UNIVERSITÀ DEGLI STUDI DELL'AQUILA
DIPARTIMENTO DI SCIENZE FISICHE E CHIMICHE

Dottorato di Ricerca in Scienze Fisiche e Chimiche

XXXV ciclo

INNOVATIVE METHODS FOR THE REALIZATION OF IMPROVED CARBON NANOTUBES-SILICON PHOTODETECTORS

SSD FIS/01

Dottorando

Daniele Capista

Coordinatore del corso
Prof. Massimiliano Aschi

Tutor
Prof. Maurizio Passacantando

a.a. 2021/2022

Abstract

Different approaches to make carbon nanotube-silicon heterojunctions have been studied. Starting from prefabricated silicon substrates, composed of an n-type silicon wafer with a silicon nitride top layer and a metallic back, the heterojunctions have been made by different approaches. Initially by direct growth of the nanotubes over the nitride layer by means of chemical vapor deposition (CVD) and then by the deposition of carbon nanotube films using a transfer printing method. The morphology, chemical composition and structure of the nanotube films obtained with the different techniques have been characterized by means of scanning electron microscopy (SEM), X-ray photoemission spectroscopy (XPS) and Raman spectroscopy. The electrical response of the vertical heterostructures (CNT-Si_3N_4-n-type Si) has been deeply investigated, both as a function of the impinging light power and the light wavelength. The properties of the photodetectors such as responsivity (R) and External Quantum Efficiency (E.Q.E.) have been studied. Temperature dependence of the diode parameters such as on/off ratio, Schottky barrier height, ideality factor and series resistance have been performed on some of the devices and compared to that of silver-silicon heterostructure made by the deposition of Ag conductive paste above one of the substrates. Photo-response maps of the devices allowed us to correlate the morphological properties of the nanotube film and the thickness of the nitride layer to the electrical behaviours of the devices. To exploit these behaviours several techniques have been developed to easily tune the nanotube film's morphology and the nitride layer's thickness to obtain devices with improved efficiency and additional function.

Table of contents

Abstract i

Table of contents ii

Introduction 1

Chapter 1. Backgrounds 4

1.1 Carbon Nanotubes 4

1.1.1 Historical Introduction 4

1.1.2 Geometrical and electronic structure 5

1.1.2.1 Graphite 5

1.1.2.2 Single-Walled Carbon Nanotubes 7

1.1.2.3 Multi-Walled Carbon Nanotubes 12

1.1.3 Synthesis of carbon nanotubes 14

1.2 Basis of heterojunction 17

1.2.1 P-N junction 17

1.2.2 Metal-Semiconductor junction 20

1.3 Main characteristic of a photodetector device 24

1.4 Photodetectors figure of merit 25

1.4.1 Responsivity (R) 25

1.4.2 Detectivity (D) 25

1.4.3 Response time 26

1.4.4 External Quantum Efficiency (E.Q.E.) 26

Chapter 2. Effect of film thickness 27

2.1 Device realization 27

2.2 Carbon Nanotube characterization 29

2.3 Electrical measurements 32

2.3.1 First device 32

2.3.2 Second device 34

2.3.3 Third device 40

2.4 Conclusions 43

Chapter 3. Photodetectors by transfer printing of carbon nanotube film 45

3.1 Device realization 45

3.1.1 Single-walled Carbon nanotubes water dispersion 45

3.1.2 Vacuum filtration *46*

3.1.3 Dry transfer printing *47*

3.1.4 Wet transfer printing *48*

3.2 Film characterization 49

3.3 Device characterization 52

3.3.1 Electrical measurements *52*

3.3.2 Diode parameter evaluation *59*

3.4 Conclusion 63

Chapter 4. Varying the Si_3N_4 thickness to tune the photoresponse 65

4.1 Device realization 65

4.2 Film characterization 68

4.3 Device characterization 70

4.4 Conclusions 80

Chapter 5. Conclusion 82

List of publications 86

Activities 88

References 90

Introduction

Nowadays photodetectors (PDs) are our society's most used technological devices. They can be found in simple day-life devices such as TV remotes, smartphones, and automatic cars, but they can also be found in many research facilities, hospitals, and military structures [1–4]. Depending on the application a PD needs to be sensitive to a different region of the electromagnetic spectrum, especially in the range from infrared to ultraviolet radiation. The main properties required for a PD are high sensitivity in the operating wavelengths, fast response, and low noise. Generally, PDs can be divided into two subgroups, the photon type, or the thermal type, depending on whether the thermal relaxation process is involved in the photoelectric conversion process. Photon-type photodetectors are made by a semiconductor, in which the radiation excites the electrons from the valence band into the conduction band, contributing in this way to the formation of a photocurrent.

The need for low-cost photonics and the possibility to exploit the high technical knowledge of the silicon electronic industry paved the way for the development of silicon photonics and its integration into optoelectronic devices. In this field, silicon photodetectors (SiPDs) are the oldest and best-understood silicon photonic devices[5]. Commercial products can operate at wavelengths in the range from 300 to 900 nm, where band-to-band absorption occurs. Despite their high development, the limited absorption in the UV and IR spectra reduces their possible applications. To extend their operating spectral region, SiPDs have been combined with smaller bandgap elements like germanium to improve the absorption of low energy photons[6]. In other approach, the avalanche photomultiplication that occurs in silicon substrate is used to increase the signal coming from InGaAs absorber[7].

In the last decade, different groups tried to improve the properties of conventional SiPDs by combining them with low-dimensional materials [8–12]. Between them, carbon nanotubes represent one of the major candidates to achieve this goal since their outstanding electronic properties. Due to their exotic electronic structure, flexible atomic conformation, and intriguing physical properties, CNTs have been already implemented in many advanced devices such as photoconductive wires [13,14], photosensitive transistors [15], innovative solar cells [16,17], or chemical sensors [18–25].

In this work, I have studied different ways to obtain large area CNT/Si heterostructure and I have characterized their photodetection abilities. Several methods have been used to realize the detectors and different methods have been developed to improve the efficiency or to add new features to the photoresponce, allowing new possible applications in heterogeneous logic circuits such as Boolean logic optoelectronic circuits.

In the first Chapter is presented a summary of the main physical properties of carbon nanotubes, and the main techniques used for their production. A summary on the characteristic and figures of merit of photodetector is also presented.

In the second Chapter will be described a MWCNT-Si heterostructure obtained by the growth of carbon nanotubes directly grown on the silicon substrate using the Chemical Vapor Deposition (CVD) technique. A method to improve the efficiency has been developed after a combined analysis of the electrical behaviour and the morphology of the film has shown that a higher thickness of the nanotube film can negatively affect the device response. The efficiency of the devices has been studied before and after the application of this method to verify its potentiality and limits.

In the third chapter will be described a SWCNT-Si photodetector obtained by the deposition of a SWCNT film on the surface of a silicon substrate using the transfer printing method. The transfer is achieved without the expensive equipment necessary for the CVD. Furthermore, since it is obtained at room temperature, the substrate does not withstand the thermal stress associated to the CVD growth. The electrical analysis of the device showed a peculiar behaviour of the photocurrent, which depended strongly on the light spot position across the active surface of the device. This unexpected behaviour has been exploited to propose the device as a Boolean operator inside logic circuits. The diode parameters associated to the device (such as on/off ratio, ideality factor, Schottky barrier height and series resistance) have been characterized as a function of the operating temperature and compared to the ones obtained from a silver-silicon (Ag-Si) device.

In the last chapter, I present a device in which the silicon substrate has been opportunely modified before the SWCNT deposition. The insulating layer above the substrate has been etched with hydrofluoric acid to create regions with different nitride thickness above the same device. In one region the silicon substrate has been completely exposed, allowing the direct contact of the nanotubes with the n-doped silicon. The junction obtained in this way has an

enhanced photovoltaic properties respect to the other regions. The presence of different thick-nesses across the device surface can be exploited to tune the active area of the detector with the applied voltage.

Chapter 1. Backgrounds

1.1 Carbon Nanotubes

1.1.1 Historical Introduction

In nature, carbon can be found in different allotropic forms: diamond, graphite, and fullerenes. Diamond possesses a crystal lattice where every atom is hybridized sp^3 and is covalently bonded to other four atoms in a tetrahedral geometry. Graphite instead is composed of layers of carbon atoms with an sp^2 hybridization (where each atoms form covalent bond with three atoms from the same layer), kept together by a weak Van der Waals interaction. The last allotropic form comprehends different kinds of molecules where the atoms possess an sp^2 hybridization but are arranged in space to form cages with a spherical or cylindrical shape.

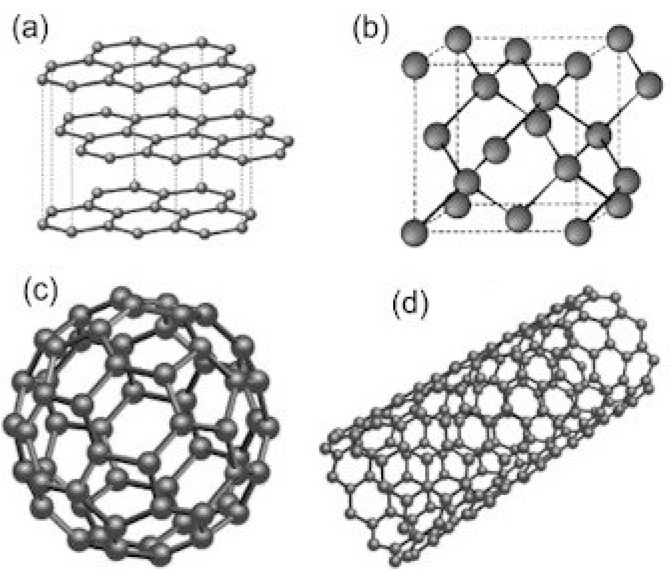

Figure 1-1(a) Graphite, (b) Diamonde, (c) C60, (d) Carbon nanotube.

The first of these molecules was observed in 1985 by Kroto, Smalley, Curl, and their collaborators at Rice University in Texas while they were making experiments to unveil the mechanism that allows the formation of carbon long-chains in interstellar space. They observed that the vaporization of graphite with a laser led to the formation of a highly stable structure made of sixty carbon atoms. They called this molecule Buckminsterfullerene (or C_{60}), and

they suggest that the atoms were disposed at the vertex of a truncated icosahedron. Although the atoms are still in an sp^2 hybridization, the round shape of C_{60} imposes an out-of-plane strain on the bond between carbon atoms, making the electronic properties completely different from that of graphite. As a fact, while graphite is semi-metallic, fullerenes are semiconductors [26]. In 1990 Rick Smalley proposed the existence of a cylindrical fullerene obtained by the elongation of C_{60} molecules. The first experimental evidence was observed by Sumio Iijima in 1991 when he found needle-shaped structures in the residue produced by his arc-discharge evaporator. These needles were long till one micron and had diameters between three and forty nanometres. Using tunnelling electron microscopy he observed that each of these needles was formed by a coaxial tube of graphitic carbon, with a number of inner tubes ranging from two to fifty [27]. These structures were then called Multi-Walled Carbon Nanotubes (MWCNT). Further studies in this new field led to the discovery in 1993 of Single-Walled Carbon Nanotubes. The discovery was achieved by two different groups: Iijima at NEC Laboratory and Bethunes at the IBM Almaden Laboratory [28,29].
The discovery of these materials had significant importance because it paved the way for numerous studies aimed at experimentally verify the theories on their properties and most importantly the study on how to exploit them. Over the years carbon nanotubes have been used in different applications, like *composite materials* [30–33], *electrochemical devices*, like supercapacitors or electrodes for lithium-ion batteries; *gas storage units* or *electrical devices* like field emitters, sensors [34–36], or nanometre-sized semiconductor devices [37]. Different synthesis methods have been developed for the mass production of highly pure CNTs. They can be grown into an organized three-dimensional complex structure or a two-dimensional flexible sheet, with both aligned or randomly oriented tubes [38,39].

1.1.2 Geometrical and electronic structure

1.1.2.1 Graphite

The structure of graphite consists of layers of carbon atoms arranged in a hexagonal pattern. These layers are stacked in the ABAB sequence and kept together by weak van der Waals forces Figure 1-2(a). The unit cell is hexagonal with dimensions c=6.71 Å and a=2.46 Å and

contains 4 carbon atoms. A single plane of graphite is called graphene. The carbon atoms are disposed on a hexagonal lattice where each atom is hybridized sp^2 and forms three σ-bond with other carbons located at 120 degrees on the layer plane at distance of 1.42 Å [40]. The unpaired $2p_z$ electron forms a delocalized orbital with π symmetry that stabilize the in-plane carbon bond. Since the interplanar distance is much higher than the intraplanar one, the interaction on an atom between the nearest plane will be weaker than the interaction between the nearest neighbour of the same plane. This allows us to approximate the electronic structure of graphite to that of graphene[41].

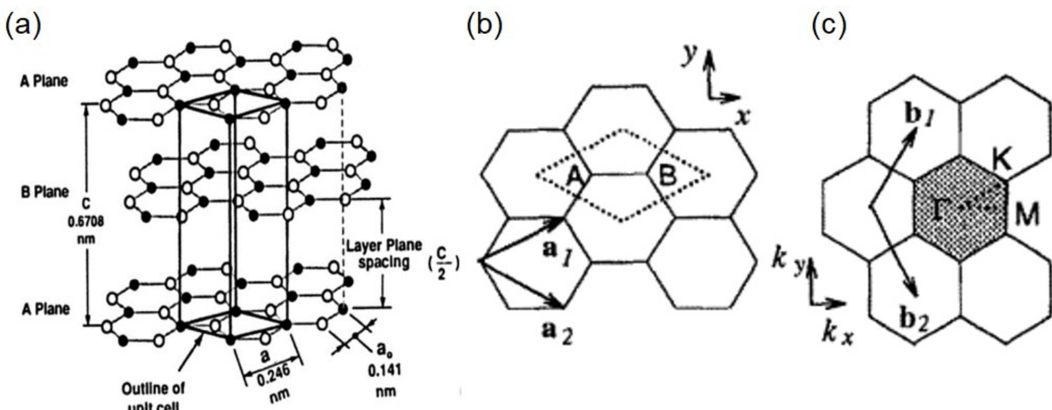

Figure 1-2 (a) Crystal structure of graphite showing -ABABAB- stacking sequence and unit cell. (b) Unitary with basis vector of graphene. (c) First Brillouin zone and reciprocal lattice vector of graphene.

The unitary cell and the first Brillouin zone are reported in Figure 1-2 (b-c) with the respective translational vectors: $(\boldsymbol{a}_1, \boldsymbol{a}_2)$ for the real lattice and $(\boldsymbol{b}_1, \boldsymbol{b}_2)$ for the reciprocal lattice. Using an (x,y) reference frame the translational vector in the real space can be written as:

$$\boldsymbol{a}_1 = \left(\frac{\sqrt{3}}{2}a; \frac{a}{2}\right), \boldsymbol{a}_2 = \left(\frac{\sqrt{3}}{2}a; -\frac{a}{2}\right) \tag{1.01}$$

where $a = |\boldsymbol{a}_1| = |\boldsymbol{a}_2| = (1.42 \times \sqrt{3})\text{Å} = 2.46\ \text{Å}$ is the in plane nearest neighbour distance. These vectors correspond to a reciprocal lattice with basis vectors:

$$\boldsymbol{b}_1 = \left(\frac{2\pi}{\sqrt{3}a}; \frac{2\pi}{a}\right), \boldsymbol{b}_2 = \left(\frac{2\pi}{\sqrt{3}a}; -\frac{2\pi}{a}\right) \tag{1.02}$$

Figure 1-2(c) reports also the high symmetry points of the first Brillouin zone: namely the centre **Γ**, the corner **K**, and the centre of the edge **M**. Figure 1-3 reports the energy dispersion relation calculated along the high symmetry direction of the triangle **ΓKM** and the related density of state. Since each unitary cell of graphene contains two carbon atoms, and each

carbon atoms have four valence electrons, the system will have 8N occupied states. Keeping in mind that each band can fit at most 2N state, the electronic band of graphene will be filled up to the π band. This means that the Fermi level will pass exactly at the **K** point where the π and π* bands are degenerate. Since an accurate calculation of the density of state shows that the density at the Fermi energy is zero, graphene is usually called a zero-gap semiconductor. The existence of this zero-gap at the **K** point gives rise to an exotic quantum effect in the electronic structure of carbon nanotubes.

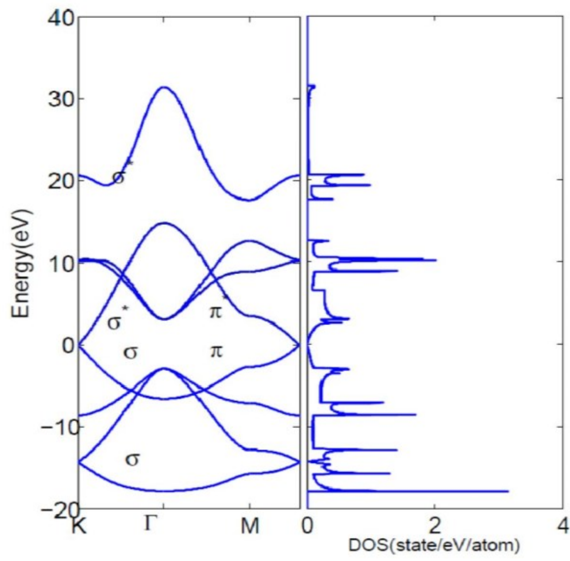

Figure 1-3 Energy dispersion relation along the high symmetry points of graphene and relative density of states.

The basic concept introduced for the two-dimensional graphite in this chapter will be used to discuss the structure and the electronic properties of carbon nanotubes.

1.1.2.2 Single-Walled Carbon Nanotubes

A single-walled carbon nanotube (SWCNT) can be imagined as a graphene sheet rolled up in a cylindrical shape to obtain a structure with axial symmetry. Considering the high aspect ratio of the cylinder (i.e., the ratio between the length of the cylinder and its diameter) these nanotubes can be considered as a one-dimensional nanostructure. The orientation of the six-membered ring in the honeycomb lattice in the tube can be taken almost arbitrarily without inducing any distortion to the hexagonal lattice, except for the distortion due to the curvature

of the nanotubes. Generally, the tubes are closed by a hemisphere of fullerene, where the hexagon and pentagons are arranged to perfectly fit the cylindrical section.

Figure 1-4(a) shows a classification of carbon nanotubes: zigzag and armchair nanotubes, which are the only two types of achiral nanotubes (i.e., their mirror image can be superposed to the original one) and then the generic chiral nanotubes, where the spiral symmetry prevents the superposition of the mirror and original images.

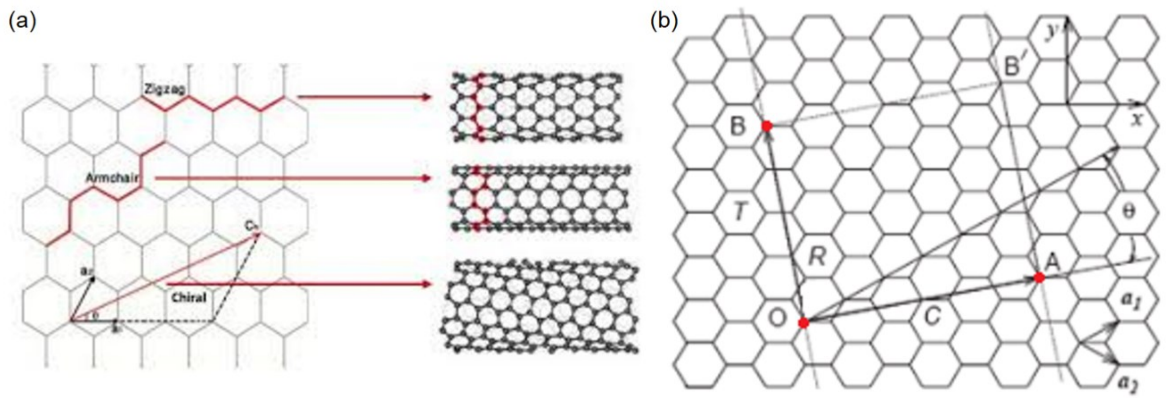

Figure 1-4 (a) Different typologies of nanotubes, in order Zigzag, Armchair and Chiral. (b) Graphene sheet with reported in red the points O, A, and B and the cutting lines used for the definition of the nanotube. Are also reported the chiral vector, the translational vector, and the chiral angle.

A carbon nanotube can be constructed starting from a simple toy model. Starting from a graphene sheet it is needed to choose two different points of the lattice, one to fix the origin **O** and a generic point **A**. these two points will individuate the segment $\overrightarrow{OA}$. A graphene string can be obtained supposing to cut along the directions perpendicular to $\overrightarrow{OA}$ and passing through the points **O** and **A**. Now imagining closing the string along the cuts will generate the nanotubes itself. It is possible to find another point **B** along the cut through the origin that possess translational symmetry respect to point **O**. The vectors $\overrightarrow{OA}$ and $\overrightarrow{OB}$ determine respectively the *chiral vector* $\boldsymbol{C}_h$ and the translational vector $\boldsymbol{T}$. The chiral vector can be express in terms of the real space unit vector of graphene defined in (1.01):

$$\boldsymbol{C}_h = \mathrm{n}\boldsymbol{a}_1 + \mathrm{m}\boldsymbol{a}_2 \tag{1.03}$$

where *n* and *m* are integer numbers that satisfy the relation $0 \leq |m| \leq n$.

Starting from the chiral vector is possible to determine the diameter of the nanotube and its chiral angle that is the angle between the chiral vector and basis vector of graphene $\boldsymbol{a}_1$. These quantities are defined as follow:

- *Diameter*: $d_t = \frac{|C_h|}{\pi}$; $|\boldsymbol{C_h}| = \sqrt{\boldsymbol{C_h} \cdot \boldsymbol{C_h}} = a\sqrt{n^2 + m^2 + nm}$
- *Chiral angle*: $\theta = arccos\left(\frac{\boldsymbol{C_h} \cdot \boldsymbol{a_1}}{|\boldsymbol{C_h}||\boldsymbol{a_1}|}\right) = arccos\left(\frac{2n+m}{2\sqrt{n^2+m^2+nm}}\right)$

Depending on the values of *n* and *m* the nanotube can have a chiral or achiral structure. The following table resumes the main structure of nanotubes with the associated condition on the values of *n*, *m*.

n, m	**Structure**	**Graphic representation**
m = n ≠ 0	Armchair	
m = 0, n ≠ 0	Zig-zag	
Any other combination	Chiral	Combination of the two conformations.

Table 1-I Graphic representation of the nanotube associated to the (n,m) values.

The translational vector **T** can also be expressed in terms of the basis vector:

$$\boldsymbol{T} = \mathrm{t}_1\boldsymbol{a}_1 + \mathrm{t}_2\boldsymbol{a}_2 \qquad (t_1\ and\ t_2\ integer\ numbers) \tag{1.04}$$

The numbers t_1 and t_2 can be obtained by imposing the orthogonality between the chiral vector and the translational vector ($\boldsymbol{C_h} \cdot \boldsymbol{T} = 0$) leading to:

$$t_1 = \frac{2m+n}{\alpha}; t_2 = -\frac{2n+m}{\alpha} \tag{1.05}$$

where α is the greatest common divisor of $(2m + n)$ and $(2n - m)$.

The unitary cell of the nanotube in the real space is the rectangle *OABB'* defined by the chiral and translational vector as reported in Figure 1-4. It is straightforward to determine the number of hexagons **N** in each unit cell of the nanotubes by dividing its area by the area of the unit cell of graphene:

$$\mathrm{N} = \frac{S_{tube}}{S_{exagon}} = \frac{\boldsymbol{C_h} \times \boldsymbol{T}}{\boldsymbol{a}_1 \times \boldsymbol{a}_2} = \frac{2(\mathrm{m}^2 + \mathrm{n}^2 + \mathrm{nm})}{\alpha} \tag{1.06}$$

The reciprocal lattice vector of a nanotube can be evaluated using the relation $\boldsymbol{R}_i \cdot \boldsymbol{K}_j = 2\pi\delta_{ij}$ where $\boldsymbol{R}_i$ and $\boldsymbol{K}_j$ are respectively the real and reciprocal space basis vector. We get the relations for $\boldsymbol{K}_1$ and $\boldsymbol{K}_2$:

$$\boldsymbol{K}_1 = \frac{1}{\mathrm{N}}(-t_2\boldsymbol{b}_1 + t_1\boldsymbol{b}_2); \qquad \boldsymbol{K}_2 = \frac{1}{\mathrm{N}}(m\boldsymbol{b}_1 - n\boldsymbol{b}_2) \tag{1.07}$$

where $\boldsymbol{b_1}$ and $\boldsymbol{b_2}$ are the reciprocal lattice vector of graphene given by Eq. (1.02).

Figure 1-5 First Brillouin zone of a SWCNT (4,2), composed of 28 lines superimposed to the first Brillouin zone of graphene.

Since nanotubes are one-dimensional materials only $\boldsymbol{K}_2$ will be an actual reciprocal lattice vector, while $\boldsymbol{K}_1$ will give discrete k values in the direction of $\boldsymbol{C}_h$. The first Brillouin zone will be the line segment *WW'* in Figure 1-5. Since $N\boldsymbol{K}_1 = -t_2\boldsymbol{b}_1 + t_1\boldsymbol{b}_2$ is a reciprocal lattice vector of graphene, it results that two wave vectors which differ by $N\boldsymbol{K}_1$ are equivalent. Since the numbers t_1 and t_2 do not have a common divisor except for unity, all the N-1 vector long $\mu\boldsymbol{K}_1$ (whit $\mu = 0, 1, \ldots, N-1$) will identify N discrete k vectors. This phenomenon arises from the quantization of the wave vectors due to the periodic boundary condition on $\boldsymbol{C}_h$.

Starting from this description of the nanotube structure is possible to determine its electronic structure using the tight-binding methods for the π orbital of the carbon atoms.

Since the wave vector associated with the $\boldsymbol{C}_h$ direction become quantized, the energy bands will consist of a set of *N* one-dimensional energy dispersion relations which are a cross-section of the energy dispersion surface of graphene with cuts made along the lines shown in Figure 1-5.

These 1D energy dispersions will be described by the relation.

$$\mathrm{E}_{\mu}(\mathrm{k}) = \mathrm{E}_{\mathrm{graphene}}\left(\mathrm{k}\frac{\mathbf{K}_2}{|\mathbf{K}_2|} + \mu\boldsymbol{K}_1\right), \left(\mu = 0, \ldots, N-1, and\ -\frac{\pi}{\mathrm{T}} < k < \frac{\pi}{T}\right) \tag{1.08}$$

For specific values of (n, m) a cutting line can pass through the K point of graphene, where the π and π^* energy bands are degenerate by symmetry, making also the one-dimensional energy band of the nanotube with a zero-energy gap. In this case, the calculated density of

state at the Fermi energy is a finite number, therefore nanotubes will be metallic. If, however, the cutting line does not pass through the K point, the nanotube is expected to be semiconductive, with a finite gap between the valence and the conduction bands.

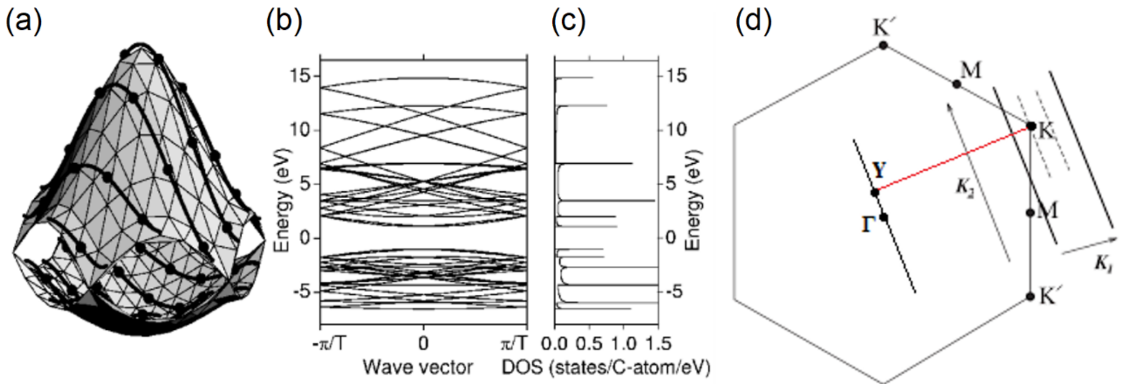

Figure 1-6 (a) Valence and conduction band of graphene with superimposed the cutting lines of a (4,2) nanotube. The point on these lines represents the extremal points of the nanotube bands. (b) Associated energy dispersion and (c) density of states for the (4,2) nanotube. (d) First Brillouin zone of graphene with superimposed the cutting lines of the nanotube, in red is reported the distance between the first cut and the K point.

A nanotube to be metallic needs that the distance between the first cut and the K point of graphene (i.e., the distance $\overline{YK}$ in Figure 1-6) is equal to an integer multiple of the vector $\boldsymbol{K}_1$. Since the distance $\overline{YK}$ can be expressed by:

$$\overline{YK} = \frac{2n+m}{3}\boldsymbol{K}_1 \tag{1.09}$$

the nanotubes will be metallic every time $(2n+m)$ is a multiple of 3. This highlight the fact that all armchair nanotubes (denote by (n, n)) are metallic, while zig-zag nanotubes (denoted by (n, 0)) are metallic only when *n* is a multiple of 3.

The cutting lines near the K point can be found in three possible configurations depending on:

$$n - m = \begin{cases} 3l \\ 3l+1 \\ 3l+2 \end{cases} \quad with\ l \text{ integer number}$$

In the first case the nanotube will be metallic since it satisfies the relation in Eq. (1.09), the other two cases describe the position of the K point at one-third and two third of the distance between two successive lines. This allows the classification of the semiconductive nanotubes in semiconductor type S1 or S2 depending on $(n-m-3l)$ is equal to 1 or 2.

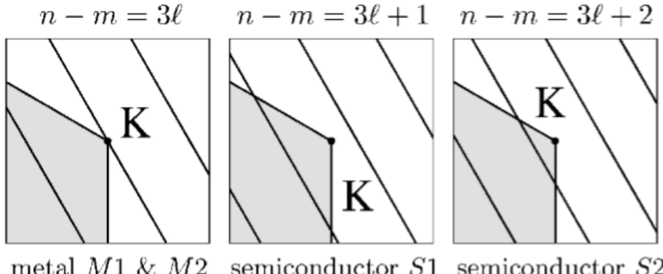

Figure 1-7 Possible positions of the cutting lines with respect to the K point. The first case corresponds to metallic nanotubes, while the other to S1 and S2 semiconducting nanotubes.

A similar classification can be made also for the metallic nanotubes, depending on the position of the K point along the cut line. By making a projection of the vector $\overline{\Gamma K}$ on the vector $\boldsymbol{K}_2$ it is possible find the length of the segment $\overline{\Gamma Y}$:

$$\left|\overline{\Gamma Y}\right| = \overline{\Gamma K} \cdot \frac{\boldsymbol{K}_2}{|\boldsymbol{K}_2|} = \frac{m}{\alpha}|\boldsymbol{K}_2| \tag{1.10}$$

This shows that the projection is equal to the base vector $\boldsymbol{K}_2$ times the ratio of the value *m* of the nanotube and α (the greatest common divisor found in Eq. (1.05)). If we define the number *d* as greatest common divisor between *n* and *m*, it is possible to notice that the value α can have only two values:

$$\alpha = \begin{cases} d, & if\ n - m\ is\ a\ multiple\ of\ 3d \\ 3d, & if\ n - m\ is\ not\ a\ multiple\ of\ 3d \end{cases}$$

In the first case since α will be a divisor of m, the ratio will give an integer number and therefore the point **Y** will become the **Γ** point (since it is translated by an integer number of times the vector $\boldsymbol{K}_2$), so the degeneracy will occur at $k = 0$. In the other case the ratio can be expressed as $m/\alpha = \ \nu \pm 1/3$ (with ν is an integer), and the degeneracy will occur at $k = \pm 2\pi/3T$. Depending on which of the two cases the nanotube can be classified as a *metal-1* or a *metal-2* nanotube.

1.1.2.3 Multi-Walled Carbon Nanotubes

Multi-walled carbon nanotubes (MWCNTs) can be described by two different models: the first is the *Russian doll model*, consisting of a series of coaxial nanotubes of different diameters, while the second is the *parchment model* that consists of a sheet of graphene wrapped around itself manifold times (just like a scroll of paper) [42]. The first model is commonly used for the description of MWCNTs.

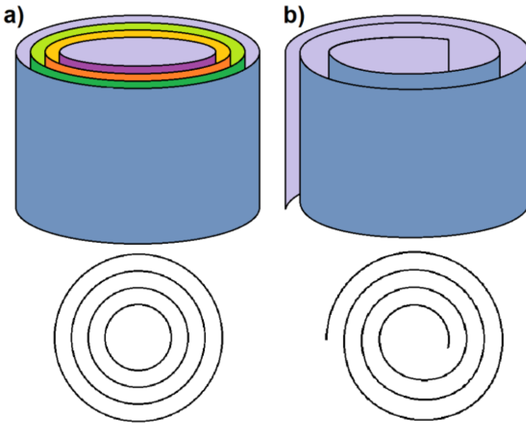

Figure 1-8 (a) Russian doll and (b) Parchment model for MWCNT.

Depending on the growing techniques, the diameter of the outer nanotube can be very different. For example, it can be 20 nm for the nanotube grown with the arc discharge method, but it can also reach 100 nm when the Chemical Vapor Deposition (CVD) is used.

It is reasonable to think that the interaction between the nanotubes contained inside a MWCNT can modify the energy dispersions close to the Fermi energy, adding in this way new properties to the material. Several studies have been made to quantify this interaction. The first models were made using the *tight-binding method* on relatively simple cases like double-walled carbon nanotubes DWCNTs, considering all the possible cases: metallic-metallic, metallic-semiconductor and semiconductor-semiconductor nanotubes [43]. It was observed that in the case of commensurate nanotubes (i.e., the ratio between the diameter is an integer number) the energetic bands with the same symmetry showed the phenomena of anticrossing, while bands with different symmetry were able to cross each other since the wavefunction remained orthogonal also with the interaction. The evaluated energetic bands of the DWCNT were very similar to the sum of the energetic bands of the single CNT, with just a small correction due to the anticrossing of the bands. Also when this phenomenon took place near the Fermi energy the system does not variate much: the two nanotubes do not change their nature because of the interaction.

Another study on MWCNT was made using the Density Functional Theory (DFT) to estimate the optimal distance between a (5, 5) and a (10, 10) armchair nanotubes. The evaluation gives a distance of 3.39 Å, values slightly lower than the distance between graphite planes (3.44 Å). This difference can be explained by an additional correlation between the atomic site of the different tubes both in the axial direction and along the circumference [44].

1.1.3 Synthesis of carbon nanotubes

Carbon nanotubes can be produced using three techniques:

- Laser ablation
- Arc discharge
- Chemical vapor deposition

The first technique was initially used by Kroto et all. to study the formation of long-chain carbon molecules in interstellar space, leading to the discovery of fullerenes. Since that day the technique has evolved and now represents an efficient way to produce a high-quality bundle of SWCNTs. In this technique, two sequenced laser pulses are used to vaporize a graphene target placed inside a furnace at 1200 °C filled with an inert gas flow. The products of the sublimation are then displaced by the gas flow into a lower-temperature region. Here, small carbon molecules and atoms begin to nucleate, bringing the formation of fullerenes and nanotubes. The gas flow transports these products to a water-cooled copper collector. Depending on the mixture of the graphite target is possible to produce both multi or single-wall nanotubes. MWCNTs will be produced using a pure graphite target, while by mixing the target with transition metals (like Co, Ni, Fe or Y) is possible to produce also SWCNTs [45–48].

The second method uses the electrical discharge between two graphite rods to obtain vaporized carbon atoms, that a nucleation process will form the nanotubes. The discharge is obtained by keeping the electrodes at a distance of 1 mm with a voltage of 20-25 V and a DC current of 50-120 A. The arc is typically operated in 500 Torr He with a flow rate of 5-15 ml/s for cooling purposes. Once the arc is in operation, the length of the positive electrode decreases, and a carbon deposit forms on the negative electrode. Pure carbon electrodes are used to produce MWCNT, while a mixture of carbon and catalysts are used to produce SWCNTs. Transition metals (Co, Fe, Ni) and rare earths (Y, Gd) are used to produce isolated SWCNTs, while mixed catalysts like Fe/Ni, Ci/Ni, and Co/Pt led to the formation of ropes of SWCNT [49,50].

Chemical vapor deposition is one of the best methods to produce great quantities of nano-tubes. The production of nanotubes is achieved after the thermal dissociation of hydrocarbons like methane or acetylene, that in presence of metallic catalysts rearrange to form tubular

structure. The temperature required for the dissociation can be achieved with an electric oven or by electric discharges that transform the gas into plasma (in this it is called Plasma Enhanced Chemical Vapor Deposition (PECVD)). Varying the type of hydrocarbons, the catalysts and the temperature is possible to produce CNT in many shapes like powder of CNT, thin films or even sponges of nanotubes [39,51–54].

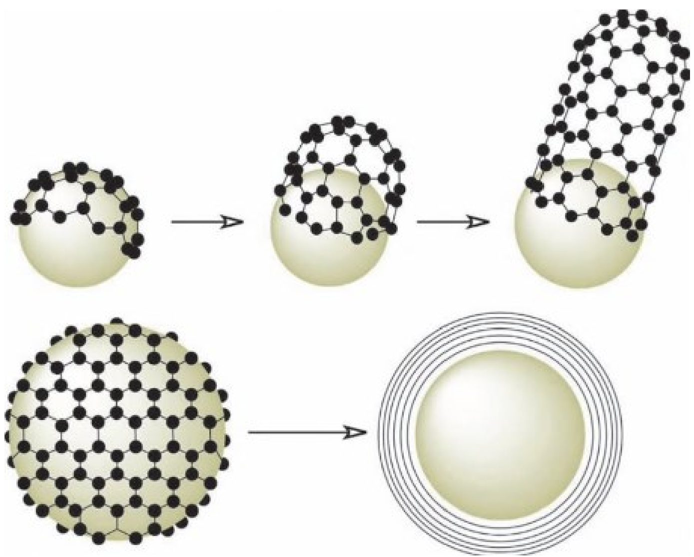

Figure 1-9 Steps of the formation of a SWCNT or an "onion" like structure.

Since the chemical and physical properties of nanotubes are directly related to their atomic structure, it is essential to understand how to control the size, number of shells, helicity, and the overhaul structure of the tube during the synthesis. The mechanisms that are responsible for nanotube growth are still unclear and present substantial differences depending on the synthesis method. Smalley et al. proposed a simple model to explain the growth of SWCNT starting from metallic particles. They suppose that in presence of a metallic particle the carbon atoms start to spread across its surface forming fullerene caps. Depending on the dimension of the particle, it will be possible to generate carbon nanotubes or graphite-encapsulated metal particles (onion structure in Figure 1-9). The small particle will be energetically favourite to extrude the carbon dome from the metal particle, producing in this way the nanotubes. With larger particle is easier to get an onion-like structure because the detachment of the cap to grow a tube has a higher energetic cost [55].

The catalytic growth of SWCNTs was investigated using first-principles molecular dynamics simulation. At an experimental temperature of 1500 K, even though the open ends of SWCNTs close spontaneously into a graphitic dome, the metal-carbon bonds keep breaking

and reforming. Such a phenomenon provides a direct incorporation process for the necessary additional carbon and suggests a close-end mechanism for the catalytic growth. The catalytic action of metallic particles is also important for the reconstruction of the nanotube tip after carbon incorporation, by the annihilation of defects.

1.2 Basis of heterojunction

A heterojunction is defined as a junction between two dissimilar semiconductors. Generally, when this happens, the asymmetry in the electronic configuration allows the current to flow only in one direction. This phenomenon is responsible for the peculiar behaviour of electronic devices such as diodes and transistors. Light can also interact with this type of junction, generating currents without an external bias, namely the photovoltaic effect. Depending on the materials involved different types of junctions can be realized. A general heterojunction is achieved by contacting two different semiconductors with different band structures (p-n junction) or even by contacting a metal with a semiconductor (Schottky junction).

1.2.1 P-N junction

The p-n junction is a particular type of heterojunction composed of only one semiconductor (for example silicon) n-doped on one side of the junction and p-doped on the other. As a result of the different concentrations of carriers in the two regions, a diffusive mechanism will lead electrons from the n region to migrate in the p region while holes will diffuse in the opposite direction. As the diffusion continues, the charges will generate an electric field that opposes further diffusive currents. This phenomenon causes the formation near the junction of a region of space where the density of carriers is reduced greatly below its value in the homogeneous regions far away (for that reason this region is called *depletion region*).
Once equilibrium is reached, drift and diffusion currents of electrons and holes must balance each other at every point of the junction:

$$\mathrm{J_n(x)} = \mathrm{J_n^{\mathit{drift}}}(x) + \mathrm{J_n^{\mathit{diff}}}(x) = nq\mu_n F + qD_n \frac{dn}{dx} = 0 \tag{1.11}$$

$$\mathrm{J_p(x)} = \mathrm{J_p^{\mathit{drift}}}(x) + \mathrm{J_p^{\mathit{diff}}}(x) = pq\mu_n F - qD_p \frac{dp}{dx} = 0 \tag{1.12}$$

(n, p are the carrier density of electron and holes respectively, $F = -\nabla\phi$ is the electric field generated by the internal space charge region and q is the electron charge).
Since the built-in potential $\psi_{bi}(x)$ varies slowly with respect to the lattice constant of the material, it is possible to retain that the energy levels of the semiconductor are rigidly shifted by the quantities $(-q)\psi_{bi}(x)$. The band edges E_c and E_v are given by:

$$E_c(x) = E_c + (-q)\psi_{bi}(x) \quad E_v(x) = E_v + (-q)\psi_{bi}(x) \tag{1.13}$$

In the pn junction at equilibrium, the free electron carrier concentration $n(x)$ depends on the position x via the relation:

$$n(x) = N_c(T)e^{-[E_c(x)-E_F]/k_BT} \tag{1.14}$$

Combining Eq (1.13) and (1.14) is possible to obtain a relation that correlates the equilibrium carrier density at any two points of the semiconductor structure:

$$n(x_1) = n(x_2)e^{-q[\psi_{bi}(x_1)-\psi_{bi}(x_2)]/k_BT} \tag{1.15}$$

The same argumentations are valid for

$$p(x_1) = p(x_2)e^{-q[\psi_{bi}(x_1)-\psi_{bi}(x_2)]/k_BT} \tag{1.16}$$

This is important because it can relate the concentration of electrons well inside the p region with that well inside the n region. By calling n_{p0} the equilibrium concentration of electron in the p region and n_{n0} that in the n region we have:

$$n_{p0} = n_{no}e^{-q\psi_{bi}/k_BT} \tag{1.17}$$

Where ϕ_b is the maximum value of the built-in potential.

When a bias potential V is applied to the junction, the effective potential barrier is modified, drift and diffusion current are no longer balanced and current can flow through the junction. By assuming that in quasi-equilibrium condition the relation (1.15) and (1.16) are still valid, the electron concentration at the boundaries of the depletion region (located at $-d_p$ in the p region and $+d_n$ in the n region) can be written as:

$$n(-d_p) = n(d_n)e^{-q(\psi_{bi}-V)/k_BT} \tag{1.18}$$

Adding the assumption of low-injection condition, i.e. the changes of the majority carrier density are negligible at the boundaries of the neutral region (the concentration of electrons at the border of the depletion layer is essentially the same concentration of electrons in the rest of the n region: $n(d_n) \approx n_{n0}$, relation (1.18) became:

$$n(-d_p) = n_{no}e^{-q(\psi_{bi}-V)/k_BT} = n_{p0}e^{qV/k_BT} \tag{1.19}$$

Where in the second equation has been used the relation (1.17). It results that the minority concentration at the left side of the depletion layer is proportional to a factor that grows exponentially to the applied voltage. A forward bias will increase the number of minority carriers (i.e. an injection) while a reverse bias will reduce the initial amount (extraction). The difference of carriers between the biased and unbiased junction can be written as:

$$\Delta n\left(-d_p\right) = n_{p0}(e^{qV/k_BT} - 1) \tag{1.19}$$

Since the semiconductor in the p region is approximately neutral, the difference of carriers (injected or extracted) at the boundaries of the depletion region gives rise to a diffusion current that can be written as [56]:

$$\mathrm{J}_n^{\mathrm{diff}}\left(-d_p\right) = qD_n\frac{\Delta n\left(-d_p\right)}{L_n} = qD_n\frac{n_{p0}}{L_n}(e^{qV/k_BT} - 1) \tag{1.20}$$

Where L_n is the minority carrier diffusion length. The total electron current at the boundaries $x = -d_p$ will be the sum of the diffusion components and drift components. The latter is negligible because so is the concentration of minority carriers and the electric field in the quasi-neutral region $x < -d_p$. The total current due to electrons in the p region can be written as:

$$J_n(-d_p) \approx \mathrm{J}_n^{\mathrm{diff}}\left(-d_p\right) = qD_n\frac{n_{p0}}{L_n}(e^{qV/k_BT} - 1) \tag{1.20}$$

In the same way, the hole current density on the n region can be written as:

$$J_p(d_n) \approx \mathrm{J}_p^{\mathrm{diff}}(d_n) = qD_p\frac{p_{n0}}{L_p}(e^{qV/k_BT} - 1) \tag{1.21}$$

By assuming that the generation and recombination process balances each other in the depletion region, the electron and hole current will be constant throughout the junction, and the total current will be the sum of the previous contributions:

$$J = J_s(e^{qV/k_BT} - 1) \tag{1.22}$$

Where J_s is the reverse saturation current density:

$$J_s = eD_p\frac{p_{n0}}{L_p} + eD_n\frac{n_{p0}}{L_n} \tag{1.23}$$

Equation (1.22) is called the ideal diode equation. To describe less ideal case, where recombination processes are included, the relation can be written as:

$$J = J_s(e^{qV/nk_BT} - 1) \tag{1.24}$$

Where n is the ideality factor, a number that can estimate the deviation of the diode behaviour from the ideal one. It can be shown that the presence of an external voltage across the junction modifies the thickness of the depletion region. For negative bias the thickness will increase and consequently the resistance of the junction, while for positive bias the thickness will reduce, determining a reduction of the resistance. In the last case, the reduction of resistance causes an exponential variation of the current as a function of the voltage.

The saturation current can be expressed as [57]:

$$J_s = Ce^{-q\psi_{bi}/k_BT} \tag{1.25}$$

Where the C and the potential ϕ_b have different behaviour and meanings depending on the junction. In pn junction C does not change and ψ_{bi} is called the activation energy.

A photodiode is a particular junction in which the light is allowed to reach the depletion region and generates electron-hole pairs. The charges, separated by the high electric field in this region, will produce an additional current. A photodiode can also work in photovoltaic mode, that is the generation of electric potential across the junction under the influence of light, without an external bias. This voltage results in an additional current flowing through the junction called the short circuit current (J_{sc}). Using the superposition approximation, the overall current-voltage response of the junction can be estimated as the sum of the short circuit current and the dark current. For an ideal diode it will become:

$$J = J_s(e^{qV/nk_BT} - 1) - J_{sc} \tag{1.26}$$

1.2.2 Metal-Semiconductor junction

When a metal is contacted to a semiconductor, a barrier will form at the materials interface. The presence of this barrier will control the current flow and the capacitance of the junction.

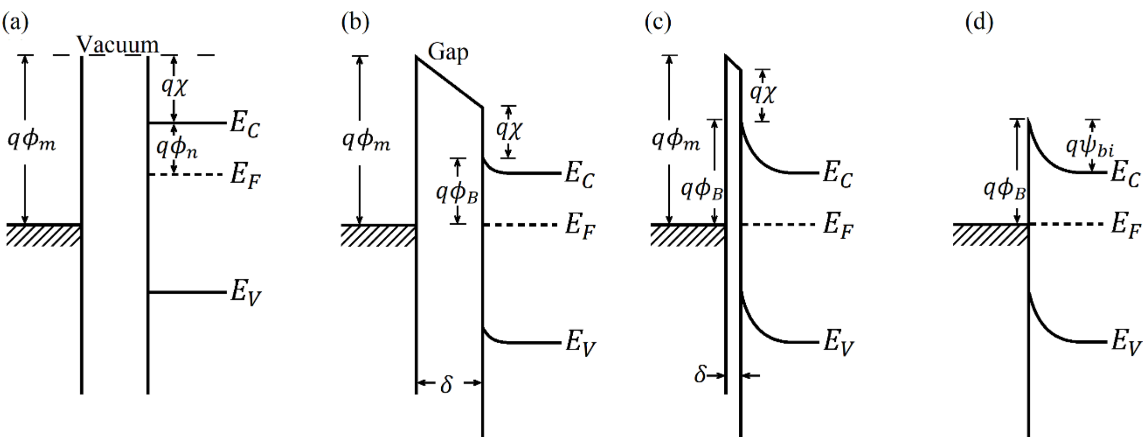

Figure 1-10 Energy-band diagrams of metal-(n-type)semiconductor junction. Metal and semiconductor in separated system(a) and connected in one system (b). System with smaller gap δ (c) and with no gap (also reported the value of the built-in potential ψ_{bi}) (d).

In the ideal case (i.e., no surface state and other anomalies), the electronic energy relation of an n-type semiconductor and a metal in separate systems can be described as Figure 1-10 (a). Supposing to connect the two materials with an external wire (but keeping them at a distance

δ), is possible to allow the communication between them. In this way a single system is established between the two materials and the electrons from the semiconductor will flow to the metal until an equilibrium is reached and the Fermi levels are lined up Figure 1-10 (b). The Fermi level of the semiconductor will be lowered by an amount equal to the difference between the work function of the two materials. These values can be expressed as: $q\phi_m$ for the metal, and $q(\chi + \phi_n)$ for the semiconductor, where $q\chi$ is the electron affinity and $q\phi_n$ is the energy difference between the bottom of the conduction band and the Fermi level.
Supposing to slowly approach the two materials (Figure 1-10 (c)), the electric field in the gap will increase and more negative charges will flow to the metal, leaving an equal number of positive charges in the semiconductor depletion region (similar behaviour of a one side p-n junction). Resulting in an increased contact potential ϕ_B. In the limiting case of δ=0, the gap becomes transparent to the electrons and the limit value of barrier height $q\phi_B$ is reached (Figure 1-10 (d)):

$$q\phi_B = q(\phi_m - \chi) \tag{1.27}$$

The barrier height simply became the difference between the work function of the metal and the electron affinity of the semiconductor.

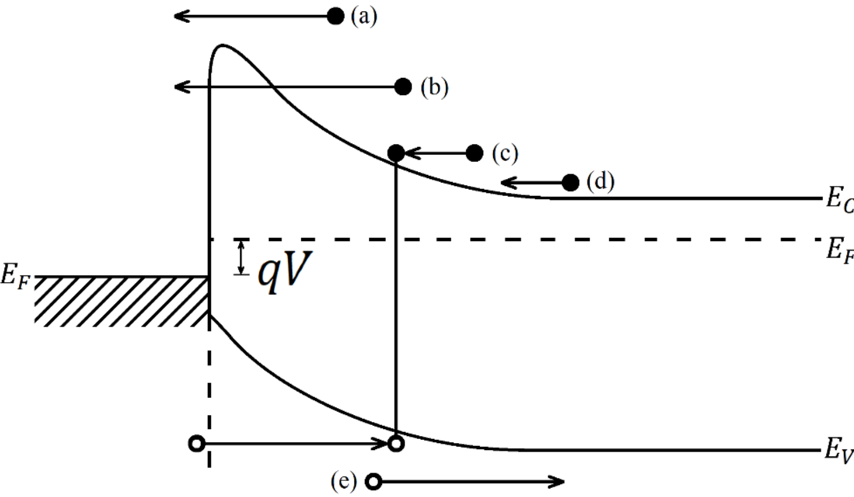

Figure 1-11 transport phenomena under forward bias (+V). (a) Thermionic emission, (b) tunnelling, (c) recombination and diffusion of electrons (d) and holes (e).

In contrast to the p-n junction, where the minority carriers are responsible for the current transport, in the case of a metal-semiconductor junction the current is mainly due to the majority carriers. Five basic transport processes can be described in this type of junction. For

the case of a forward biased metal/n-type semiconductor they can be described as: the emission of electrons over the potential barrier (*Thermionic Emission*), the quantum-mechanical tunnelling of electrons through the barrier, recombination in the space charge region, diffusion of electrons in the depletion region and hole injection from the metal. For common high-mobility semiconductor like silicon and GaAs the thermionic emission theory offer a good approximation of the transport process [57].

The thermionic emission theory, firstly proposed by Bethe [58], is derived under the assumption that the barrier height $q\phi_B$ is much larger than $k_B T$, thermal equilibrium is established at the plane that determine emission and that the formation of the net current flow does not perturb this equilibrium. With these conditions the total electron current through the junction (J_n) can be obtained by the superposition of two currents: one from the metal to the semiconductor (J_{ms}) and one from the semiconductor to the metal (J_{sm}). Furthermore, these assumptions allow to consider the Fermi level flat inside the semiconductor region. Consequently, the current flows will depend only on the barrier height, and the current density from the semiconductor to the metal can be expressed as a function of the concentration of electrons with energies higher than the barrier potential. Their number as a function of the applied forward potential can be written as:

$$n(V) = N_C e^{-\frac{q(\phi_B - V)}{k_{BT}}} \qquad where \;\; N_C = 2\left(\frac{2\pi m^* k_B T}{h^2}\right)^{\frac{3}{2}} \tag{1.28}$$

Considering now the current due to the random motion of carrier across a plane, for a Maxwellian distribution of carriers it is possible to express the current density as:

$$J = nq\frac{v_{ave}}{4} = \frac{nq}{4}\sqrt{\frac{8k_B T}{\pi m^*}} \tag{1.28}$$

Combining Eq. 1.28 with Eq. 1.27 is possible to write the J_{sm} as:

$$J_{sm} = \frac{4(KT)^2 q\pi m^*}{h^3} e^{-\frac{q(\phi_B - V)}{k_B T}} \tag{1.29}$$

$$= A^* T^2 e^{-\frac{q\phi_B}{k_B T}} \; e^{\frac{qV}{k_B T}} \tag{1.30}$$

Where A^* is the Richardson constant for thermionic emission (for free electrons $A^* = 120\ Acm^{-2}K^{-2}$).

To complete the description is required to consider the transport of electrons from the metal to the semiconductor. To obtain this value is important to make a simple consideration. The

barrier potential seen from an electron in the metal region will not change when an external voltage is applied. Consequently, also the current will be unaffected by this parameter. This must be true especially in the case of no external bias ($V = 0$), where the net current is zero:

$$J_n(V = 0) = J_{ms} + J_{sm}(V = 0) = 0 \tag{1.31}$$

From which is possible to determine the J_{ms}:

$$J_{ms} = -J_{sm}(V = 0) = \; -A^{*}T^{2}e^{-\frac{q\phi_B}{k_B T}} \tag{1.32}$$

The total current density can then be expressed as the sum of Eq. 1.30 and Eq. 1.32:

$$J_n(V) = \left[A^{*}T^{2}e^{-\frac{q\phi_B}{k_B T}}\right] \left[e^{\frac{qV}{k_B T}} - 1\right] = J_s\left[e^{\frac{qV}{k_B T}} - 1\right] \tag{1.33}$$

Eq. 1.33 give a similar behaviour of the relation obtained for the p-n junction (Eq.1.24) and show the temperature dependence of the parameter C in Eq. 1.25:

$$J_s = Ce^{-\frac{q\phi_B}{k_B T}} = A^{*}T^{2}e^{-\frac{q\phi_B}{k_B T}} \tag{1.34}$$

1.3 Main characteristic of a photodetector device

The main ability of a photodetector is the conversion of incident radiation into electrical signals. The principle behind this ability is the quantum photoelectric effect: a photon excites an electron-hole pair which contributes to the photocurrent. To be detected, a photon must be absorbed by the material, but this happens only if the photon's energy is equal or greater than the electronic transitions inside the material. It must therefore occur:

$$E_p = h\nu > E_G \tag{1.27}$$

where h is Planck's constant, ν the frequency of the incident radiation and E_G is the gap energy between the valence and conduction band of the material invested by the radiation. Using the relation $\nu = c/\lambda$, where c is the speed of light and λ is the wavelength of the incident radiation, one can express the minimum wavelength limit for detection as:

$$\lambda_{min} = \frac{hc}{E_G} \tag{1.28}$$

An important aspect that must be kept in mind is how the light is able to penetrate inside the material. This is described by the Beer-Lambert law:

$$I = I_0 e^{-\alpha t} \tag{1.29}$$

where I_0 is the intensity of the incident light, t is the thickness of the material and α is the absorption coefficient. This law states that the intensity of the incoming light decreases exponentially inside the material. The speed of this decrease is determined by the parameter α: a high value means that light is absorbed near the surface while lower values mean a higher penetration of light inside the material. In the extreme cases, the semiconductor can be transparent to incoming radiation.

1.4 Photodetectors figure of merit

Several parameters have been developed to evaluate and compare the performance of photodetectors, that can in principle have different geometry, active materials and operating mechanism. These are the responsivity (R), the detectivity (D), the response time and the external quantum efficiency (E.Q.E.).

1.4.1 Responsivity (R)

The ability of a photodetector to generate photovoltage (V_{ph}) or photocurrent (I_{ph}) under illumination at a certain light power (P_{in}) is evaluated by the Responsivity R. It is defined as the ratio of the photocurrent or photovoltage over the incident light power.

$$R = \frac{I_{ph}}{P_{in}} = \frac{I_{light} - I_{dark}}{P_{in}} \left(\frac{A}{W}\right) \; or \; \frac{V_{ph}}{P_{in}} = \frac{V_{light} - V_{dark}}{P_{in}} \left(\frac{V}{W}\right) \tag{1.30}$$

Where the subscript *light* indicates that the measures has been performed under illumination, while *dark* stands for the measures performed in dark condition.

1.4.2 Detectivity (D)

Detectivity represents the ability to detect faint light signals, which can be used to compare the performance of photodetectors with different active materials, geometries, or work mechanisms. This parameter is usually calculated as:

$$D = \frac{\sqrt{A\Delta f}}{NEP} \tag{1.31}$$

In this relation A is the active area of the device, Δf is the electrical bandwidth (defined as the frequency at which the electrical power spectrum drops to 50% of its value at DC) and the noise equivalent power of the photodetectors, respectively. The detectivity can also be expressed as:

$$D = \frac{R\sqrt{A}}{\sqrt{2eI_{dark}}} \tag{1.32}$$

where A and e are respectively the active area of the device and the elementary charge. From this equation, the D value of a photodetector can be significantly increased by lowering the dark current or by improving R.

1.4.3 Response time

The response time is an important factor in the detection of rapidly modulated optical signals, which is in close relation to the generation-recombination process of carriers. With response time are indicated the rise time (τ_r) and the decay or fall time (τ_f), which are the time required for the photocurrent to rise from 10% to 90% of the maximum value for the rise time, or vice versa for the fall time.

1.4.4 External Quantum Efficiency (E.Q.E.)

The External Quantum Efficiency (E.Q.E.) represents the percentage of photons hitting the active surface of the device that has been absorbed and collected as photo charges. It can be estimated as the ratio of the collected electrons to the impinging photons over the device. The first value can be estimated by dividing the measured photocurrent by the elemental charge e while the second dividing the incident light power by the energy of the single photon. The relation becomes:

$$E.Q.E. = \frac{N_{electrons}}{N_{photons}} = \frac{I_{ph} hc}{eP_{in}\lambda} = R\frac{hc}{e\lambda} \tag{1.33}$$

where h is Plank constant, c is the speed of light and λ il the light wavelength.

Chapter 2. Effect of film thickness

This chapter reports the analysis made on a heterojunction between MWCNTs grown directly on a silicon substrate. The MWCNTs film has been characterized through scanning electron microscopy, X-ray photoemission spectroscopy and Raman spectroscopy. Different electrical measurements have been performed on the devices to understand the nature of the junction, and how the efficiency changes across the visible spectrum. A series of measurement have been made to see if the current produced by the light could change as a function of light spot position across the device surface. These measurements led to the observation of inhomogeneities of the efficiency of the MWCNT film, that has been directly correlated to the presence of different thicknesses along the nanotube film. To confirm this observation a technique has been developed to easily modify the thickness of a grown CNT film. The nanotubes have been grown above a substrate composed of a 500 μm n-type silicon wafer (resistivity 1-5 Ωcm, doping 10^{15} cm^{-1}) with the top surface covered by Si_3N_4 layers thick 140 nm. The substrate presented two metallic pads of $1mm^2$ (50 nm Pt over 10 nm Ta) on the top surface and a metallic layer (same structure as the pads) on the bottom surface to allow electrical measurements.

2.1 Device realization

The device in this section have been realized by growing MWCNT above the substrate using the chemical vapor deposition (CVD) method. The CVD reactor shown in Figure 2-1 is composed of a horizontal quartz tube (150 cm long, 7 cm diameter) insert in an electric furnace. The furnace is connected to electric motors that can move its position along the tube. This configuration is used to speed up the heating and cooling of the substrate. Once the temperature of the furnace has reached the operating temperature, the furnace is moved above the sample, allowing a faster increase in the temperature. One end of the tube is connected to the pumping system, while the other end is connected to the gas inlet system and the sample holder. The pumping system, which allows to reach pressure up to 10^{-6} Torr, is composed of a rotary pump (EDWARDS XDS10) in series to a turbo molecular pump (TURBOVAC 50). The pressure inside the reaction chamber is controlled by a vacuum gauge (LEYBOD

VAKUUM). The sample holder is a molybdenum (Mo) ship connected to a thermocouple that allows *in situ* temperature monitoring.

Gas flow rates are controlled using mass flow controllers (MASS FLO 1179A-MKS) that are controlled by a 4-channel MKS 247 controller. From the gas inlet, the gasses are introduced into the reaction chamber with a flow parallel to the sample surfaces. A schematic picture of the experimental setup is reported in Figure 2-1.

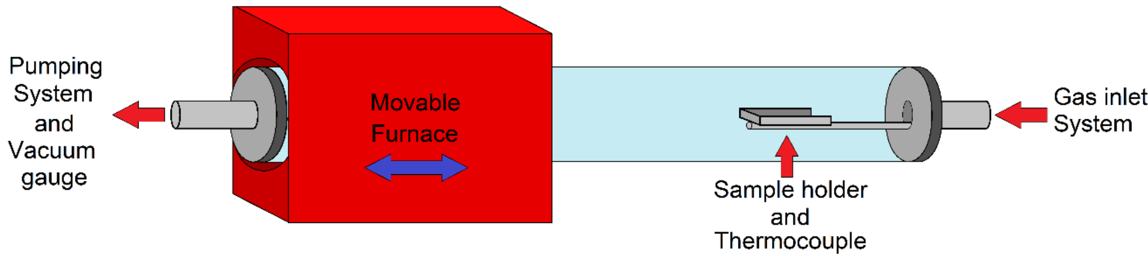

Figure 2-1 Schematic diagram of the reactor.

The silicon substrates have been firstly polished by a 15 min sonication cycle in acetone followed by another sonication cycle in isopropanol to remove all the surface contaminants. The region of the CNT growth on the substrates was selected by the deposition of a 3 nm Ni film by thermal evaporation. After the Ni deposition, the samples have been transferred to the CVD reactor.

The quartz tube has been pumped down to less than 10^{-6} Torr and then the substrates have been annealed at 750 °C for 20 minutes in ammonia flow with rate of 100 sccm, keeping only the rotary pump active. This pre-treatment was necessary to obtain small Ni nanoclusters, fundamental for the realization of small-diameter nanotubes [59]. The actual growth process started when acetylene (C_2H_2) was added to the reaction chamber. The flow rate was fixed to 20 sccm for ten minutes and the temperature was kept equal to the temperature of the annealing process. During both annealing and CNT growth, the pressure inside the chamber has been kept fixed at 5.5 Torr. The furnace is then moved far away from the devices, to cool down the devices to room temperature.

2.2 Carbon Nanotube characterization

A macroscopic inspection of the samples reveals a uniform growth of the CNTs on the silicon nitride surface, which results covered by an opaque black film.

Investigating the microscopic morphology of the sample with a scanning electron microscope (SEM) (Zeiss Leo 1530) we observe that from a top view, the film appears to be formed by a dense and intricate network of nanotubes (Figure 2-2(a)). From a lateral view (Figure 2-2(c)), it is possible to see that the nanotubes are straight and aligned in the vertical direction, forming the intricated network only in the higher part of the film. The nanotube film appeared to have a homogeneous thickness across all its surfaces, but near some edges, the thickness slowly decreases till no more nanotubes are present.

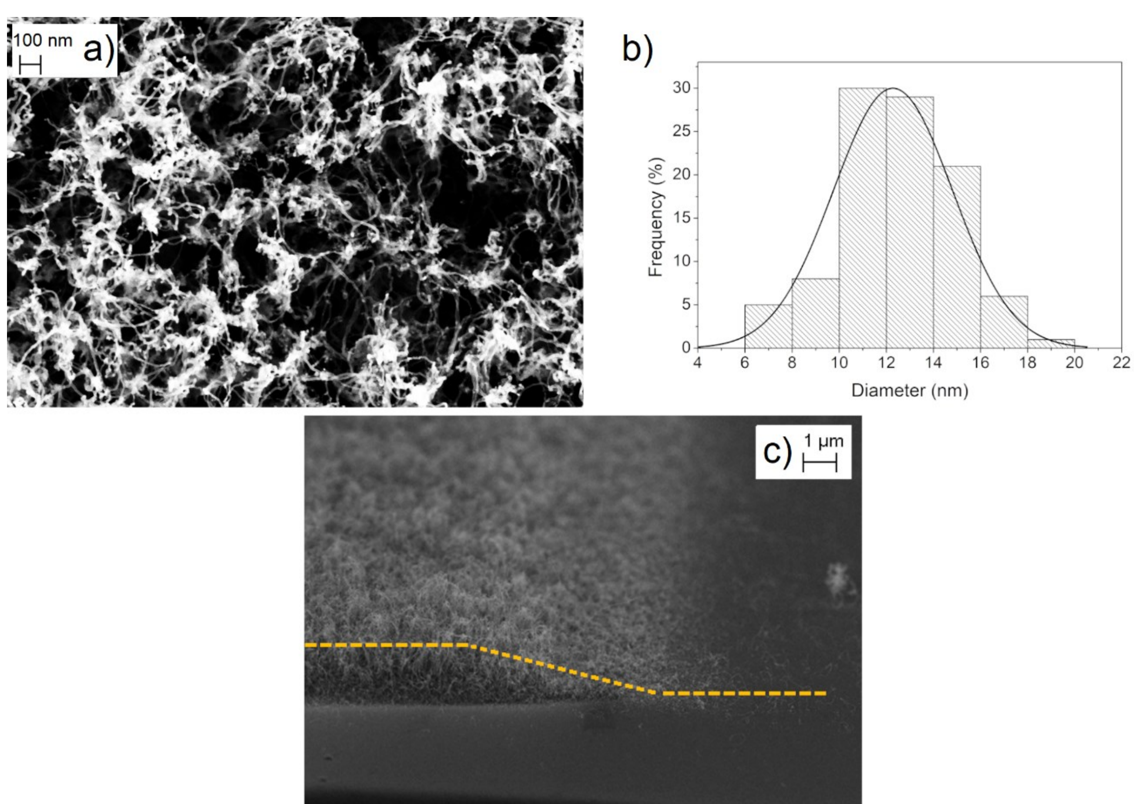

Figure 2-2 a) Top view of the MWCNT film. b) Diameter distribution. c) Lateral view of the film with highlighted the decreasing thickness of the film near an edge.

The average diameter of these nanotubes has been extracted from the SEM images by measuring different structures across the film. The gaussian fit of the diameter histogram (Figure

2-2(b)) allowed to calculate the average diameter (with the statistical error) of the nanotubes. We obtained an average diameter of (12.3 ± 2.5)nm.

The chemical composition of the nanotubes has been analysed using X-ray photoemission spectroscopy (XPS) (PHI 1257) using Mg Kα radiation. The Survey spectrum shows that the film is mainly composed of carbon and oxygen (due to atmospheric contaminants on the film). Is also observable small signals of silicon and nitrogen coming from the substrate.

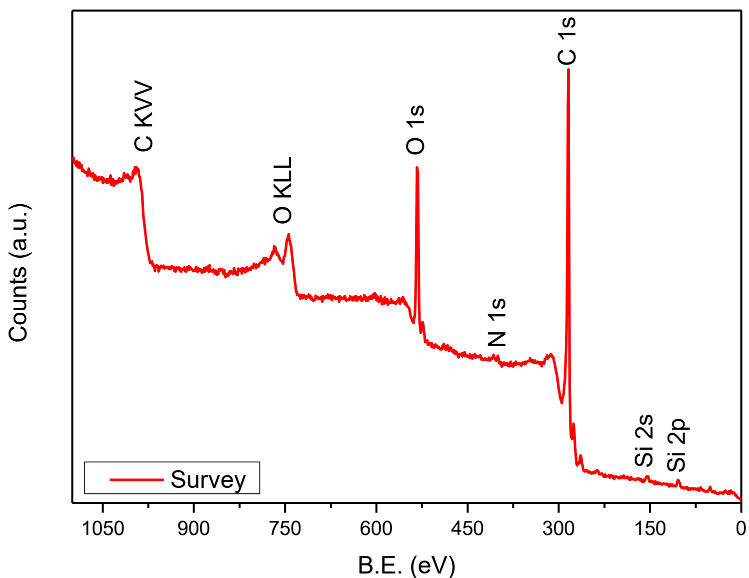

Figure 2-3 XPS survey spectrum of the nanotubes.

Information about the crystal structure of the CNTs and the presence of amorphous carbon was obtained by Raman Spectroscopy characterization. These measurements have been performed using a LabRam Hr high-resolution Raman microscope (HORIBA-Jobin Yvnov) equipped with a 632.8 nm (E=1.96) laser source. Raman spectroscopies confirm the multiwall nature of the CNTs since no Radial Breathing Modes (RBM) (typical of SWCNTs) are detected in the low energy range of the spectrum (100-300 cm^{-1}) [60]. The high-energy modes

present two main peaks attributed to the D and G bands. The presence of defective graphitic structure contributes to the high intensity of the D-band and to the broadening of the G-band.

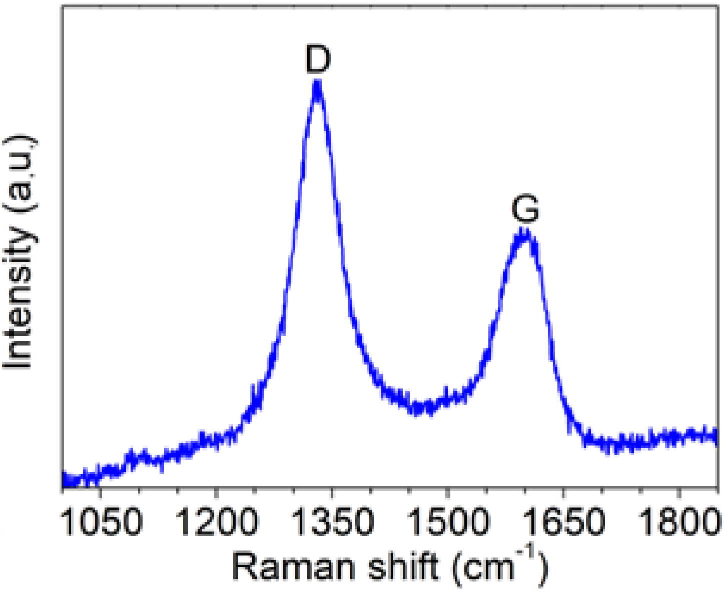

Figure 2-4 Raman spectrum of the MWCNT film.

2.3 Electrical measurements

2.3.1 First device

The electrical measurements have been carried out using a Keithley 236 source-measure unit. This instrument allows to source and measures voltage and current simultaneously, with a sensitivity of 10 μV and 10 fA respectively. All the measures were performed inside a dark box at room temperature and LEDs with different wavelengths were used as light sources.
The measures were performed in a vertical configuration, applying the voltage between one of the pads on the top surface and the back of the device.
The purpose of the first measure was to understand the average response of the device to light. Using an optic fibre, the light of the LEDs has been directed on the device surface, with a spot large enough to cover most of the CNTs film. In this way, possible inhomogeneities in the film are mediated in the final response.

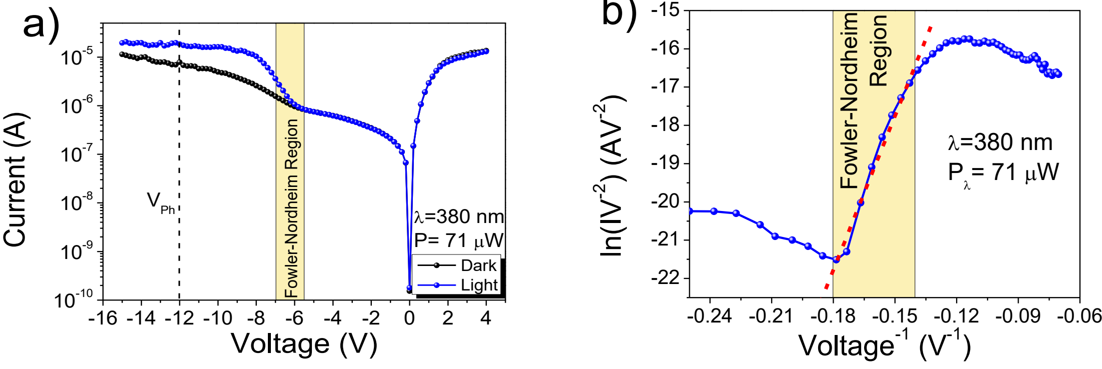

Figure 2-5 (a)I-V characteristic of the device in dark and under illumination by a 380 nm LED. It also reported the value of V_{ph} that was used for that sample. (b) Fowler-Nordheim plot of the "Light" curve reported in (a).

A series of electrical stress at high voltage has been performed to damage the top and bottom Si_3N_4 layer and transform the two junctions into stable tunnel barriers. Figure 2-5(a) shows the I-V characteristic of the first device taken in the dark and illuminated by a 380 nm LED at 71 μW. The I-V characteristic shows a rectifying behaviour with an on/off ratio of 20 at ± 4 V. While the forward current is not affected by the presence of light, the reverse current shows an exponential increase once the voltage drops below -6 V. This increase stops at a certain voltage, where a plateau is reached. The increase in current can be explained by the tunnelling of charges through the insulating barrier of a MIS diode, that in presence of the

external bias, assume a triangular shape. The tunnelling through this type of barrier is described by the Fowler-Nordheim model. The current associated to this phenomenon can be expressed as:

$$I \propto \left(\frac{V}{d}\right)^2 \phi^{-1} e^{-b\frac{d}{V}\phi^{\frac{3}{2}}} \tag{2.01}$$

Where ϕ and d are the heigh and thickness of the barrier, b is a constant ($6.83\ 10^7\ Vcm^{-1}eV^{-3/2}$) and V is the applied voltage [61,62]. It is useful to rewrite the relation in Eq. (2.01) as:

$$ln\frac{I}{V^2} = C - bd\phi^{\frac{3}{2}}\ \frac{1}{V} \tag{2.02}$$

In which is clear that the logarithm of the ratio between the current and the square of the voltage ($ln\ (I/V^2)$) is linear with the inverse of the voltage ($1/V$). In this way the linear behaviour of the photocurrent in the Fowler-Nordheim plot in Figure 2-5(b) demonstrates that the increase of current in presence of light is due to the tunnelling of the photo-charges through the metal-insulator-semiconductor (MIS) barrier generated between the nanotubes, the silicon nitride, and the n-type silicon. With the increasing bias more and more charges are separated and collected, resulting in a linear increase of the current that stops when an equilibrium between generation-collection is reached [61,63,64].

After these initial measurements, we performed a scanning photocurrent imaging of the device [65,66]. The devices have been mounted on a sample holder equipped with two-micrometre screw gauges that allowed precise movements along the x and y direction. This setup was used to move the device under the light coming from an optic fibre, kept at a fixed position. The diameter of the spot above the sample was of about 1 mm. All the device surface has been scanned across a grid of 0.25 mm in the x direction and 0.31 mm in the y direction. The current flowing in the device has been measured as a function of the spot position across the grid and has been successively used to calculate the photocurrent and the associated External Quantum Efficiency (E.Q.E.). The obtained values have been reported in the Efficiency Map in Figure 2-6

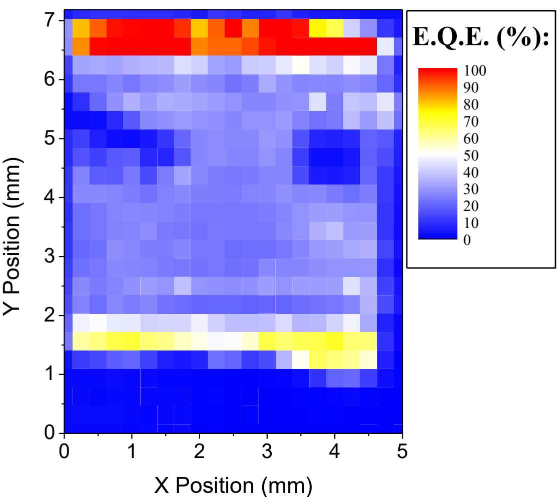

Figure 2-6 External Quantum Efficiency map of the first device. The device presents an average efficiency of 30% but near the top and bottom edges, the value increases and reaches values close to 100%.

The efficiency has an average value of the 30%, comparable to the one calculated from the I-V curves measured in Figure 2-5, but on the top and bottom edges, a significantly higher value is reached, with efficiency near 100%. The higher efficiency appeared in the same region reported in Figure 2-2(b) where the film is thinner. This suggests that a reduction of the film thickness, can be used to improve the average efficiency of the device. For this reason, a simple technique has been developed to reduce the CNT film thickness after the CVD growth. A piece of tape, normally used to exfoliate two-dimensional materials, has been placed above the nanotube film, gently pressed with a cotton swab, and then peeled off. This simple process allows the remotion of the higher tubes present on the film (that remained attached to the tape) leaving only the shorter ones.

2.3.2 Second device

Figure 2-7 (a-c) shows the steps of the thickness reduction process, used to realize the second device. Using a profilometer (Veeco Dektak 6M), we measured the thickness of the film along the blue and red lines reported in Figure 2-7 (c). The measured profiles reported in Figure 2-7 (d) indicates a clear reduction of the film thickness of about 700 nm.

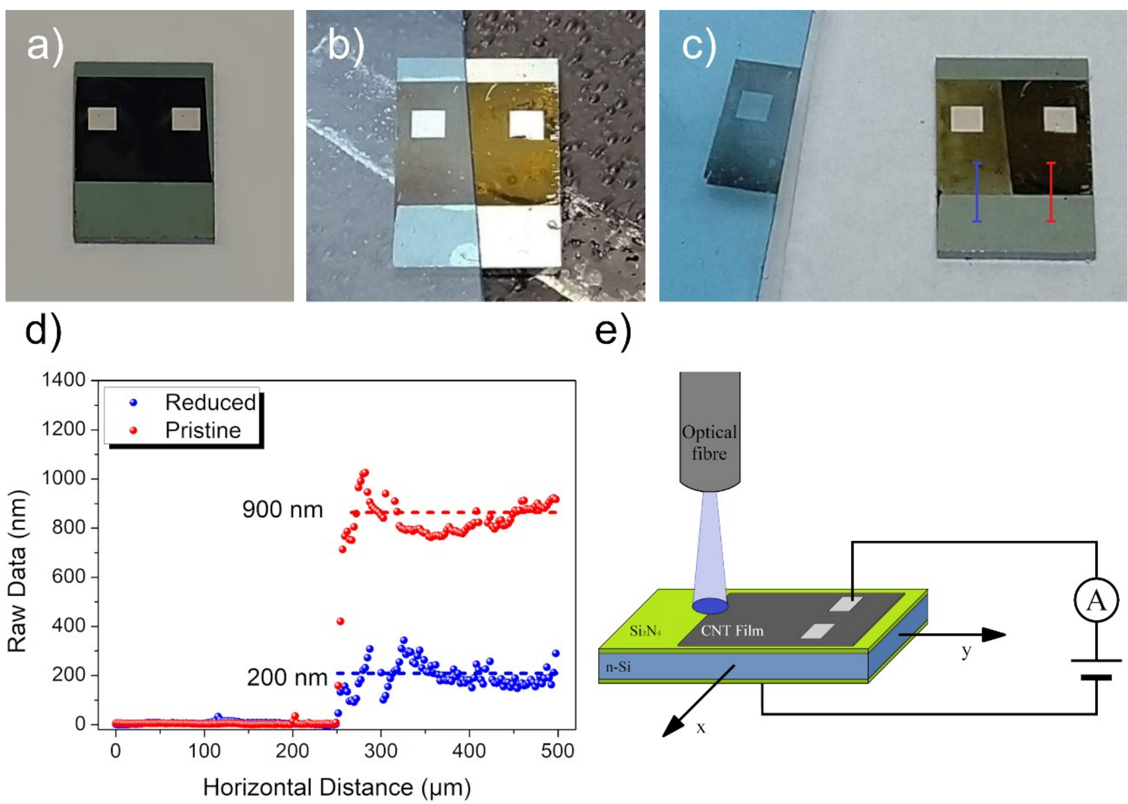

Figure 2-7 Steps of the reduction process: (a) device with pristine CNT film, (b) tape adhered on the device, and (c) tape peeled off next to the device after the remotion. (d) The thickness of the CNT film along the line in (c). (e) The layout of the device and the setup used for the electrical characterization.

SEM images taken at the interface between reduced and unreduced film directly show the different lengths of the nanotubes in the two regions.

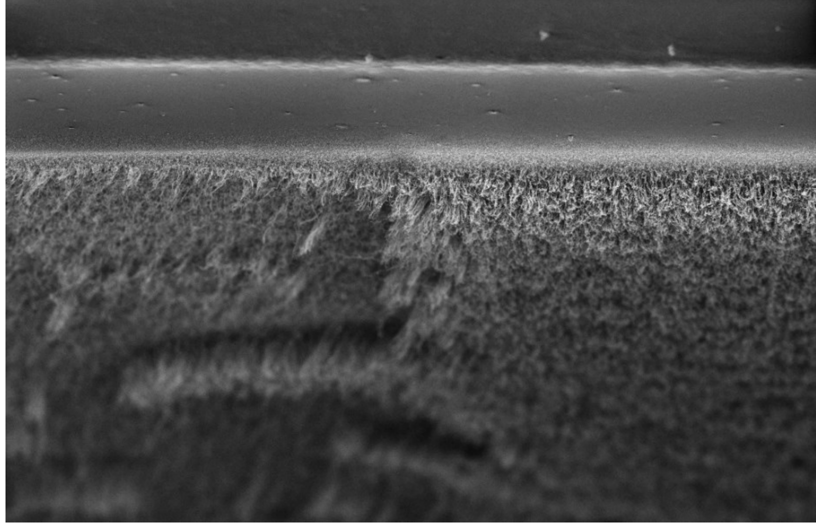

Figure 2-8 SEM images acquired with a 15° tilted angle from the surface showing the different thicknesses of the nanotubes in the reduced and unreduced film.

Figure 2-9 shows the optical images of the film before and after the reduction process, above the relative efficiency map. The maps show that the reduction process allows the device to almost double its efficiency.

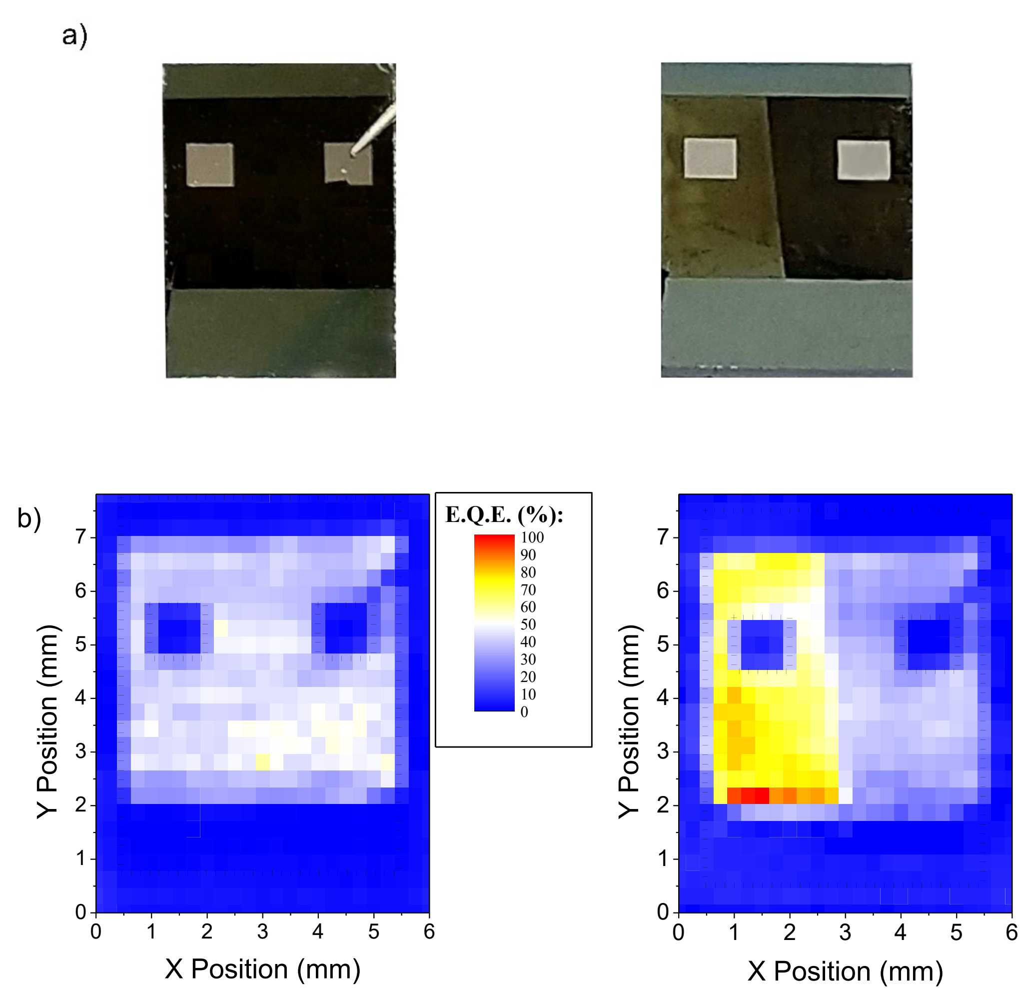

Figure 2-9 (a) Optical images of the device before and after the thinning process. (b) External Quantum efficiency maps of device 2 before (left) and after (right) the CNT remotion. The dotted lines mark the real dimension of the substrate and the metallic pads. Both maps were acquired using the right pad as an electrical contact.

The I-V characteristic of the film has been evaluated in the two regions of the film, using different LED light sources. Figure 2-10 shows the behaviour of the device's currents depending on the spot position. Like the first device, the currents deviate from the dark one only below -6 V and reach a plateau whose intensity depends on the light power and wavelength of the incoming power.

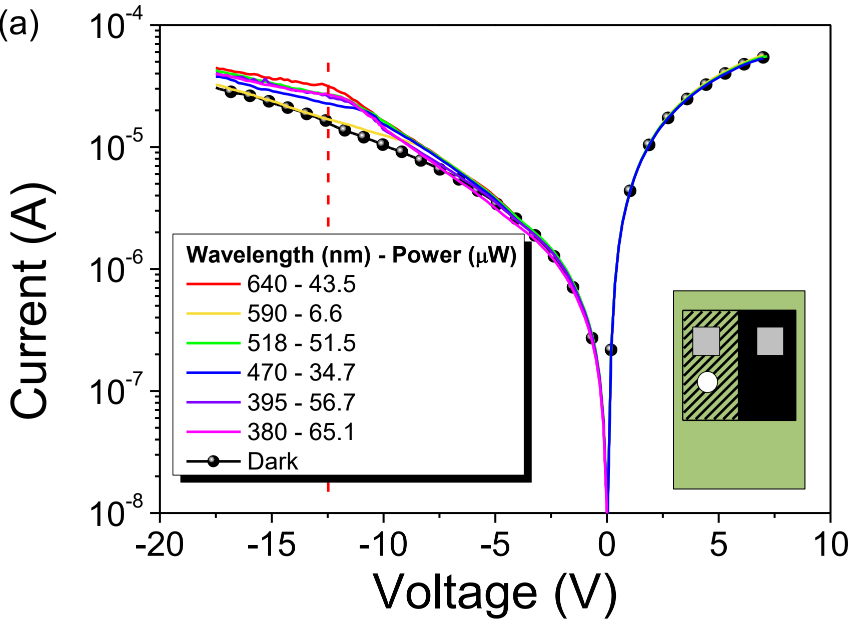

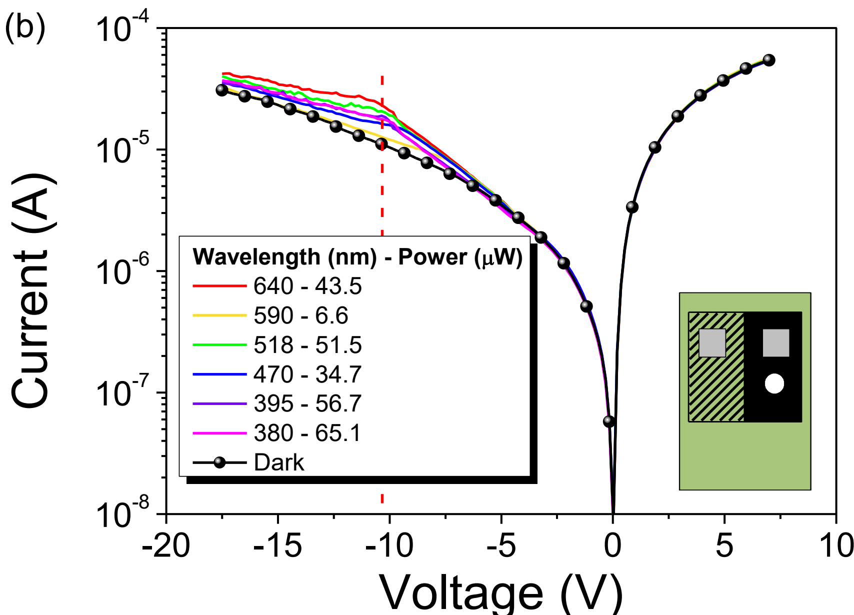

Figure 2-10 Response of the second device to different LED lights(a) I-V characteristic acquired when the spot is located on the reduced film and (b) when the spot is above the unreduced film.

The I-V curves measured in the two regions appear to be quite similar. Considering the red curves in the two graphs (λ=640 nm, P=43.5 nm), it is possible to see that the voltage at which the plateau begins (reported by the dashed line) is slightly different in the two graphs: $-12.5\ V$ for the reduced film and near $-10\ V$ for the unreduced. To better see how the currents at the plateau change between the two graphs we evaluated the average values of the

photocurrent and converted in E.Q.E. to determine the spectral response of the device (Figure 2-11).

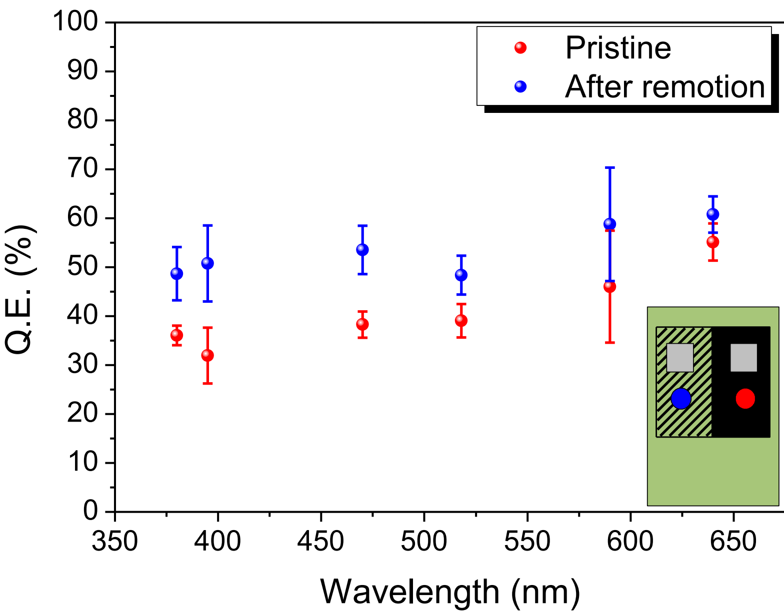

Figure 2-11 Q.E. of the device at the plateau as a function of the wavelength. Red dots represent the values of the E.Q.E. obtained on the pristine portion of the film while the blue dots represent the values from the reduced portion.

This graph shows that the increment of efficiency occurs in all the studied wavelengths. The increase is slightly higher in the near UV region, where the nanotubes have a higher absorbance [21]. To have a clearer insight into the differences between the response of the two regions a new series of measures have been done using laser sources. The higher power of the lasers allowed to better see the shape of the photocurrent in the device. Figure 2-12 shows that the photocurrent measured while illuminating the reduced portion of the film reaches a higher value at the plateaux (i.e., a higher external quantum efficiency), but since the current grow rate is smaller, a higher bias voltage is required to reach the plateau (as inferred from Figure 2-10). It is possible to recognize two regimes in the device: one at low reverse bias, where the unreduced film has a higher response, and one at higher reverse bias where the reduced film is more efficient. This phenomenon can be attributed to the different behaviour of the two films in the process of charge generation and collection. For example, the reduced film, due to the lower thickness will transmit a higher number of photons to the substrate, resulting in higher efficiency. But this higher efficiency comes with a cost, the reduced

number of nanotubes will increase the resistance of the film, and the device will then need a higher voltage to be able to collect all the generated photocharges.

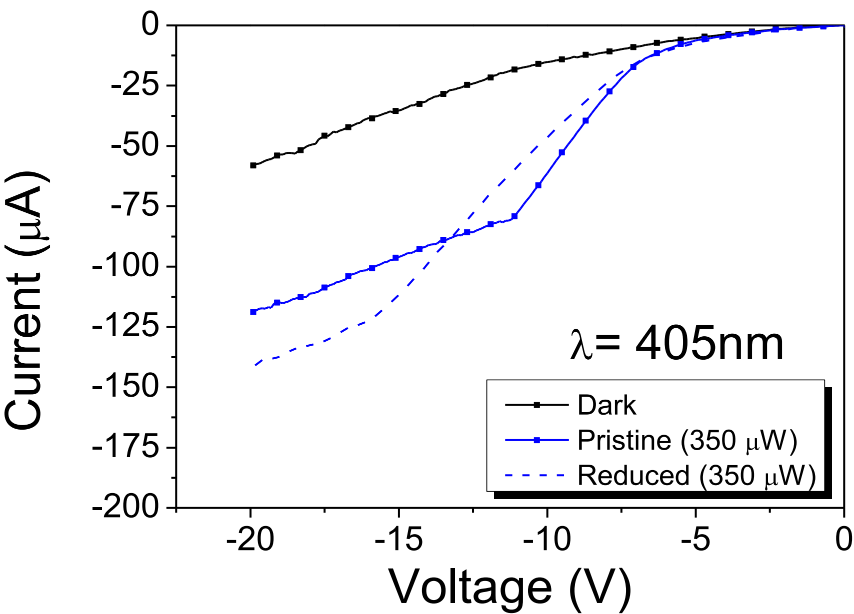

Figure 2-12 Detail of the reverse current measured when the same light power is above the reduced and the pristine film.

All the measures presented to this point are acquired using the right pad (the one on the unreduced film). To complete the analysis other measures were taken on the left pad and compared to the previous one. Figure 2-13 reported the I-V curves acquired in dark and under the illumination of the device contacted from the two pads. The dotted lines represent the dark currents of the device. The dark currents measured in the forward region exhibit a big difference depending on which pad was used: the currents taken from the right pad (the one in contact with the unreduced film) are almost an order of magnitude greater than the currents measured from the left pad. The reduced current measured from the left pad can be explained by a worsening of the contact between the nanotubes and the metallic pad after the reduction process. The reverse dark currents do not present significative differences, they have the same behaviour and almost the same intensity. In presence of light, the currents measured from the pads behave similarly to what already observed, independently of which pad is used: when the spot is located above the unreduced film the plateau is reached sooner, but its value is always smaller than that reached when the spot is on the reduced film. The only appreciable difference is that the currents measured from the left pad are always smaller than that measured from the right one.

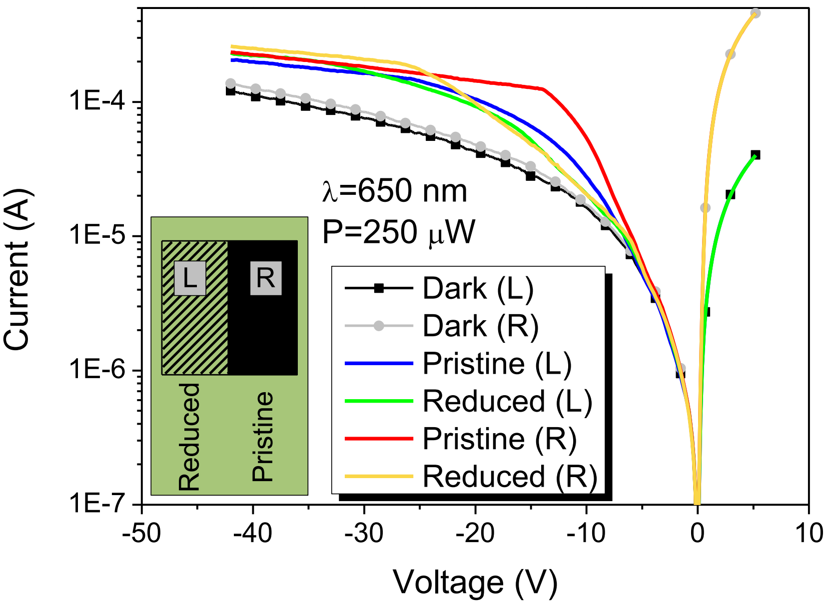

Figure 2-13 I-V curves acquired using both pads in dark and under the light of a 650 nm laser at 250 μW.

2.3.3 Third device

This device was realized with multiple iterations of the reduction process. This has been made to understand if the E.Q.E. could be further improved by repeated reduction process.

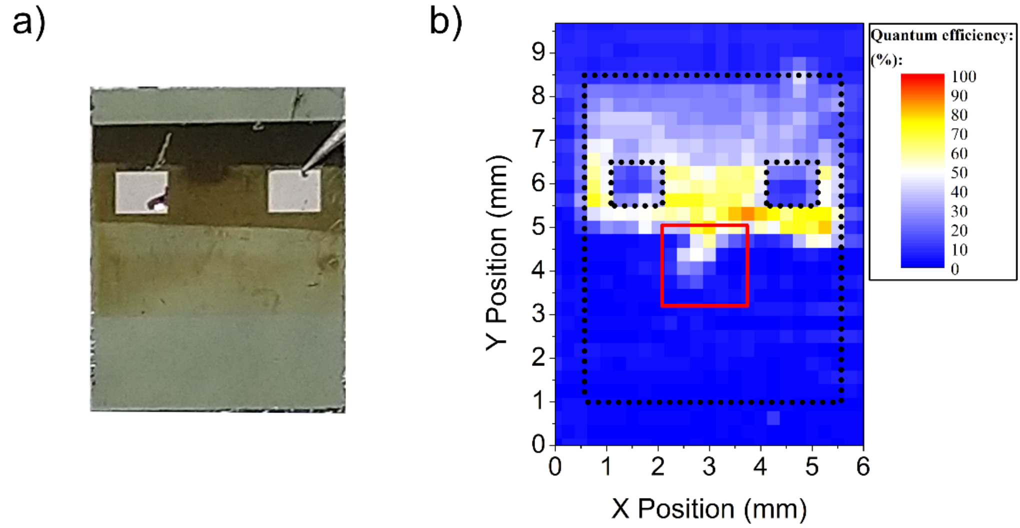

Figure 2-14 (a) Optical image of the third device, the three different zones are visible: the first with the unreduced film on top, the single time reduced at the middle, and the two times reduced at the bottom. (b) Q.E. map of the third device.

The device has been obtained by repeating the reduction two times, shifting the position of the tape at each iteration. In this way, we obtained a film composed of an unreduced portion on top, a one-time reduced portion in the middle and a two-times reduced portion at the bottom. The three different regions can be recognized in Figure 2-14 (a). The efficiency map shows that the unreduced and the one-time reduced regions have behaviours similar the second device (i.e., 30 % efficiency on the unreduced region that grows to almost 60% on the one-time reduced). Completely different is the behaviour of the two times reduced region, where E.Q.E. drops to zero.

To understand this phenomenon, high-resolution SEM images were taken on the different film regions. The images show that the morphology of the film changes drastically from one region to the other (Figure 2-15). In the two-time reduced film, the substrate is completely exposed. The only structures left are short nanotubes and small particles, that can be nanocluster of the precursor metal or graphitic residue. In the one-time reduced film, the nanotubes are still present and form a network above the substrate. The substrate, recognizable by the globular structure seen also in the two-time reduced film, is still exposed, while in the unreduced film the nanotubes are so long that the substrate is no longer observable.

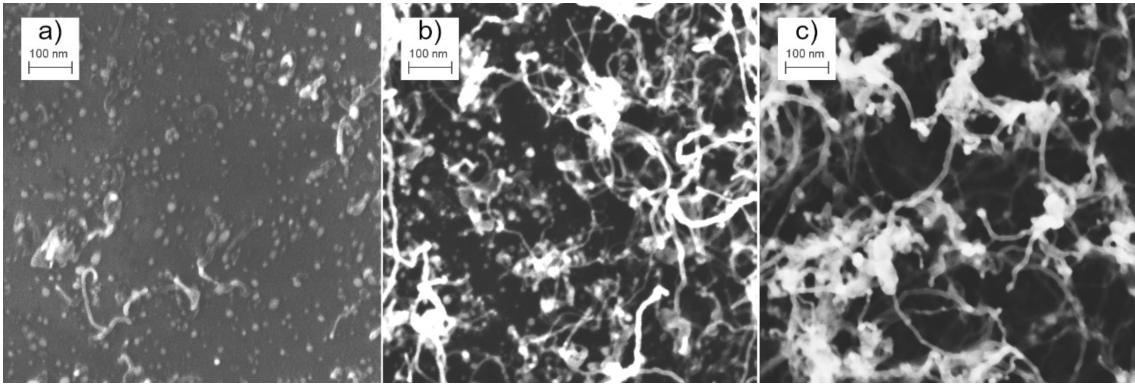

Figure 2-15 High-resolution SEM images of the CNTs film after the remotion process. (a) Two times reduced film: there are only short nanotubes and numerous Ni nanoclusters. (b) Single-time reduced film: the nanotubes are longer and create an intricated net above the visible substrate. (c) Unreduced film: the nanotubes are longer, and the substrate is no longer visible.

The red square in the efficiency map reported in Figure 2-14 (b) highlights a region that extends for over one millimetre inside the two-times reduced film, where the efficiency is

different from zero. Observing this region with the electron microscope is possible to see that a nanotube strip, around 1 millimetre long and 20 μm wide is present on that exact point.

Figure 2-16 Nanotube strip that extends almost 1mm from the one-time reduced film border to the two-times reduced region.

The presence of this strip, probably due to some defect on the tape used for the remotion, highlight the accuracy of the efficiency map acquired, and the ability of μm sized portion of nanotube film of collecting a high photocurrent. This is important because indicates the scalability of this device, and its possible implementation in integrated circuits.

2.4 Conclusions

Three devices have been made by growing multi-walled carbon nanotubes on silicon substrates. The performed electrical measures showed that the devices begin to produce a photocurrent once a reverse bias of -6 V is applied between the top electrode and the back of the device. The linear behaviour in the Fowler-Nordheim plot shows that the photocurrent is due to charges tunnelling through the Si_3N_4 layer, thinned by repeated electrical stress. The measured efficiency maps and the film morphology of the first device suggested that the maximum efficiency could be boosted by a reduction of the film thickness. For this reason, we developed a simple and inexpensive reduction process, inspired by the scotch tape method used for the exfoliation of two-dimensional materials.

This method has been used on a second device to see if was effectively possible to increase its efficiency. The efficiency of the device has been calculated before and after the reduction process and reported in efficiency maps. These maps show that the reduction allowed an increase of the maximum efficiency of roughly the fifty per cent of the initial value. The I-V characteristic acquired on this device showed that the increase in efficiency is present for all the wavelengths under consideration, with a slightly higher increase in the near UV region. Another important observation was the presence of the different behaviour of the photocurrent depending on the position of the spot above the film. The unreduced film offers the possibility of reaching higher efficiency, but as a trade-off, the plateau of the photocurrent is reached at higher voltages.

To see if higher external quantum efficiency could be reached by multiple iterations of the reduction method a third device was realized. By applying the reduction method twice, we were able to make a device with an unreduced, a one-time reduced and a two-times reduced film on the same device. The efficiency map of this device showed that the second reduction brings the efficiency to zero. Using electron microscopy, it was possible to see that the nanotubes in that region were completely removed.

From these devices, we were able to get a better insight into the role of nanotubes inside this type of detectors. The nanotubes act as a semi-transparent metallic layer of the Metal-Insulator-Semiconductor (MIS) junction that forms on the device. The thickness of the film play a major role because with thinner the film, a higher amount of photons is allowed to reach

the silicon substrate and produce an higher number of photocharges, resulting in higher efficiencies. As a trade-off, the higher resistance of the film reduces the efficiency of the charge collection process, so a higher bias will be needed to collect them and reach the plateau. The proposed method offers a simple way to improve the efficiency of the device but has still some flaws. The improvement is not tuneable, and successive iterations can lead to the complete remotion of the film, consequently ruining the detector.

Chapter 3. Photodetectors by transfer printing of carbon nanotube film

The results obtained from the previous chapter made clear that a better control on the film thickness is one of the main parameters that has to be controlled for the device optimization. For this reason, the devices in this chapter are obtained by the deposition of a thin film of SWCNT above a silicon substrate using the transfer printing technique [67,68]. In this method, the nanotubes have been initially dispersed in an aqueous solution and then vacuum filtered to realize the film above a membrane filter. Varying the amount of filtered solution is possible to produce film with different thicknesses. After the filtration, a filter piece has been used to transfer the nanotubes above the substrate. Another peculiarity of this method is that the contact between the nanotube film and the substrate can be achieved without the high temperatures needed for the CVD growth of nanotubes. In this way, problems connected to the thermal stress like the diffusion of catalyst metal inside the silicon substrate can be completely avoided.

3.1 Device realization

3.1.1 Single-walled Carbon nanotubes water dispersion

To realize a thin film of nanotubes above a membrane filter is required to have a homogeneous dispersion of tubes in a liquid medium. Since the nanotubes are insoluble in water and because after growth are usually grouped in bundles, the realization of a stable and homogeneous dispersion of the tube is not an easy task. The condition of homogeneous dispersion is achieved when the solution has reached the point of nano-dispersion, in which the CNTs are individually dispersed in the solvent [69]. To separate the nanotubes both mechanical and chemical approaches can be used. The mechanical approach uses high-frequency vibration to separate the bundles, while the chemical one uses surfactants or functionalization to improve the wettability of the material, reducing the tendency to agglomerate in the solvent [54,70,71].

In our procedure, an anionic surfactant, the sodium-dodecyl-sulphate (SDS, from Sigma-Aldrich) was mixed with water with a 2% weight-volume ratio. The solution has been sonicated for some minutes until all the SDS was dissolved in the solution. Then a SWCNT powder was added to the mixture, reaching an 80 μg/mL concentrated solution. To obtain the homogeneous dispersion, the solution has been tip ultra-sonicated for one hour in ice bath. The sonication was fundamental to allow the SDS molecules to surround the nanotubes, separate and keep the nanotubes dispersed inside the water. Then the solution has been left overnight to allow the bundled nanotubes to precipitate.

Figure 3-1 Vials containing water dispersions of MWCNT with the addition of SDS and without. In the vial on the right, all the nanotubes have precipitated at the bottom.

After the remotion of the small deposit of bundled nanotubes, the solution resulted homogeneous and does not show any kind of precipitates even after several months.

3.1.2 Vacuum filtration

A low vacuum filtration process has been used to deposit the nanotubes above a membrane filter (Figure 3-2).

Using a mechanical pipette, different aliquots of dispersion have been introduced in the filtration system. The system is composed of a filter head where the membrane (Durapore PVDF, pore size 0.22 μm, diameter 47 mm) can be placed and the vacuum can be applied through an outlet port. The head can be attached to a cylinder funnel by a metal clamp to contain the solution that has to be filtered, and to a bottle to collect the filtered solution.

A rotary pump connected to the filtration system has been used to facilitate and make the filtration faster. The nanotubes will automatically form a random homogeneous network

above the membrane filter while the solvent can pass freely through the membrane. At this point, the film has still some residue of the surfactant needed for the dispersion, observable by the formation of a white foam below the filter. This must be removed since its presence can affect the electronic properties of the CNT film. A washing process has been used to clean the film. Making use of the same filtering apparatus, a solution of ethanol, methanol, and distilled water (15:15:70) has been passed through the filter to remove as much surfactant as possible. The process has been repeated till no more SDS foam was present.

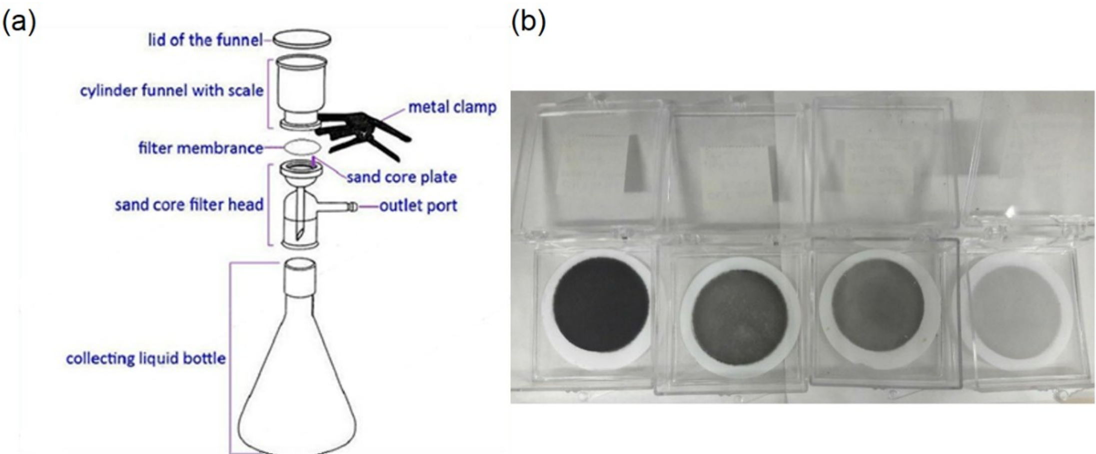

Figure 3-2(a) Schematic of the vacuum filtration apparatus. (b) Examples of filters obtained by a different aliquot of dispersion. Darker films correspond to higher volumes of filtered solution.

By varying the aliquot of solution filtered is possible to obtain a film with different thicknesses and consequently different colours, where darker filters correspond to thicker films.

3.1.3 Dry transfer printing

Once dried out, the filters are stable, and no sign of degradation has been observed. The film is now ready to be deposited on a substrate. A piece of the filter can be easily cut with ordinary scissors in the desired shape and dimension. To obtain the transfer, the piece of filter must be deposited on the substrate, keeping the membrane filter on top. Then using a cotton swab, the membrane can be soaked with water and ethanol. This improves the adhesion of the nanotubes to the substrate and their evaporation facilitates the detachment of the membrane. Moreover, a glass slide can be used to press the wet membrane over the substrate to improve the adhesion of the film. After some minutes the membrane dries out and can be peeled off, leaving the CNT film above the substrate.

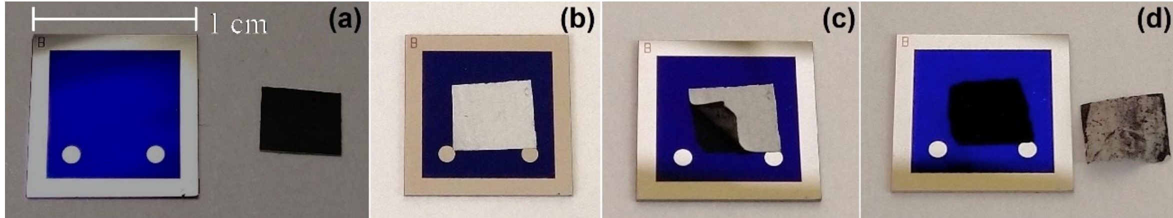

Figure 3-3 Phases of the dry transfer process. (a) Substrate and piece of SWCNT filter before the transfer. (b) SWCNT film was pressed over the substrate surface after wetting the membrane with water and ethanol. The film has been placed directly in contact with the metallic pads to facilitate the connection with the measurement equipment. (c) Peel-off of the membrane. (d) The device with the deposited SWCNT film and membrane after the process.

The transfer process is very simple and allows the deposition of films with variable thickness and scalable sizes. Depending on the nanotube used in the initial dispersion, it allows to create films of single or multi-walled nanotubes. In principle also other nanostructured materials can be added to the nanotube solution or simply used by themselves to realize even different types of devices.

3.1.4 Wet transfer printing

In some cases, when the thickness of the nanotube film is very small, or in general, the adhesion with the filter membrane is higher than that reached with the sample surface, the dry transfer cannot be achieved. So, when the membrane is peeled off, also the film is removed. Especially when thinner films are needed to be deposited, a modification of the deposition method is required. One solution is to remove the filter membrane chemically, without the mechanical peel off. This can be easily done using filter membrane made by cellulose acetate. Due to the solubility of this material in common solvent like acetone [72,73] is possible to remove the filter from the substrate without the mechanical peel off. The initial steps of the deposition are the same of the dry version, the portion of filter is cut and deposited on the substrate with the nanotube facing down, then slightly wetted with water and finally pressed with a glass slide. At this point the substrate is submerged in vial glass filled with acetone and left until the membrane is completely dissolved. The process can be accelerated warming up the acetone.

3.2 Film characterization

After the deposition of the nanotube film above the substrate, we proceeded with its characterization. We investigated the morphology of the film using a field emission scanning electron microscope at an accelerating voltage of 5 kV. At low magnification the film appears highly corrugated, with asperities and ripples recognizable by the lighter contrast in the Figure 3-4 (a). The film covers large areas of the surface without leaving exposed parts. Above the nanotubes are recognizable some particles with micrometric dimension due to resiudes of the filter membrane trapped into the film surface. Looking at the film with higher magnification is possible to see that the nanotubes are randomly oriented and form an intricated three-dimensional net structure (Figure 3-4 (b)).

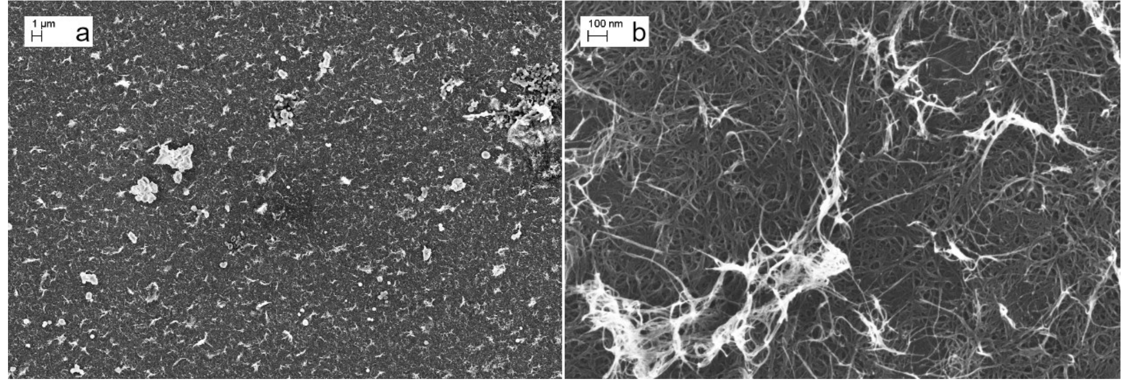

Figure 3-4 a) SEM image at low magnification of the SWCNT film. The nanotubes cover the substrate surface entirely; it is possible to see some residue of the membrane used for the transfer process. b) SEM image at high magnification of the SWCNT film.

Using an X-ray photoemission spectrometer equipped with Mg Kα radiation we checked the chemical composition of the film, especially looking for any remaining of the surfactant molecules. The survey spectrum reported in Figure 3-5 shows that the strongest signal comes from the carbon (C 1s) of the nanotubes, with a smaller one coming of oxygen (O 1s) due to atmospheric contaminants. Very small signals come also from nitrogen and silicon, due to the exposed substrate surface. Figure 3-5 (b) shows the deconvoluted XPS spectrum of the core level C 1s. The spectrum has been fitted by the sum of six signal: aromatic rings carbon (C=C/C–C, 284.8 eV), hydroxyl groups (C-OH, 285.9 eV), epoxy groups (C=O, 288.2 eV), carboxyl groups (C=O(OH), 289.3 eV) and the π-π^* shake up (291.1 eV).

Figure 3-5 (c) shows the valence electron energy loss spectrum (EELS) taken from the SWCNT film. The spectrum can be understood by comparing it with typical graphite EELS

spectra. Is possible then to attribute the peak at 5.8 eV to the excitation of the π bound electrons, while the broad peak centred at 25.5 eV to the excitation of the (σ+π) bound electrons [74].

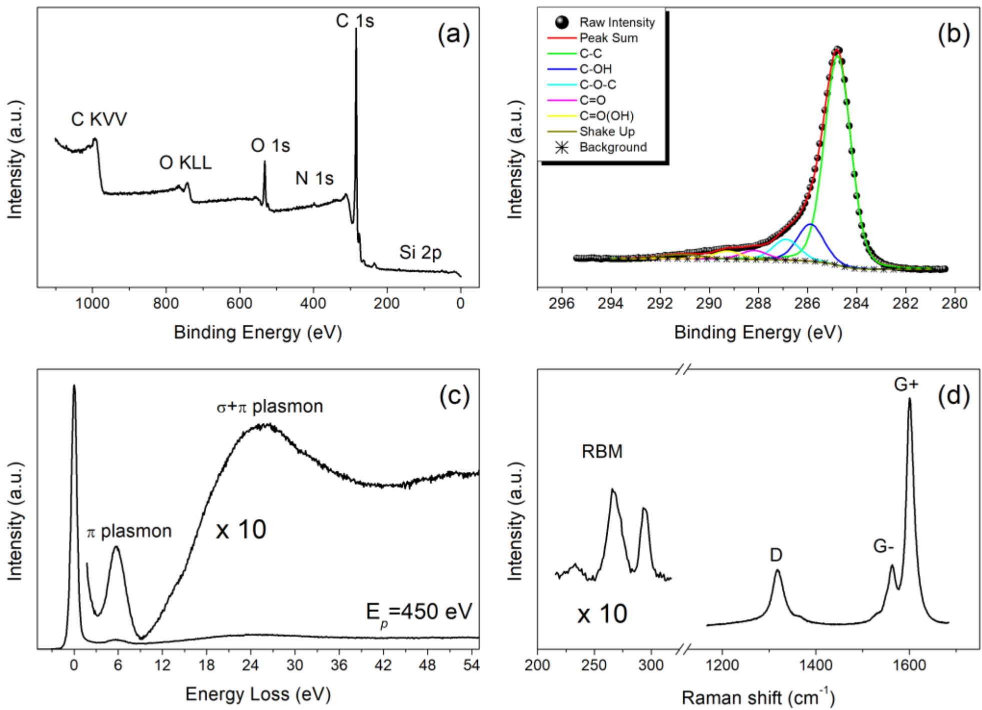

Figure 3-5 (a) Survey spectrum of SWCNT film, are evident the carbon signal, with presence of oxygen and nitrogen due to atmospheric contaminants. (b) C 1s deconvoluted spectrum. (c) Electron Energy Loss Spectrum acquired on the film. (d) Raman spectra.

To determine the quality of the SWCNT powder, micro-Raman spectra were taken using a LABRAM spectrometer with a λ = 633 nm (1.96 eV) excitation line and were calibrated by the Raman peak of crystalline silicon. The Raman spectrum at high frequency of the SWCNT film is reported in Figure 3-5 (d) and shows the typical D and G bands of carbonous material. The D band, attributed to amorphous carbon is less intense that the G band, indicating the high quality of the used nanotubes and the G band shows a splitting in two peaks: the G+ and G- associated respectively with carbon atom vibration along the axis and along the circumferential direction of the SWCNT [60,75]. In the low frequency region are observable the radial breathing modes (RBM), that are observable in SWCNT. Using the phenomenological relation (3.01) is possible to determine the tube diameter d starting from the RBM frequency ω [21]:

$$d(nm) = \frac{234}{\omega(cm^{-1}) - 10} \tag{3.01}$$

The following table resumes the diameter, the chiral vector index and the nature associated to the most intense RBM observed in the Raman spectrum.

ω (cm^{-1})	***d* (nm)**	***(n, m)***	**Type**
267.2	0.91	(8, 5)	Metallic
294.3	0.82	(9, 2)	Semiconductor

Table 3-I RBM frequency (ω) obtained from the most intense lines in the Raman spectrum and the evaluated diameter (d), chiral index (n,m) and nature of the SWCNTs.

3.3 Device characterization

The device has been realized depositing a SWCNT film above silicon substrate using the Dry transfer printing method. A different substrate has been used for these devices. Since there have been no thermal stresses involved with the deposition, the thick nitride layer of the substrates used in the last chapter did not allow the formation of the junction even after severe electrical stresses. For this reason, we used a substrate composed by a 1 cm^2 n-doped silicon wafer (300 µm thickness,2300-3150 Ωcm resistivity) with the top surface covered by a 60 nm Si_3N_4 insulating layer. Two metallic pads on the top surface and a metallic bottom surface (Ti 30 nm/ TiN 50 nm/ Ti 20 nm/ Pt 100 nm) were used for the electrical measurements.

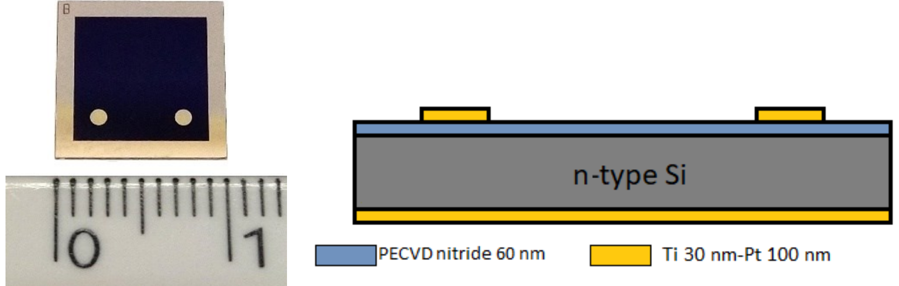

Figure 3-6 Optical image of the substrate and relative cross-section.

The SWCNT film has been deposited simultaneously above the nitride surface and the metal pads, that were used as electric contacts. The behaviour of the vertical heterostructure has been electrical characterized both under the illumination of different light sources and as a function of the temperature.

3.3.1 Electrical measurements

The electrical behaviour of the nanotube film has been tested using the configuration reported in Figure 3-7(a). The I-V characteristic of the nanotube film alone has been measured applying a voltage bias between the metallic pads and by measuring the currents. The measures have been performed both in dark and under the white light of a supercontinuum laser (SuperK COMPACT by NKT PHOTONICS Blokken 84 DK-3460 Birkerød). The film shows a linear behaviour, indicating the formation of ohmic contacts between the metallic pads and the nanotube film. As reported in Figure 3-7(b) the current in the film does not

varies once illuminated. The high conductance of the film does not allow the detection of a photocurrent.

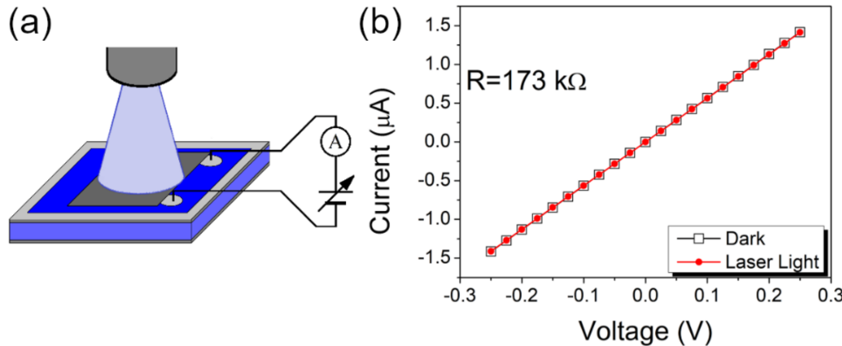

Figure 3-7 (a) Pad to pad horizontal measurement configuration. (b) I-V characteristics of the SWCNT film in the dark and illuminated by a white light (wavelengths in the range 450 nm to 2400 nm, with an intensity of 2W/cm^2).

After the study of the nanotube film, we focused on the electrical characterization of the device. One of the top pads has been used with the back of the device as the electric contacts (Figure 3-8(a)) to measure the behaviour of the vertical SWCNT-Si_3N_4-n Si-metal hetero-structure. The device has been initially subjected to a series of voltage sweep in the range $(-40\ V, +7.5\ V)$ until a reproducible behaviour of the dark current was reached. The electrical stress caused by these sweeps induced a local thinning or breakdown of the Si_3N_4 layer underneath the nanotube film and the metallic pad, that now can be considered as an ultrathin tunnelling layer able to withstand a voltage drop and transmit electrical current [76]. The SWCNT-Si_3N_4-Si heterostructure on top of the device will behave like a Schottky MIS (metal-insulator-semiconductor) structure, while the Ti/TiN/Ti/Pt-Si junction on the back became an ohmic contact.

The I-V characteristic of the device in this configuration has been measured both in dark and under the light of various LEDs with different intensities (Figure 3-8(c)). In the forward region the current quickly reaches high values, whereas in the reverse bias very small currents are measured. Three regions can be highlighted in the reverse current. The first region is in the range $(-7.5\ V, 0\ V)$, where the current is so small that only the noise floor of the experimental setup can be measured (with values around the nanoampere). In the second region, $(-10V, -7.5\ V)$, the current exponentially increases for more than an order of magnitude and then remain constant in the last region $(V < -10\ V)$ with currents values around twenty nanoampere. The device shows an outstanding rectification, with an on-off ratio of 10^4 at $\pm 5\ V$.

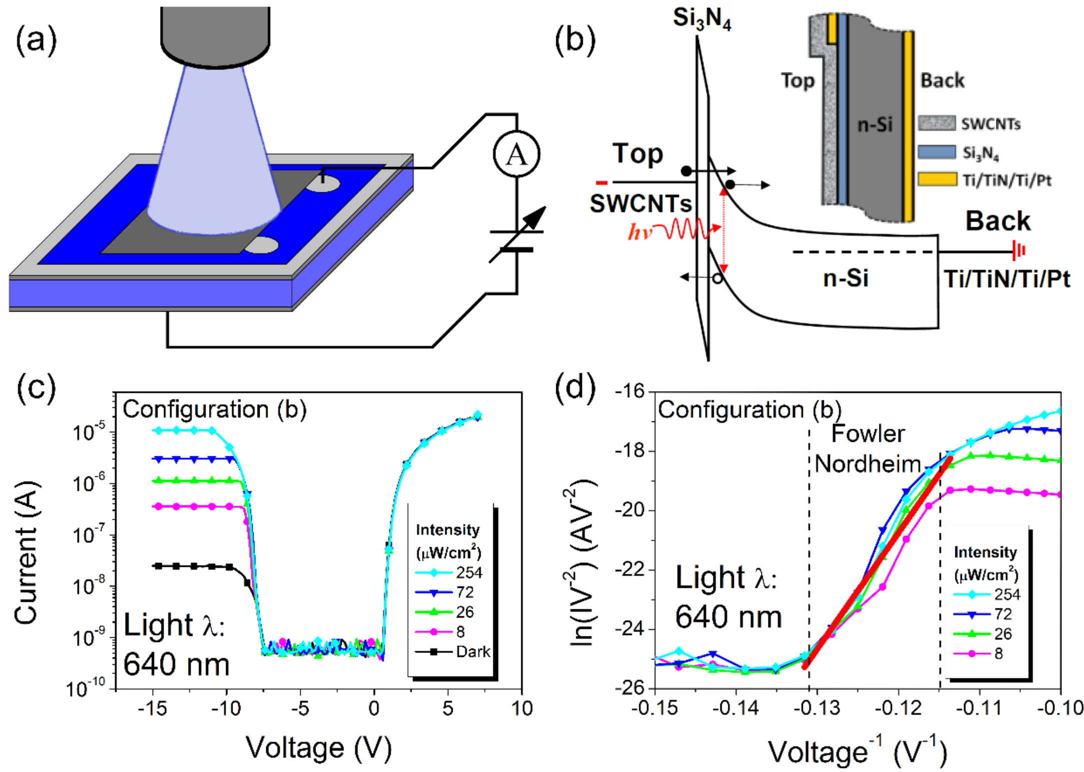

Figure 3-8 (a) Top-Back vertical measurement configuration. (b) Band diagram of the device in reverse bias showing tunnelling through the top barrier and photogeneration in the top depletion layer (the back contact is assumed ohmic). (c) I-V characteristics of the SWCNT-Si_3N_4-Si MIS structure in the top-back configuration under 640 nm light at different light intensities. (d) Fowler-Nordheim plot of the I-V curves in (c) around $V = -7.5\ V$ (the red straight line $y = 26 + 392\ x$ is the fit of 26 $\mu W/cm^2$ curve).

The exponential growth in the second region of the reverse current is attributed to the tunnelling of charges through the MIS barrier, which ends up in saturation due to the series resistance [63]. A schematic representation of the structure's band is reported in Figure 3-8(b). The current in this region is described by the Fowler-Nordheim (FN) model. This model describes the tunnelling of charges trough the triangular barrier generated at the MIS junction under the application of an external field. The current in the junction can be described as:

$$I \propto \left(\frac{V}{d}\right)^2 \phi^{-1} e^{-b\frac{d}{V}\phi^{\frac{3}{2}}} \tag{3.02}$$

By knowing the barrier heigh ϕ, the thickness of the nitride layer d can be extrapolated from the slope of the linear fit of the data in the FN plot ($\ln\frac{I}{V^2}\ vs\ V^{-1}$). A barrier height of 3 eV can be estimated from the difference between the work function of the nanotubes ($\phi_{CNT} =$

$4.8\ eV$) [77] and the electron affinity of the silicon nitride ($\chi_{Si_3N_4} \sim 1.8\ eV$) [78]. We estimate that the nitride layer has been reduced from an initial value of 60 nm to less than 10 nm. When the device is illuminated, the saturated reverse current below $-7.5\ V$ reaches higher values, with steps that depends on the intensity of the incident light intensity. This increase is due to photogeneration of charges in the depletion layer of the device, that enhances the measured current. When is illuminated by a 640 nm light, in the range between $(-7.5\ V, 0\ V)$, the currents measured are always below the noise floor, so it is not possible to claim if an actual photocurrent is present.

LEDs light sources with wavelengths in the range 380-640 nm at different powers were used to test the response of the device in the near UV-Visible region of the light spectrum. The photocurrent produced by the different lights has been calculated as the differences between the current measured when the device is illuminated (I_{light}) and the dark current (I_{dark}) and plotted as a function of the incoming light intensities. As reported in Figure 3-9(a) the photocurrent grows linearly with the incoming light intensity for all the wavelengths and reaches higher values for light in the near IR region. The values of photocurrent have been used to determine the external quantum efficiency (E.Q.E.) of the device. As consequence of the high linearity of the photocurrent with respect to the light intensity, the E.Q.E. reported in Figure 3-9(b) is independent from the incident light intensity. The average E.Q.E. are reported in the inset of Figure 3-9(b), a maximum value of 65% is reached for the red light, with decreasing efficiency with decreasing wavelengths.

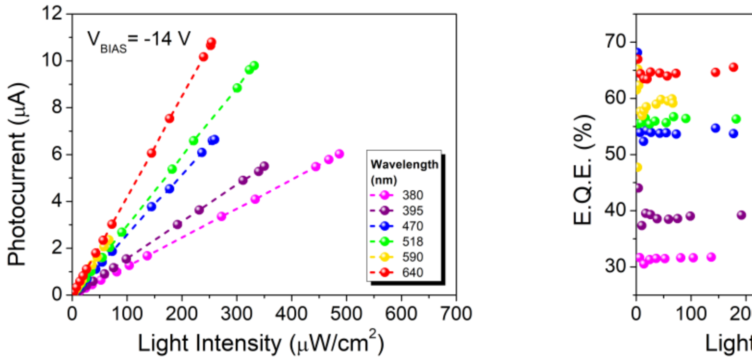

Figure 3-9 (a) Photocurrent vs. light intensity in reverse bias ($V = -14\ V$) for different wavelengths. (b) Calculated E.Q.E. as a function of the light intensities for different wavelengths and (inset) average E.Q.E. as function of the wavelengths.

The values of efficiency are competitive with that observed in other CNT-Si detectors obtained with more complex and expensive techniques like CVD growth or arc discharge method [79,80].
The device has been also characterized using a different experimental setup. In this case a Keithley 4200-SCS was used as source measure unit and a supercontinuum laser (SuperK compact by NKT photonics) with wavelengths in the 400-2400 nm range was used as light source.

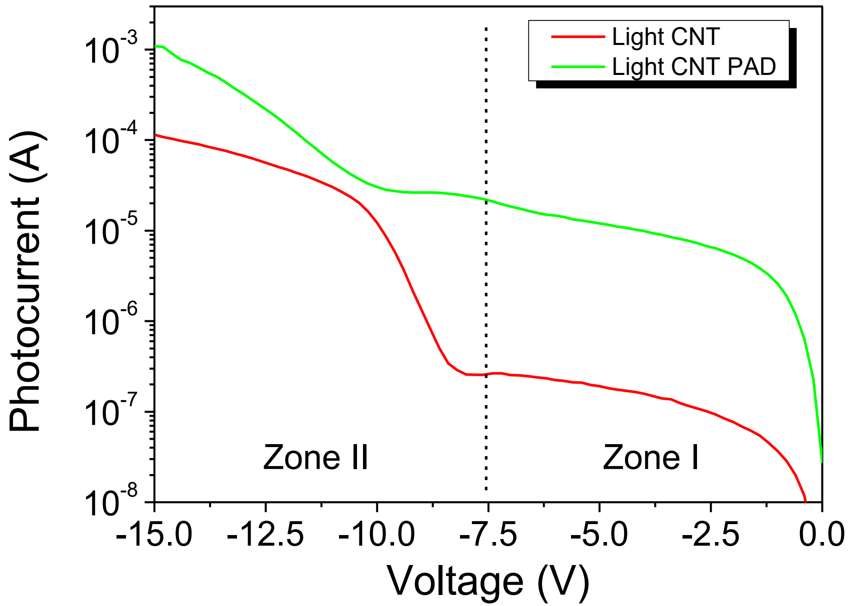

Figure 3-10 Photocurrent behaviour depending on the light spot position: on film near the pad (green curve) far from it.

The greater light power of this source allowed to measure a photocurrent also in the $(-7.5\ V, 0\ V)$ region (called Zone I in Figure 3-10) that was not observable with the LED light sources used before (due to the lower light power). We noticed that different photocurrent behaviours could be observed depending on the position of the light spot across the active surface of the film. If the light is directed above the SWCNT film close to the pad the photocurrent is greatly enhanced, especially in the Zone I where it reaches values two orders of magnitude greater than that acquired on the film alone (green curve in Figure 3-10).
This behaviour suggest that the repeated electrical stress have reduced the thickness of the nitride layer mostly below the pad, leading to the formation of the MIS diode only below this region. The rest of the SWCNT film, due to the higher thickness of the nitride layer, can be

considered instead as a MIS capacitor, that allows FN tunnelling at higher reverse bias. In this framework when the light is focused near the pad, the generation of photocharges takes place directly in the depletion layer of the MIS diode, leading to the collection of a large photocurrent also at low voltages. The photocurrent then shows a further increase due to the FN tunnelling of charges at higher reverse bias. Vice versa, when the light is directed on the MIS capacitor the photocurrent reaches higher values only in the Zone II where is observable the FN tunnelling.

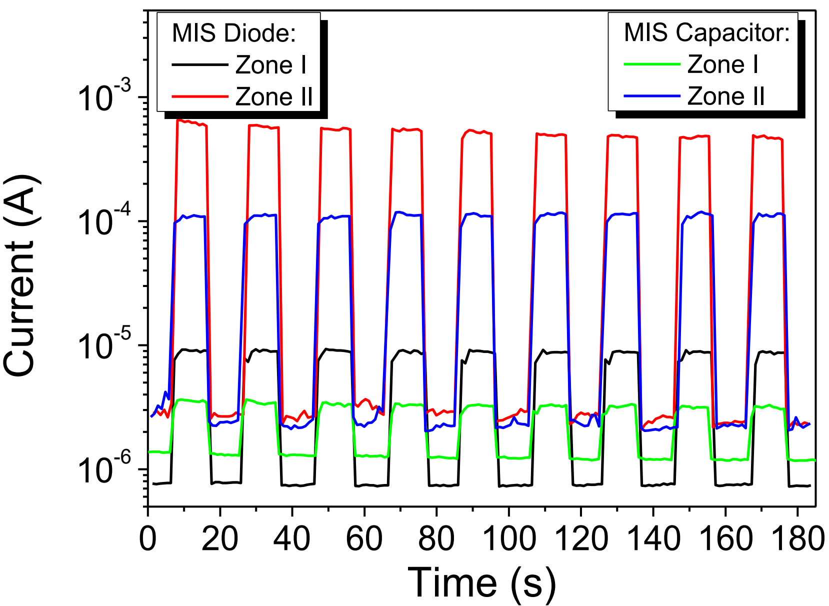

Figure 3-11 Device current under switching white light (wavelength in the range 450 nm to 2400 nm and intensity 2W/cm^2.

The time response of the device has been tested both for the MIS diode and the MIS capacitor. The measured currents reported in Figure 3-11 shows the good stability of the photoresponse for repeated on/off cycles and confirm that the photoresponse is faster than the 500 ms set by the measurement setup for the MIS diode and the MIS capacitor as well.

To check if the device could be operated in a self-powered mode, a series of measures have been acquired at zero-voltage bias and then a zero-current flow. Figure 3-12 shows that the device under illumination generates both a current and a voltage. When the MIS diode is illuminated a current of 40 nA at 0 V and 20 mV at 0 A can be measured. Since the light source operates at 8 mW cm^{-2} the MIS diode shows a photocurrent responsivity of 4.5 µA

W^{-1} and a photovoltage responsivity of 2.5 V W^{-1}. Hence the device can be operated in a self-powered mode [81–83].

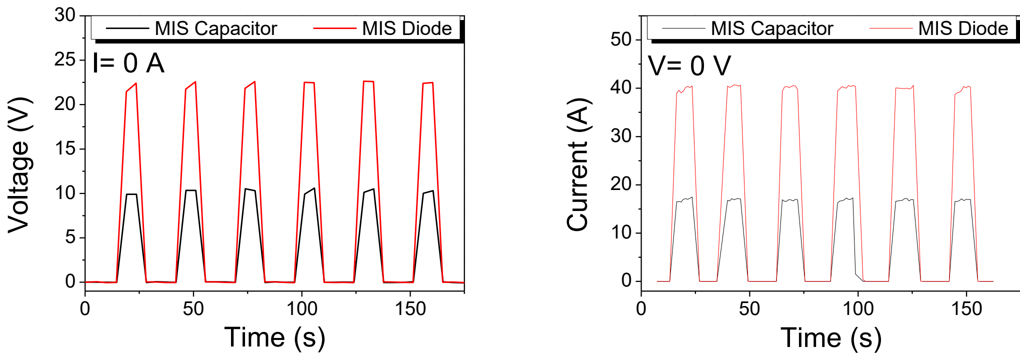

Figure 3-12 Photovoltage at 0 A and photocurrent at 0 V of the SWCNT-Si device

Furthermore, the simultaneous dependence of the photocurrent from the voltage bias and the spot position can be used for the definition of an innovative Boolean logic operator. It is possible to associate a binary variable (x) to the applied voltage (for example "0" for $-8\ V < V < -6\ V$ and "1" for $-14\ V < V < -12\ V$) and a second variable (y) to the position of the incident light spot ("0" for the light spot over the MIS capacitor and "1" for the light over the MIS diode). In this way, by considering the output equal to "1" for photocurrents in the range $10^{-5}\ A < I < 10^{-4}\ A$ and zero elsewhere, allows to consider the device as an exclusive OR (XOR).

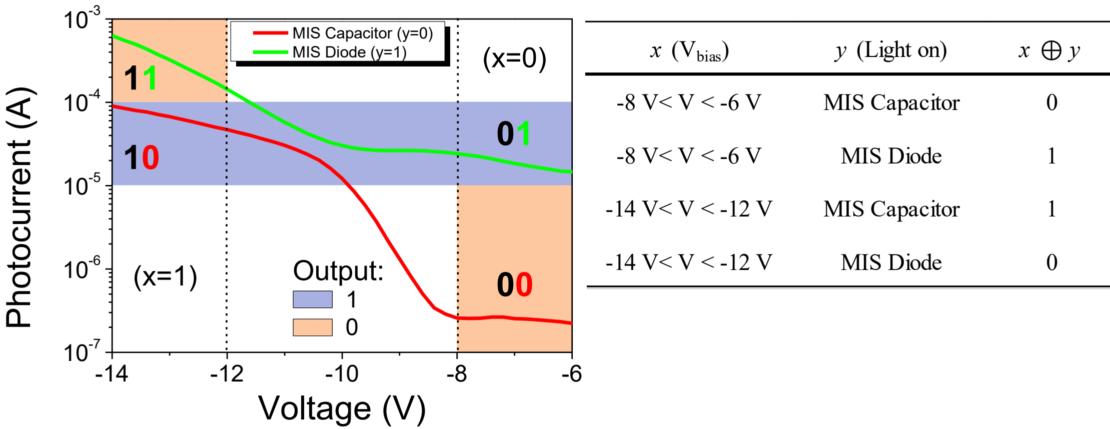

x (V_{bias})	y (Light on)	$x \oplus y$
-8 V< V < -6 V	MIS Capacitor	0
-8 V< V < -6 V	MIS Diode	1
-14 V< V < -12 V	MIS Capacitor	1
-14 V< V < -12 V	MIS Diode	0

Figure 3-13 SWCNT-Si device suitable as an optoelectronic Boolean logic operator, working as an XOR.

3.3.2 Diode parameter evaluation

To evaluate the diode parameter a series of electrical measurements were performed in a Janis 500 high vacuum cryogenic probe station connected to a semiconductor parameter analyser Keithley 4200-SCS.

To better understand the role of the nanotubes in the junction, another device was realized, in which the CNT film has been replaced by a silver film. The silver film on the substrate was obtained by depositing a layer of a silver conducting paste above the substrate. A Kapton tape mask was realized to deposit the paint in a similar shape of the SWCNT-Si device (Figure 3-14).

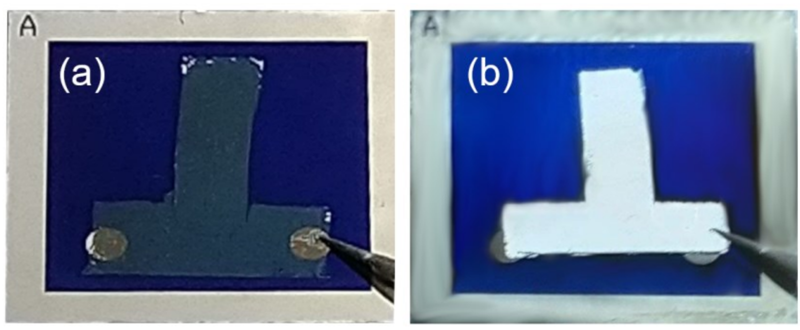

Figure 3-14 Optical images of the SWCNT-Si device (a) and the Ag-Si device(b).

The devices were then heated to the temperature of 400 K and then the first I-V curves were measured. Then the temperature was lowered with step of 20 K, acquiring new I-V curves at each step. This procedure has been repeated till a temperature of 100 K was reached.

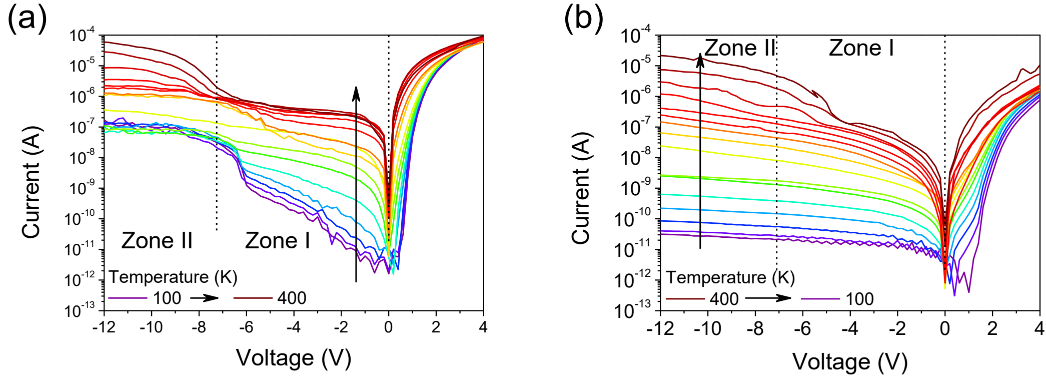

Figure 3-15 I-V characteristics at different temperatures for (a) SWCNT-Si device and (b) Ag-Si device.

The measured I-V curves are displayed in Figure 3-15(a-b). The plots show that for both the device is observable a suppression of the forward and reverse current for lower temperature.

This phenomenon agreed with the thermionic theory of MIS device. It has to be noticed that the reverse current measured in the SWCNT-Si device present a step around $V = -7\ V$ for any temperatures, that is not observed in the Ag-Si device. From the measures done in the last section we understood that this phenomenon is related to the Fowler-Nordheim tunnelling through the Si_3N_4 layer. The fact that this happens only in the SWCNT-Si device can be attributed to the peculiar shape of the nanotubes, that due to their aspect ratio, can locally enhance the electric field and allow the transition to the FN regime [84]. Is possible to observe a current saturation in the Zone II of the SWCNT-Si device, that is caused by the lump series resistance (due to the substrate), the contacts and wires which limits the currents at higher bias.

The measured currents were used to evaluate the temperature behaviour of the MIS diode parameters such as: on/off ratio, the ideality factor (n), the Schottky barrier heigh (SBH) and the series resistance (R_S).

Following the Cheung's method is possible to extract the SBH, ideality factor and series resistance from the I-V curves acquired at the different temperatures [85]. The forward current of an ideal MIS diode in the thermionic emission framework is given by:

$$I = I_0(e^{qV_D/k_BT} - 1) \quad (3.04)$$

Where V_D is the voltage applied across the diode, q the electronic charge, k_B the Boltzmann constant and T is the absolute temperature. The current I_0 can be expressed as:

$$I_0 = SA^*T^2e^{-q\phi_B/k_BT} \quad (3.05)$$

Where S is the surface of the diode, A^* is the Richardson constant and ϕ_B is the SBH of the diode.

Eq. (3.04) does not consider the presence of nonideal behaviour or resistance in series with the diode. A more generic description is given by:

$$I = I_0(e^{q(V-IR_S)/nk_BT} - 1) \approx I_0(e^{q(V-IR_S)/nk_BT}) \quad for \quad V - IR_S \gg nK_BT/q \quad (3.06)$$

Where V is the total voltage applied to the diode, IR_S is the volage drop across the series resistance an n is the ideality factor (a dimensionless number that take into accounts the nonideal behaviours. For $V - IR_S \gg nK_BT/q$ the relation in Eq. (3.06) can be rewritten in the form:

$$\frac{dV}{d(lnI)} = \frac{nk_BT}{q} + R_SI \quad (3.07)$$

Thus, a linear fit of the plot $dV/d(lnI)\ vs\ I$ can be used to determine the ideality factor (from the intercept) and the series resistance (from the slope). Once determined the value of n, the value of ϕ_B can be determined from a linear fit of the function H(I), defined as:

$$H(I) = V - \frac{nk_BT}{q}\ln\left(\frac{I}{SA^*T^2}\right) = R_SI + n\phi_B \tag{3.07}$$

In Figure 3-16 are reported the values calculated with the Cheung method and the rectification (on/off) ratio at $V = \pm 4\ V$ as a function of the temperature.

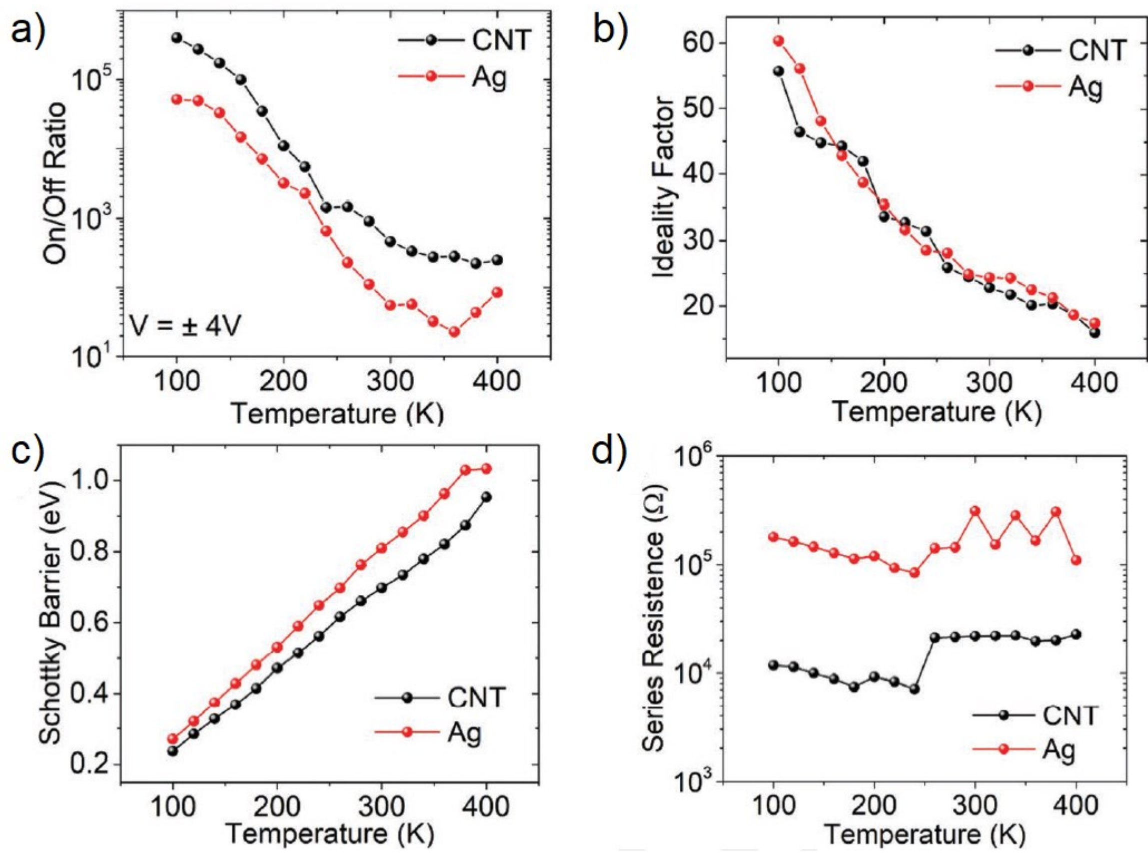

Figure 3-16 (a) On-off ratio at V=± 4 V, (b) ideality factor, (c) Schottky barrier height and (d) series resistance as a function of the temperature for the SWCNT-Si device (labelled as CNT) and Ag-Si device (labelled as Ag)

The on/off ratio in Figure 3-16(a) shows a decreasing trend with growing temperature. The higher temperatures enhance the thermal generation of carriers, which results in higher reverse currents. Figure 3-16(b) shows the behaviour of the ideality factors of the two devices, and for both higher values are reached at lower temperatures. This is reasonable because at lower temperatures the thermionic emission will be suppressed and other transport phenomena like tunnelling and diffusion will be comparatively relevant, resulting in a greater deviation from the ideal thermionic behaviour. The SBH behaviour is reported in Figure 3-16(c).

A value of 0.7 eV is measured at room temperatures, that decreases to 0.2 eV at 100K. The obtained barrier is analogous to that calculated in similar devices [86,87]. The temperature behaviour of the barrier is well-known phenomenon due to the presence of spatial barrier inhomogeneities. When the temperature drops, the reduced thermal energy allows the carrier to cross the barrier only in positions where the SBH is smaller, resulting in a reduced average SBH. Finally, in Figure 3-16(d) are reported the values of the series resistance of the devices. In both cases the resistance is constant across the explored temperature range. The better values of on/off ratio and series resistance showed by the SWCNT-Si device highlight the advantages of using carbon nanotubes over metal coating to realize electric contacts for the realization of improved photodetectors.

3.4 Conclusion

SWCNT-Si photodetector device has been developed by direct transfer of SWCNT on a silicon substrate using the dry transfer method. This simple and cheap method allows the deposition of thin nanotubes film above a substrate without the thermal stress, and expensive apparatus needed for the other approaches like the CVD growth.

Repeated electrical stresses are applied to the device until a reproducible rectifying behaviour is reached. We assumed that the electrical stress induced a reduction of the nitride layer thickness, enabling the formation of MIS junction between the SWCNT and the substrate. The device exhibits a great rectifying behaviour, with a reverse current that increases in presence of light. We demonstrate that the increase of current is due to the Fowler-Nordheim tunnelling of charges throughout the nitride layer and that the electrical stresses have reduced the nitride thickness down to 10 nm.

Using different LED sources, we observed that the photocurrent produced by the device is highly linear for all the used wavelengths and that the reached External Quantum Efficiency are competitive with other device obtained with more expensive techniques.

Using a more intense light source we saw that the photocurrent could be produced also at bias lower than the F-N threshold. Furthermore, the photocurrent could be enhanced by focusing the light near the metallic pads. This suggested that the electrical stresses thinned the nitride layer mostly below the pad, which behaves like a MIS diode, while the rest of the SWCNT film can be considered as a MIS capacitor. The enhanced current measured near the pad is explained by the photogeneration of charges directly in the depletion region of the diode, which can be collected without the higher reverse voltage needed for the FN tunnelling. The simultaneous dependence of the photocurrent on the voltage bias and on the spot position can be exploited for the realization of an opto-electronic Boolean logic operator. A possible application of the device as an XOR has been proposed.

The device parameters like on/off ratio, ideality factor, Schottky barrier height and series resistance have been evaluated as a function of the temperature. Both the on/off ratio and the ideality factor decrease with the raising temperatures, the Schottky barrier increases, and the series resistance remain almost constant. All these behaviours are consistent with the thermionic emission theory for MIS diodes. Furthermore, the lower values of series resistance and

higher on/off ratio obtained from the SWCNT-Si device respect to an Ag-Si device (realized by the deposition of conductive silver paste on the same substrate as the SWCNT-Si device) confirm that the use of carbon nanotubes is fundamental to realize improved photodetector devices.

Finally, voltage-current measures done at zero bias voltage and zero current showed that the device can be also operated in self-powered mode.

Despite the simple realization method, this device showed extremely promising features, like high linearity, high E.Q.E and the self-powered behaviour, that makes it suitable for photo-detector application. In addition, the possibility of tuning the response with the applied voltage and the position of the light allows the device to be used as an opto-electronic Boolean operator.

Chapter 4. Varying the Si_3N_4 thickness to tune the photoresponse

In the last chapter we observed that the different thicknesses of the nitride layer, obtained by the breakdown induced by electric stress, deeply affected the output of the photodetector. The differences in the nitride layer added more features to the detector, allowing the possible use as a Boolean logic operator. It follows that a better control on the nitride thickness can lead to the realization of improved and multifunctional detectors. In this chapter the nitride thickness on a silicon substrate has been modified before the CNT film deposition. We realized the devices starting from the same substrate described in the second chapter (the ones used for the CVD deposition). These were composed by a nominal 140 nm thick nitride top layer specifically designed to prevent the diffusion of the metallic catalyst into the doped silicon during the growth process. Since with the printing method the junction can be achieved without the metal catalyst, we could modify the nitride thickness without concerning of eventual modification on the silicon doping. Furthermore, the reduced thickness of the nitride layer allowed the formation of the junction (not observed in the previous chapter). The nitride layer has been thinned using hydrofluoric acid and then SWCNTs have been deposited on its surface using the transfer printing method. The properties of the nitride layer such as thickness and chemical composition has been checked before the nanotube film deposition and the electrical tests.

4.1 Device realization

The thickness of the nitride layer in these devices has been tuned using a wet etching process. The substrate has been completely covered by a Kapton tape mask to protect the metallic contacts and avoid unwanted etching, then a small window has been made on the tape to expose only a selected portion of the surface. After that, the substrate has been placed in a plastic vial containing a 5% room temperature hydrofluoric acid (HF) water solution to start the etching process. Since the different thicknesses of the nitride layer results in different interference between the light reflected from the front and back surfaces of the nitride layer,

it was possible to control the evolution of the etching process simply looking at the changes in the coloration of exposed nitride. Once reached the desired thickness the substrate has been removed from the HF and rinsed with distilled water.

For our device we choose to repeat the etching in two adjacent regions of the substrate. In this way we obtained three different thicknesses across the substrate surface: one with the “total” nitride, one with a “partial” and one with a “null” nitride left. The depth profiles across the three regions are reported in Figure 4-1. From the measures we get that the total thickness of the nitrate layer is of 120 nm and that the intermediate region has an average thickness of 70 nm.

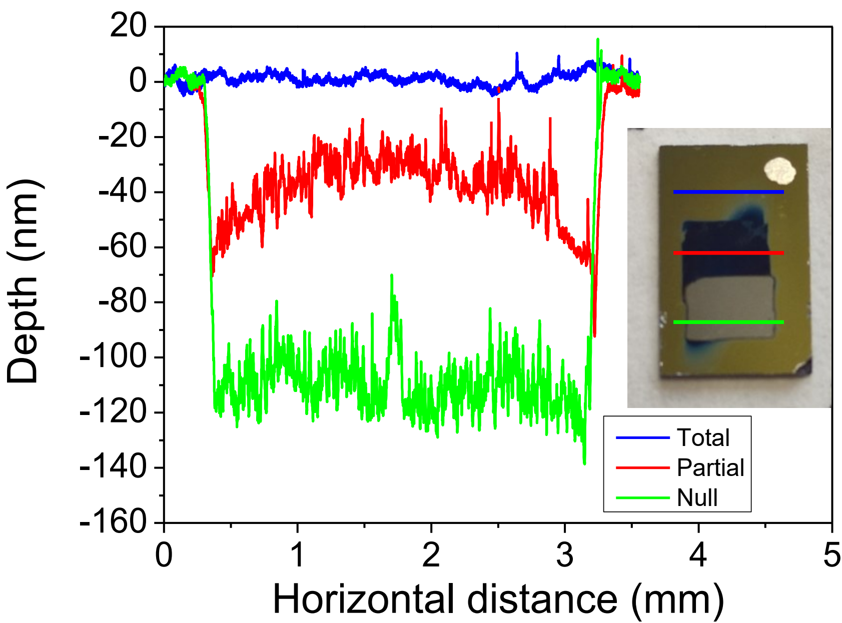

Figure 4-1 Depth profile across the lines in the three regions.

XPS spectroscopy was used to analyse the chemical composition of the surfaces, especially to confirm the complete removal of nitride in the third region. The three survey spectra are reported in Figure 4-2(a). The blue curve acquired on the full nitride region exhibits strong signal of silicon (Si), nitrogen (N) due to the substrate and carbon (C) and oxygen (O) due to atmospheric contaminants. The spectra acquired on the partial reduced region has a spectrum similar to that previously measured, with the addition of a signal coming from the fluorine (F). This signal is due to the absorption of fluorine during the etching process [88]. The last spectrum, acquire on the third region confirm that the nitride layer has been completely

removed by the etching process since the signal coming from the nitrogen is no longer observable. Figure 4-2(b) reports the deconvoluted XPS spectra of the core level Si 2p acquired on the three regions. The spectra have been fitted by the sum of three signals: the Si^0 (98.9 eV, characterized by a spin orbit splitting of 0.6 eV), the Si_3N_4 signal (101.5 eV) and the silicon oxide (102.7 eV) [89,90]. The unetched surface presents a strong signal due to the Si-N bonds, with a non-negligible signal due to silicon oxide. The partially etched region shows a spectrum like the unetched, with a reduced signal due to the oxide. The thickness of the partial region is still too high to observe the signal coming from the silicon wafer. Finally, the completely etched surface shows a strong signal at lower binding energies attributed to the pure silicon surface. A small oxide signal is presents also in this case, indicating the formation of native oxide above the silicon surfaces after the etching process.

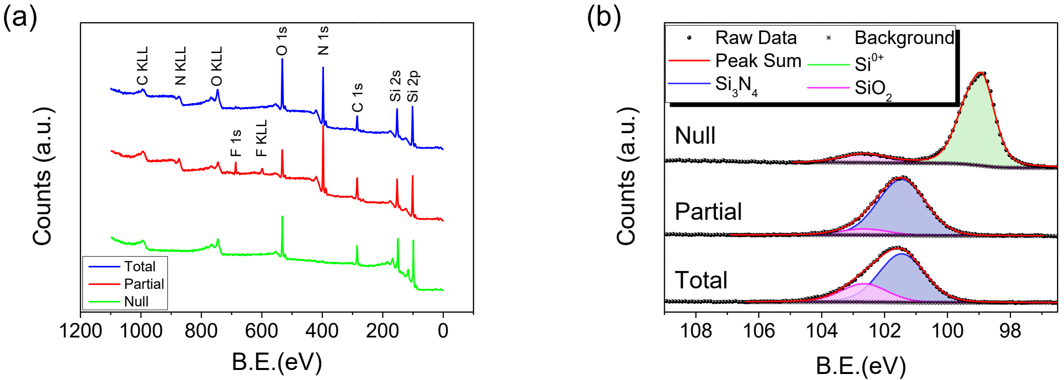

Figure 4-2 (a) XPS survey spectra acquired on the three regions of the substrate: full nitride layer (blue curve), partially and completely etched layer (respectively red and green curves). (b) Si 2p core level spectra in the three regions.

After the characterization of the substrate surface, we deposited a film of SWCNT using the wet transfer printing. The film has been deposited making contact with one of the metallic pads (to facilitate the electric contact) and covering all the three regions of the surface.

4.2 Film characterization

The morphology of the film has been analysed with a scanning electron microscope and compared with a similar film deposited with the dry transfer printing. Figure 4-3 reports the high-resolution SEM images acquired with an accelerating voltage of 5 kV on a SWCNT film deposited by the wet transfer (a) and by the dry transfer (b). The overall structure of the film is similar, the nanotubes are randomly oriented and form an intricated three-dimensional structure above the device surface. The evident difference is that the space between the nanotubes, that in the case of dry transferred nanotubes is empty, is now filled with by the residue left by the undissolved cellulose acetate filter.

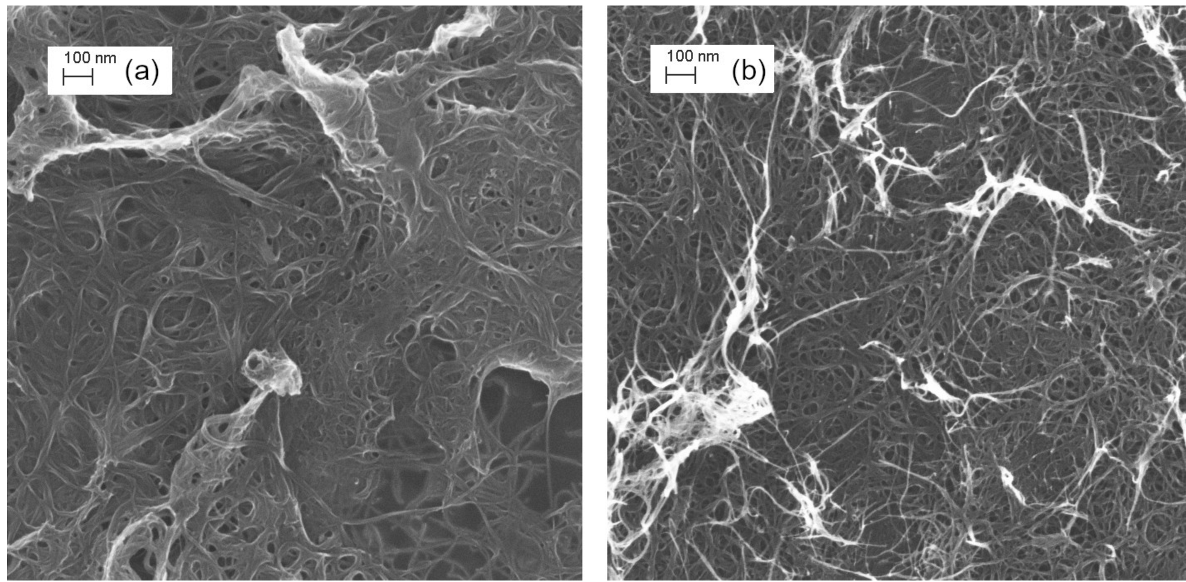

Figure 4-3 High resolution SEM images of a SWCNT film transferred with "wet" (a) and "dry" transfer printing (b)

The chemical composition of the film has been checked by X-ray photoemission spectroscopy using a Mg Kα radiation. The deconvoluted C 1s core level spectra of the two film is reported in Figure 4-4. The spectrum has been modelled by the sum of six components: aromatic rings carbon (C=C/C–C, 284.8 eV), hydroxyl groups (C–OH, 285.9 eV), epoxy groups (C–O–C, 289.6 eV), carbonyl groups (C=O, 288.2 eV), carboxyl groups (C=O(OH), 289.3) and the π-π* shake up (291.1eV). In the "wet" film, the presence of cellulose acetate residue is observable by the higher signals of oxidized carbon present in the spectrum, that in the case of "dry" transfer are much less intense.

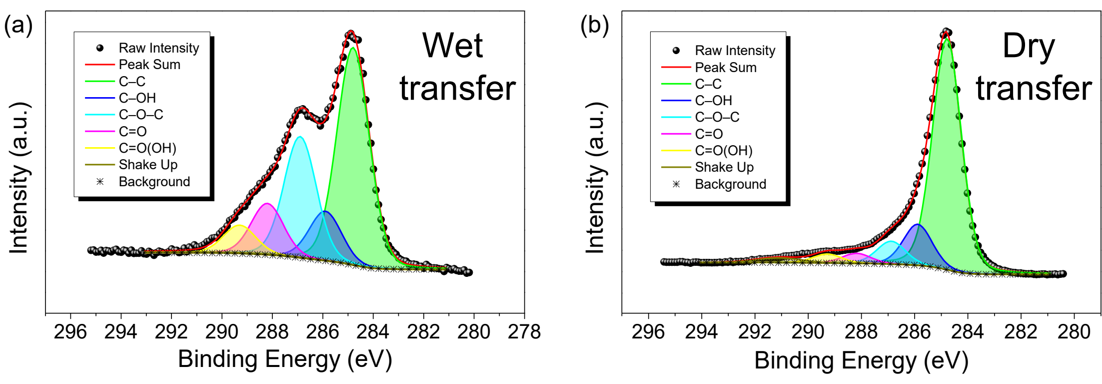

Figure 4-4 C 1s deconvoluted core level spectra of the "wet" (a) and "dry" (b) transfer SWCNT film.

The positions, full width at half maximum (FWHM) and the ratio of the areas of the individual components are reported in Table 4-I,

Peak	Position (eV)	FWHM (eV)		Area (%)	
		Wet	Dry	Wet	Dry
C–C/C=C	284.8	1.5	1.3	45.8	72.1
C–OH	285.9	1.5	1.3	10.4	12.8
C–O–C	286.9	1.5	1.3	25.5	7.1
C=O	288.2	1.5	1.3	10.8	3.1
C=O(OH)	289.3	1.5	1.3	6.0	2.8
π–π*	291.1	2.1	2.0	1.5	2.1

Table 4-I Parameters extracted from the fit of the C 1s spectra reported in Figure 4-4.

Finally, the structure of the SWCNT in the two films has been checked by Raman spectroscopy. Micro-Raman spectra were taken using a LABRAM spectrometer with a λ = 633 nm (1.96 eV) excitation line and were calibrated by the Raman peak of crystalline silicon. A comparison of the high energy modes in the Raman spectra of the two film is reported in Figure 4-5. While the G band does not display any modification, the D band presents an increased intensity in the spectrum taken on the "wet" film, that can be associated to the presence of amorphous carbon left by the cellulose acetate filter.

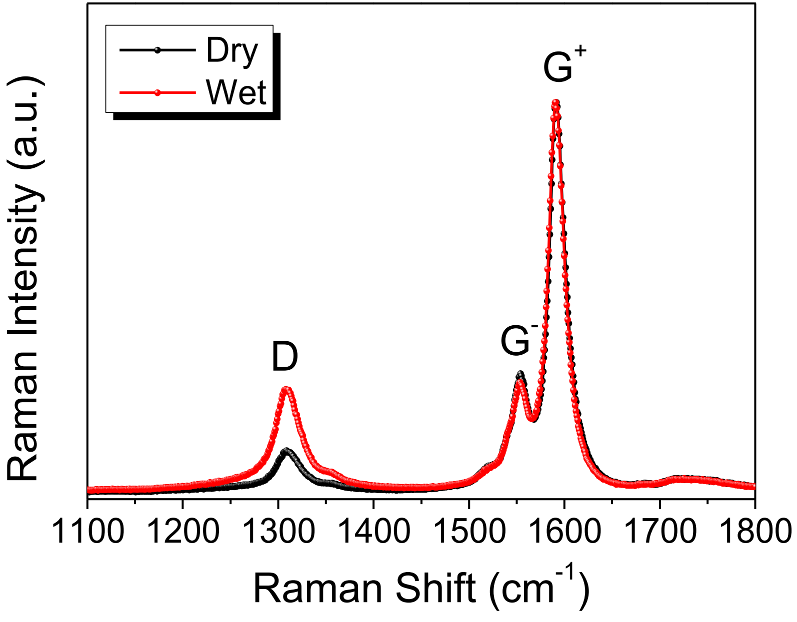

Figure 4-5 Raman high energy modes of the "wet" and "dry" film. The residues of cellulose acetate on the nanotube film contributes to an increased value of the D band.

4.3 Device characterization

The substrate before the modification was composed by a 500 µm n-type silicon wafer (resistivity 1-5 Ωcm, doping 10^{15} cm^{-1}) with the top surface covered a 140 nm Si_3N_4 layer and a metallic bottom. The top surface has been subjected to two etching cycles to obtain three regions with different nitride layer thicknesses. Figure 4-6 shows an optical image of the device after the transfer process. The three regions are easily recognizable by their colors: the full nitride layer has a yellow-green color, the partially etched is blue while the region without nitride is grey.

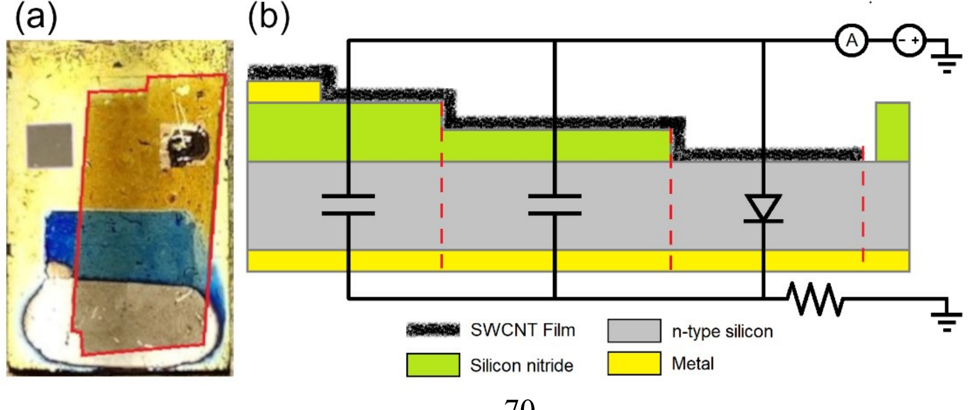

Figure 4-6 Optical image of the device. In red is highlighted the border of the SWCNT. Schematic representation of device with the different nitride thicknesses.

We measured the current-voltage characteristics of the device using the top Pt-Ta pad and the back of the substrate as anode and cathode. The electrical behaviour of the device has been tested both in dark and under a 650 nm laser light ($P = 100\ \mu W$) focused on the three nitride regions. In this device we were able to measure a reproducible current without the initial electrical stresses, fundamental step in the pevious devices. It is possible to assume that absence of the nitride layer on the third region allows the formation of a metal semiconductor junction (MS diode) between the nanotubes and the exposed silicon, that automatically allows the flow of currents through the device. Without the electrical stresses, the nitride layer below the SWCNT film does not sustain heavy damage and so it is possible to consider all the other regions of the device as MIS capacitor. The device can be modelled as the parallel of two MIS capacitor with different insulator thicknesses and a MS diode (Figure 4-6(b)). The dark I-V curve reported in Figure 4-7(a) shows that the device has a low rectifying behaviour, with an on-off ratio of only 2.3 at $V = \pm 10\ V$. The absence of the nitride layer in the third region and the large area of the SWCNT-Si junction contributes to measure a high reverse current[91,92]. Using the Cheung method, we estimated the diode parameters. Figure 4-7(b) reports the experimental $dV/d\ln(I_{dark})$ versus I (black dots) and $H(I_{dark})$ versus I (red dots) calculated at room temperature. The linear fits of these curves can be used to evaluate the values of series resistance, ideality factor and Schottky barrier height. In particular: the slope of the two curves directly determines the series resistance of the diode and, the intercept of $dV/d\ln(I)$ and $H(I)$ can be used to calculate the ideality factor and Schottky barrier height respectively. From the fits we get: a series resistance value of $R_s = 200\ k\Omega$, an ideality factor $n = 36.41$ and a Schottky barrier $\phi_b = 0.69\ eV$.

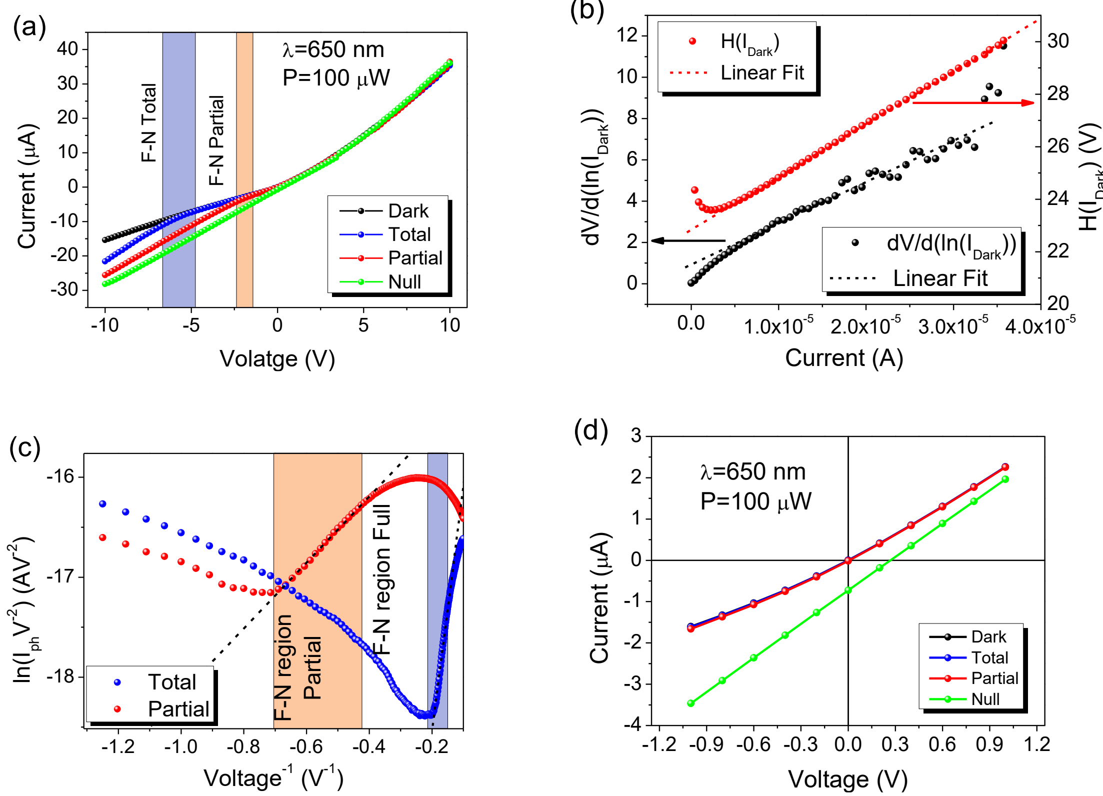

Figure 4-7 (a) I-V characteristic of the device in dark and under illumination with the spot focused of the different regions of the device: "total", "partial" and "null" nitride thickness. (b) Experimental values of $dV/d\ ln\ (I_{dark})$ (black dots) and $H(I_{dark})$ as a function of the dark current (I_{dark}) (red dots). The dashed lines represent the linear fit of the data. (c) Fowler-Nordheim plot of the photocurrents measured for the total and partial MIS capacitor. The dashed highlight the linear behaviour in the F-N region. (d) Detail of the currents around 0 V that shows the production of an open circuit voltage of near 300 mV and a short circuit current of 0.7 μA.

Despite the poor quality of the SWCNT-Si diode, the photoresponse of the device is very interesting. From Figure 4-7(a) is possible to see that the device exhibits different behaviours depending on the position of the spot across its surface. When the spot is located above the complete nitride layer (blue curve) the current under illumination does not change much from the dark one until a voltage $V = -5\ V$ is reached. Then, if the light spot is moved on the partially etched region the starting voltage of the photocurrent gets closer to zero. The linear behaviour of the photocurrent in the Fowler-Nordheim plot in Figure 4-7(c) demonstrate that the photocurrent is due to charges tunnelling through the triangular barrier in the MIS capacitors. The F-N plot also highlight that the charges begin to tunnel through the nitride layer at different bias, depending on the insulator thickness. We observe a turn-on voltage of $V^{Turn-on} = -1.5\ V$ for the "partial" capacitor and $V^{Turn-on} = -5\ V$ for the "total" capacitor. Finally, the device shows photovoltaic properties when the light is focused above the MS diode. The I-V curve in Figure 4-7(d) shows that a 650 nm laser light at 100 μW focused on

the MS diode produces an open-circuit voltage $V_{oc} = V(I = 0) = 0.27\ V$ and a short-circuit current $I_{sc} = I(V = 0) = 0.72\ \mu A$. The corresponding current and voltage responsivity are 720 μA W^{-1} and 27 V W^{-1}.

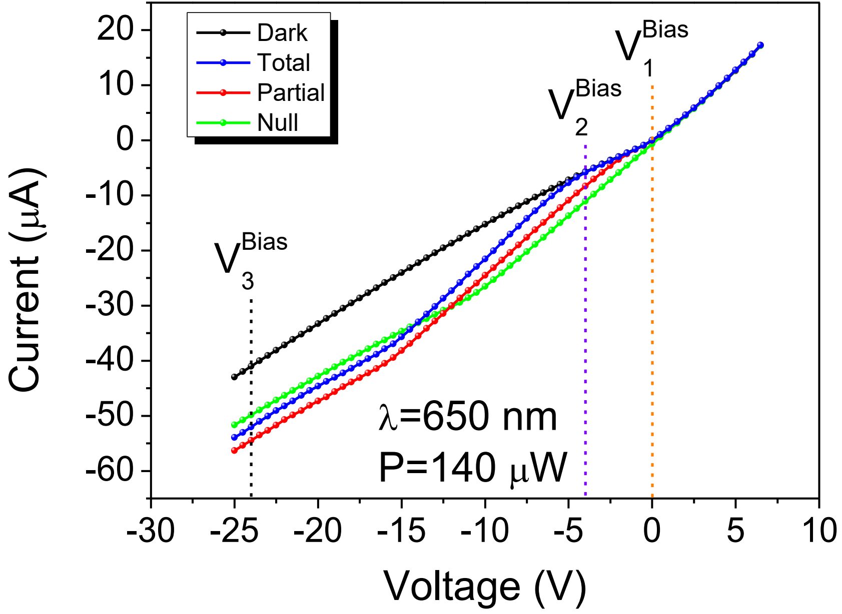

Figure 4-8 Detail of the currents in a wider voltage range. In the pictures are highlighted the biases used for the linear characterization of the device.

To have a better insight on the current behaviour in presence of light we acquired more I-V characteristics using a larger voltage sweep. Figure 4-8 highlights the presence of a plateau in the photocurrent that was not observable in Figure 4-7(a). The light impinging on the substrate generates electron-hole couples inside the silicon, that get separated by the electric field and move toward the contacts. If the photocharges are generated inside a MIS capacitor, then the photocurrent does not change much from the dark one until the turn-on voltage for the tunnelling is reached. With the increasing reverse bias, more charges can reach the contacts without recombination, resulting in a linear increase of the current. Eventually an equilibrium between generation of charges and collection is achieved and the photocurrent reaches a plateau. When the light is directed on the MS diode instead the charges are separated by the built-in potential so there is no need to reach a turn-on voltage to see a photocurrent. Then the current grows with the reverse bias till a plateau is reached.

We deeply investigate the response of the device to different incident light powers to understand its behaviour and the presence of limits towards future applications. The complete I-V

characteristics were collected with the light of a 650 nm laser focused on the different regions of the device. Then the photocurrents ($I_{photo}(V) = I_{light}(V) - I_{dark}(V)$) produced by the different impinging power were then calculated at the three biases reported in Figure 4-8 to highlight the presence of linear behaviours in different working condition. The first bias has been set at $V_1^{Bias} = 0\ V$ to better characterize the photovoltaic mode of the device. The second bias at $V_2^{Bias} = -\ 4\ V$ has been chosen to highlight the response of the device in a region where only the MS diode and the partial MIS capacitor are active. The third bias has been set at $V_2^{Bias} = -\ 24\ V$ to characterize the response of the device in the plateau region. Figure 4-9 shows the values of photocurrent calculated at different bias as a function of the impinging light power for the three regions of the device. To highlight the presence of small photocurrents we reported the values in two graphs, one for currents in the order of microampere and one for that in the nanoampere. When the light is focused on the unetched nitride layer (Figure 4-9(a)), the photocurrents reach values in the order of microampere only when strong reverse bias is applied to the device while with lower voltages the photocurrents remain in the order of nanoampere. The photocurrents measured at high reverse bias and that with no external bias show linearity for all the impinging power used, while with the low reverse bias the behaviour is not well defined. When the light is focused on the partially etched nitride (Figure 4-9(b)) the photocurrent at low reverse bias is enhanced. Now is possible to observe a microampere current flowing through the device, but there is still no complete linearity: at lower powers, the photocurrent values follow a trend that is comparable to that of the plateau region, but with higher powers a saturation occurs. In the cases of high reverse bias and with no external bias the values of photocurrents follow a linear behaviour for all the impinging powers. Finally, when the light is focused on the MS diode the full linear behaviour is conserved only when the current is measured at the plateau, while bot in the other cases the photocurrents have an initial linear behaviour that then ends in saturation.

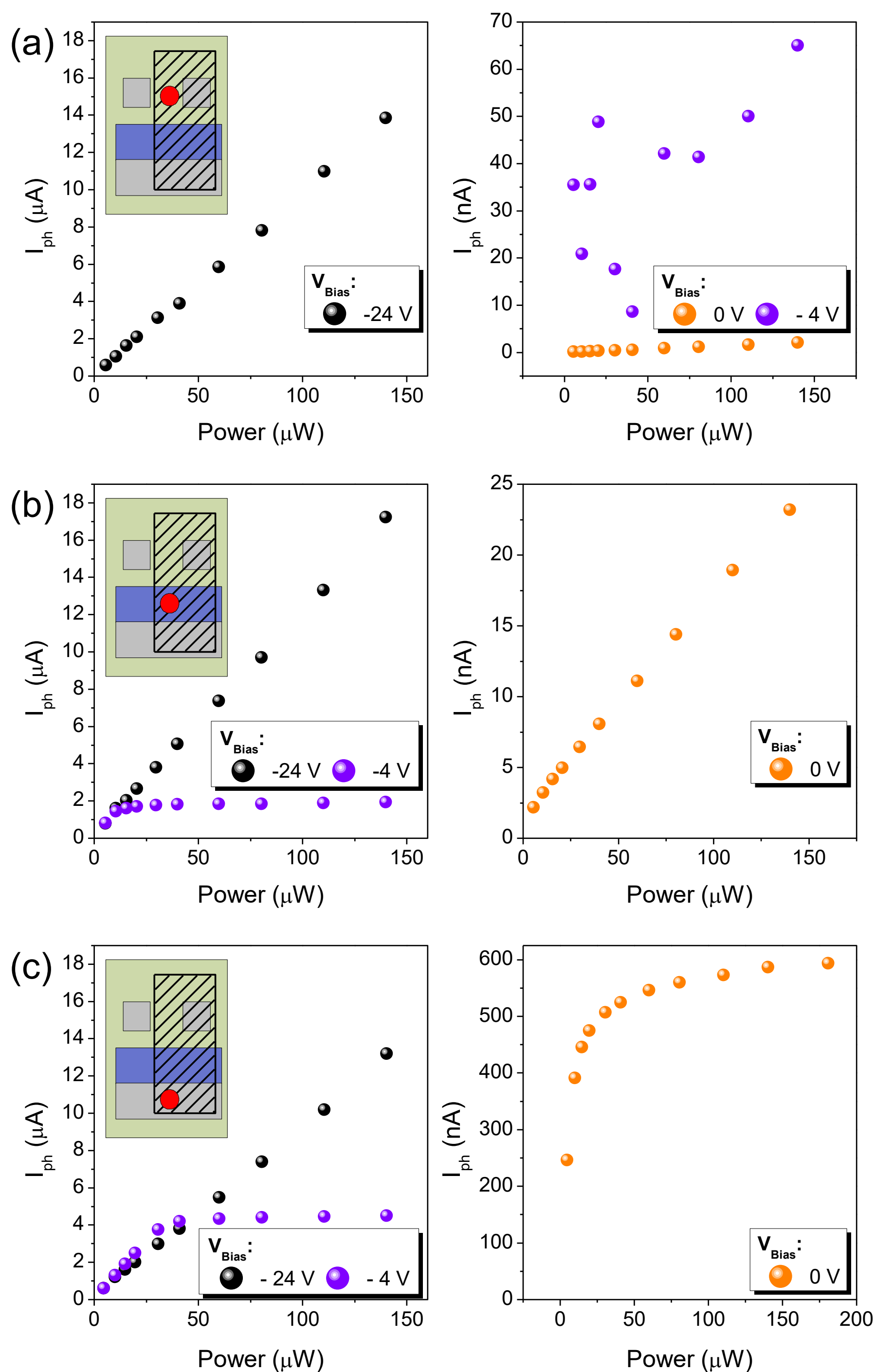

Figure 4-9 Values of the photocurrent calculated at different bias for (a)MIS capacitor with total nitride layer, (b) MIS capacitor with partially etched and (c)MS diode.

When the structures show a linear behaviour, the average responsivity can be evaluated from the slope of the linear fit of all the data. In presence of saturation, since the photocurrent does not grow anymore with the impinging light power, the responsivity will show a decreasing

trend with the increasing power. In these cases, the maximum value of responsivity can be evaluated from a linear fit restricted to the region before the saturation. To have an idea of the performance of the different structures we reported the responsivity values (and the associated error obtained from the fit) inside Table 4-II.

Spot Position	Responsivity (A/W)		
	V = 0 V	V = - 4 V	V = -24 V
MIS Capacitor (Total)	$(1.48 \pm 0.03)\ 10^{-5}$	$(24.1 \pm 9.9)\ 10^{-5}$	$(9.9 \pm 0.1)\ 10^{-2}$
MIS Capacitor (Partial)	$(15.6 \pm 0.1)\ 10^{-5}$	$(7.8 \pm 2.4)\ 10^{-2}$	$(12.1 \pm 0.1)\ 10^{-2}$
MS Diode	$(1.5 \pm 0.3)\ 10^{-2}$	$(12.1 \pm 0.2)\ 10^{-2}$	$(9.1 \pm 0.1)\ 10^{-2}$

Table 4-II Responsivity of the device regions at the different bias.

Several information can be extracted from this table. First, the responsivity of the device in the photovoltaic mode ($V = 0$) strongly depends on the thickness of the nitride layer. The values obtained from the diode, where no nitride layer is present, are two orders of magnitude greater than that obtained from the capacitor with the partially reduced nitride layer, which in turn is one order of magnitude greater than that with the total nitride. This is coherent with the description made until now. The insulating layer put a barrier that prevents the transport of carries through the junction, but when this is removed the carriers can cross the junction and contribute to an appreciable current. An important feature is that the structures can be activated by simply changing the applied voltages. For example, by setting the voltage to $-24\ V$ is possible to have a response from all the structures (with a similar response), but by lowering the reverse bias to $-4\ V$, the response of the capacitor with the thicker nitride layer will be completely suppressed.

To highlight this behaviour, we acquired several photocurrent maps of the device using the scanning photocurrent imaging. To help the description of the maps, Figure 4-10(a) report an in-scale reproduction of the device shown in Figure 4-6(a). The map acquired at $V = -18\ V$ (i.e., in the plateau region of the currents) shows that all the nanotube film is responding to the incoming light, while the rest of the device does not respond. The region below the pad is not responding since the metal layer reflects completely the radiation and then no photo-charges can be generated inside the silicon substrate. A slightly higher photocurrent can be measured in the partially etched region respect to the unetched one, where the higher nitride

thickness reduces the numbers of photon that can reach the silicon and generate photo-charges. At this voltage, the presence of the nitride layer positively affects the device response, as a fact the photocurrent measured on the MIS capacitor is always greater than that on the MS diode. Indeed, other works confirms that the presence of an insulating layer at the interface of a CNT-Si heterostructure is able to improve the performance of the device since it switches the charge transport from pure thermionic emission to a mixture of thermionic emission and tunnelling, improving the diode properties [93–99].

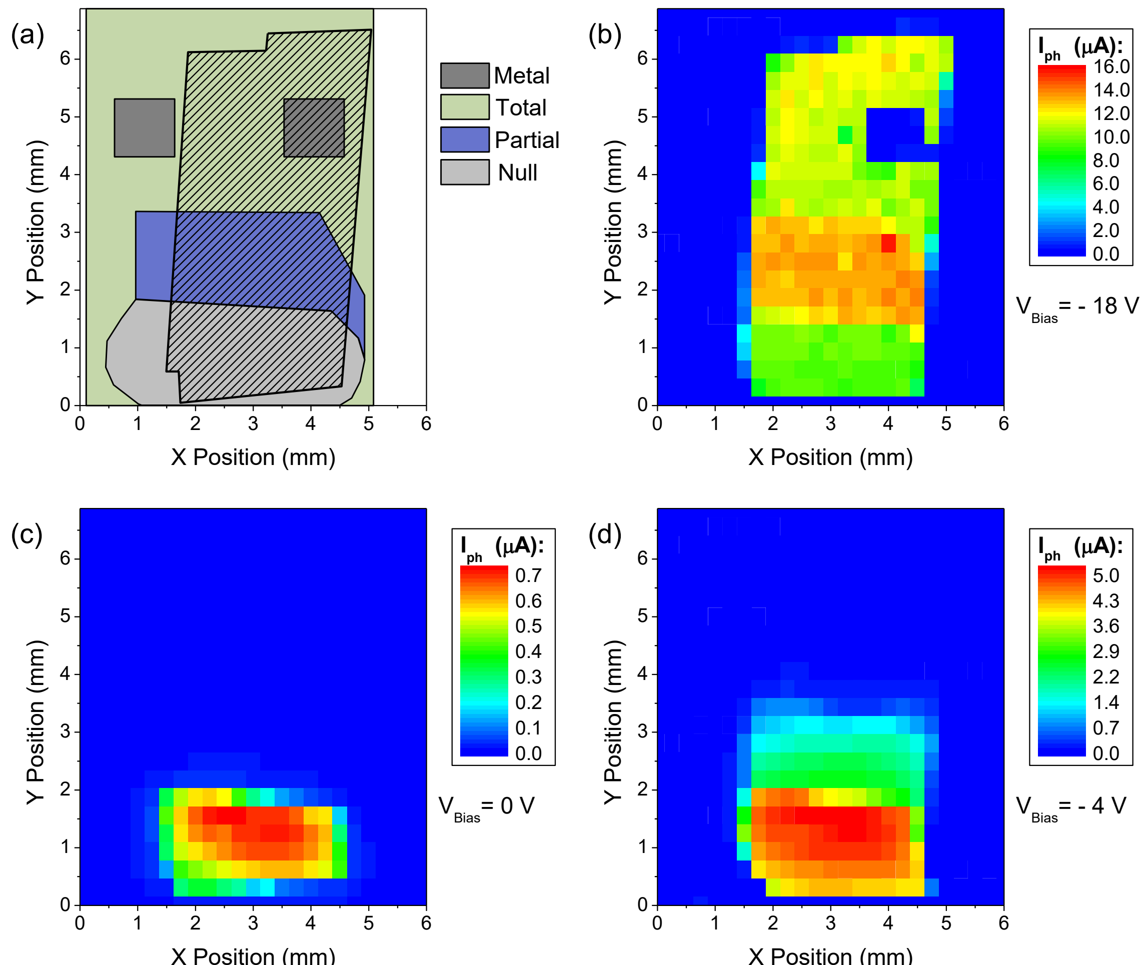

Figure 4-10 (a) In-scale schematic top view of the device. Extracted photocurrent maps at -18 V (b), 0 V (c) and -4 V (d).

By simply varying the voltage bias the response of the device can be tuned accordingly to the thickness distribution of the nitride layer. When no biases are applied to the device only the MS diode region is active, and the device only work in photovoltaic mode. When the reverse bias is increased to $-\ 4\ V$, that is a voltage slightly higher than the turn-on voltage of

the "Partial" MIS capacitor and less than that of the "Total" MIS capacitor, the Partial MIS capacitor start to respond.

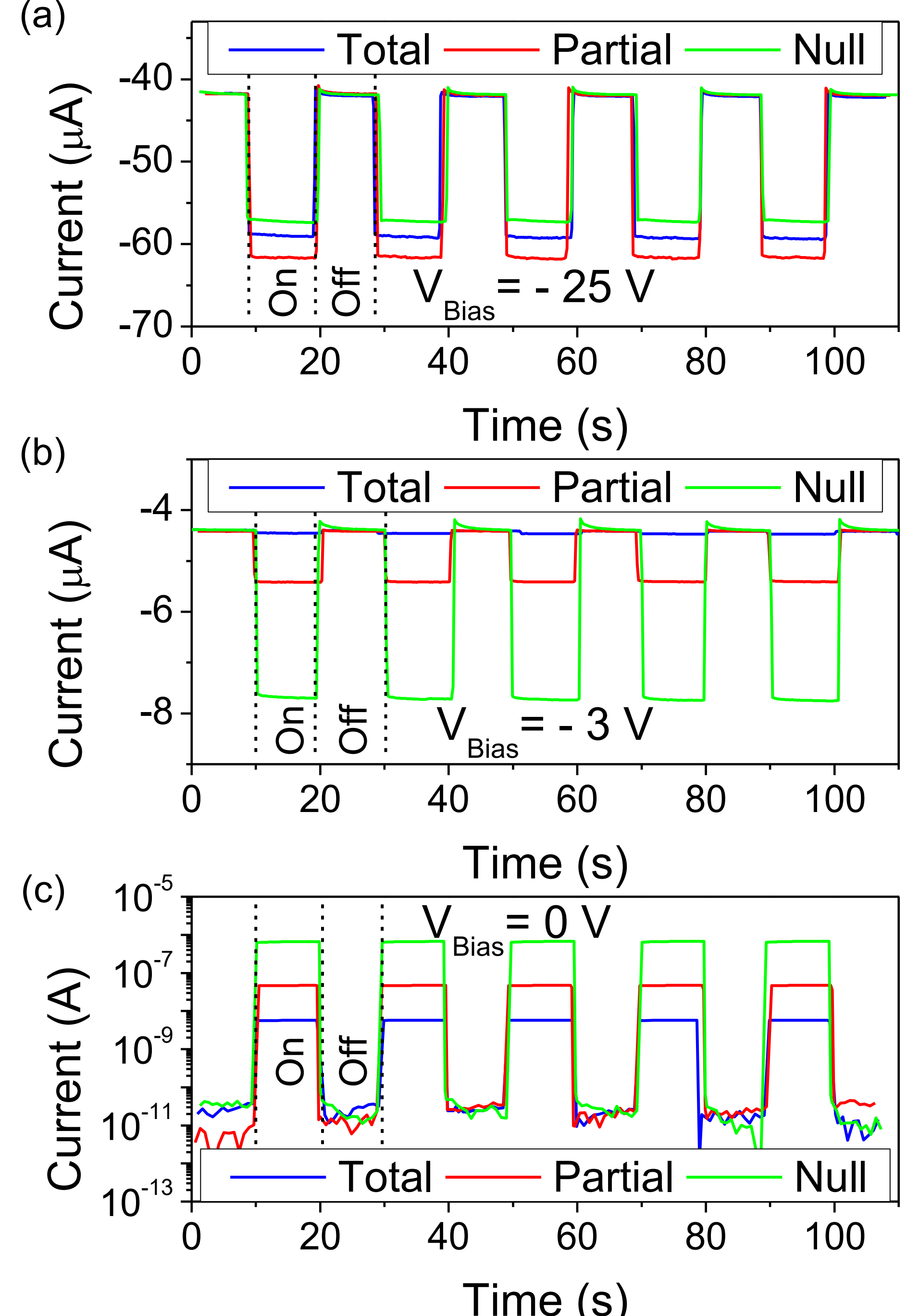

Figure 4-11 time response of the device in the plateau region (a), at an intermediate voltage (b) and at zero voltage(c). The last graph is reported in semi-log scale to highlight the different orders of magnitude of the photoresponse.

The time response of the device has been tested with repeated on/off cycles of a 650 nm laser light at 200 μW power. The response acquired for all the regions at different bias is reported

in Figure 4-11. In all the cases the time response is faster than the $500\ ms$ limit set by the experimental setup and stable for all the observed time. Figure 4-11(c) shows the current modulus in a semi-log scale of the currents acquired at $0\ V$. In this way is possible to emphasize the various orders of magnitude of the currents produced in the photovoltaic mode.
To conclude the analysis on this device we tested the response of the different regions as a function of the wavelength of the incoming radiation. We measured the photocurrent produced by the device under different lights and calculate the associated external quantum efficiency. Figure 4-12 displays the efficiency calculated at zero bias (photovoltaic mode) and at plateau of the photocurrent (photoconduction mode). In the photovoltaic mode the efficiency in the MS diode is two to three orders of magnitude greater respect to the other regions for all the wavelengths. In the photoconductive mode all the efficiency are of the same magnitude, whit the MIS capacitors slightly more efficient than the MS diode

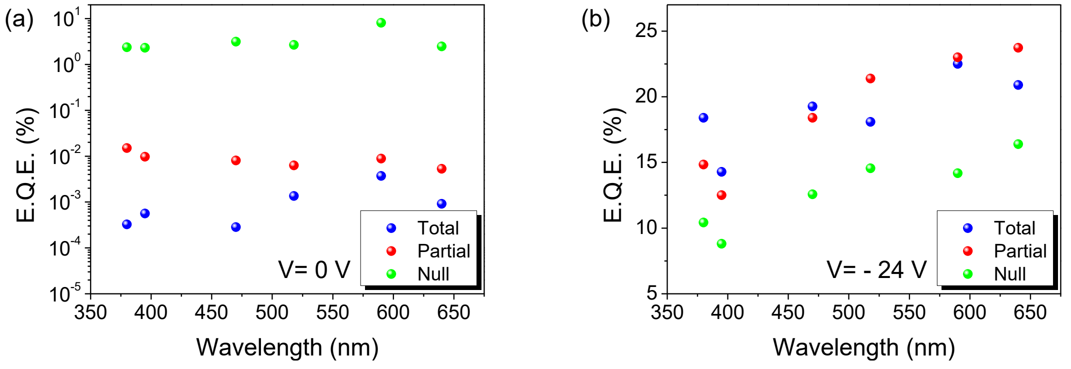

Figure 4-12 External Quantum efficiency calculated at zero bias (a) and at the plateau of the photocurrent (b).

4.4 Conclusions

We have fabricated and studied a photodetector obtained from the heterojunction between SWCNT and a silicon substrate. The substrate, initially composed by a n-doped silicon wafer with the top surface covered by a thick nitride layer (nominally 140 nm), has been modified by repeated wet etching cycles to reduce the thickness or remove the nitride layer across its surface. Three zone has been made on the device: one with the total nitride thickness (called "Total"), one with a partial thickness (called "Partial") and one without nitride (called "Null"). The XPS spectra acquire in the "Null" region confirmed the absence of silicon nitride above the substrate and the profilometer measurement allowed us to determine the effective thickness of the nitride in the Total and Partial region (120 nm and 70 nm respectively). After the etching treatment, a SWCNT film has been deposited on the substrate using the wet transfer process. Both the morphological and chemical analysis of the film highlights the presence of cellulose acetate residue on the film.

The device then has been electrically characterized in the top-back configuration, using one of the top pads and the metallic back of the device as contacts. The I-V characteristics, acquired without electrical stresses showed a low rectification, with a huge deviation from the ideal behaviour, due mostly to the large contact area of the junction with the exposed silicon. The absence of electrical stresses allows to consider the nitride layers undamaged. It is possible to consider all the device composed by the parallel of two MIS capacitor (one with the total and one with the partial nitride thickness) and a MS diode (formed in the Null region of the substrate). Despite its low performances as rectifying junction, the device is still interesting due to its peculiar response to the incoming light. Depending on the position of the spot across its surface, the photocurrent exhibits completely different behaviours. When the light is focused on the MIS capacitors, the reverse current does not vary from the dark one until a certain voltage is reached, where, as confirmed by the Fowler-Nordheim plot, the photocharges start to tunnel through the insulating layer. When the light is focused on the MS diode instead the device shown a photovoltaic behaviour, with a $V_{oc} = V(I = 0) = 0.27\ V$ and a short-circuit current $I_{sc} = I(V = 0) = 0.72\ \mu A$, that correspond to a current and voltage responsivity of $720\ \mu A\ W^{-1}$ and $27\ V\ W^{-1}$ respectively. The responsivity of the device has been checked at different voltages to verify the presence of linear behaviours of the

photocurrent. It has been found that at high reverse bias, where all the currents reach the plateaux, the behaviour is linear, with small differences between the device regions, but when the bias is lowered, the response of the regions with higher nitride thickness becomes negligible. To highlight this behaviour a series of photocurrent map has been acquired: one at high reverse bias, that demonstrate that the active surface of the device is delimited by the nanotube film, independently on the nature of the substrate; one with no bias, where the response comes only from the MS diode; and one at an intermediate voltage, where the contribution comes from the MS diode and the MIS capacitor with the lower thickness. The time response has also been checked by a series of on/off cycles under a laser light. In every case, the time response time is lower than the limit imposed by the experimental apparatus.

Finally, the external quantum efficiency of the device has been tested as a function of the incoming light wavelength, both in the high voltage regime and with no external bias. With no external bias, an appreciable E.Q.E. is obtained only in the MS diode, whereas, in the other regions although is still present a response, is from two to three orders of magnitude smaller. In the high reverse bias instead, the efficiency is similar for all the three regions. Furthermore, the efficiency does not present trends as a function of the wavelengths.

Chapter 5. Conclusion

I've focused the work of this thesis on the realization and characterization of devices based on carbon nanotubes-silicon heterojunction for photodetection application.

The first part of this work has been devoted to the characterization of devices obtained through the direct growth of carbon nanotubes above a silicon substrate. The nanotubes have been grown using the chemical vapor deposition method, with nickel (Ni) as metallic catalyst and acetylene as carbon precursor. The nanotube film has been characterized by means of scanning electron microscopy (SEM) to get morphological information, x-ray photoemission spectroscopy (XPS) for the chemical composition and Raman spectroscopy for the structural analysis. Then the device, has been connected to a Keithley 236 source-measure unit for the electrical characterization. After a series of electrical stress, the I-V characteristic of the vertical MWCNT-Si_3N_4-Si heterostructure has been acquired in dark and under illumination. The curves in presence of light shown a sudden increase in the reverse bias one a certain voltage is reached. The behaviour of the photocurrent in the Fowler-Nordheim plot allowed to demonstrate that this increase of current is due to the tunnelling of charges through the nitride layer. The efficiency maps acquired on the first device exhibit some inhomogeneities of the produced photocurrents across the device surface. The photocurrent resulted enhanced in region of the device where the nanotube film was thinner. For this reason, I have developed a simple and inexpensive procedure to reduce the thickness of an already grown CNT film. The efficiency maps acquire on a device before and after the reduction process highlight the increase of the photocurrents in the reduced portion of the film. The I-V curves acquired in the two regions showed that the photocurrent in the reduced film grows with a smaller rate compared to the unreduced. This led to the formation of two regimes of photocurrent depending on the applied bias. At lower reverse bias the greater number of nanotubes in the unreduced film allows a better collection and transport of the photocharges, resulting in a greater efficiency. Vice versa, at higher voltages, where the collection-extraction process has reached a saturation, the reduced film has a better response since the lower thickness of the film allows more photons to reach the substrate and generate photocharges. The reduction process has also been tested to find its limits. I saw that a second iteration can be enough to completely remove the nanotube film and therefore cut off the device response in that area.

From these first analysis I understood that one of the main parameters that must be considered in the realization of a CNT-Si device is the thickness of the film. Despite the reduction process offers a simple way to reduce the film thickness, and consequently improve the overall efficiency, it has different drawbacks that limits its application.
To overcome these problems, in the second part of this work I have realized new devices using a different approach. In this case the nanotubes have been deposited on the substrate using the transfer printing method. In this method the nanotubes are initially dispersed in a water solution and then deposited on a filter membrane by low vacuum filtration. After the filtration, the nanotube film can be transferred directly on the substrate. The attractive feature of this method is that the thickness of the film can be tuned by simply varying the aliquot of filtered solution. Once deposited, the film has been characterized by SEM, XPS and Raman to get a full understanding of the morphology, chemical composition, and structure of the nanotubes after the deposition. Then, the device has been connected to the measure apparatus for the electrical characterization. A series of electrical stresses have been applied to the vertical heterostructure to get a reproducible behaviour of the current. After that, the device showed a high rectification behaviour, due to the formation of a MIS junction between the nanotubes, the silicon nitride, and the n-doped silicon substrate. In presence of light the device starts to produce a high photocurrent once the reverse bias reaches a certain voltage. As in the second chapter, the Fowler-Nordheim plot demonstrate that the photocurrent is due the tunnelling of charges through the nitride layer. The device showed a good linear behaviour and efficiency comparable to devices obtained with more expensive approaches. Further measures done with a higher light power showed that a photocurrent can be observed also at biases lower than the F-N threshold. Furthermore, this photocurrent is greatly enhanced when the light is focused near the metallic pad. This behaviour suggested that the thinning of the nitride layer occurs mostly below the metallic pads, leading to the formation of the MIS diode in that region, while the remaining nanotube film, due to the higher thickness of the nitride layer can be modelled as a MIS capacitor. The simultaneous dependence of the photocurrent from the bias and the spot position can be exploited for the realization of intriguing optoelectronic device such as logic Boolean operators. A possible implementation of the device as an excluding OR (XOR) has been proposed. In the last section of this chapter, the behaviour of the diode parameters such as on/off ratio, ideality factor n, Schottky barrier ϕ_B and series

resistance R_s of the SWCNT-Si device have been evaluated in comparison with an Ag-Si device obtained by the deposition of silver conductive paste above a silicon substrate. The resulting value are consistent with the thermionic emission theory from a MIS junction. The better performance of the SWCNT-Si diode respect to the Ag-Si diode further support the use of these nanostructured materials as semi-transparent metallic contacts. A noticeable remark from this section is that the presence of inhomogeneities inside the nitride layer can led to the realization of intriguing new devices, exploiting the different response of the MIS diode over the MIS capacitor.

For these reasons in the last chapter of this work I have analysed a SWCNT-Si device obtained from the deposition of SWCNT above a silicon substrate in which the nitride layer has been opportunely modified. Starting from a substrate with all the top surface covered by a thick nitride layer, I have varied the thickness of the nitride with repeated wet etching cycles to obtain regions with different nitride thicknesses. The substrate used in this section were modified to obtain an unetched region, a partially etched region, and a fully etched region, with respectively the "total", "partial" and "null" nitride thickness above the same substrate. The XPS analysis in the "null" region confirmed the total remotion on silicon nitride from the surface. After the deposition of the nanotubes, the electrical response of the device has been characterized. Due to the direct formation of the junction between the nanotubes and the n-doped silicon, it was possible to obtain reproducible I-V curves without the electrical stresses needed in the previous section. This detail allows to consider that no damages have been made on the unetched and the partially etched nitride layer. This allows to consider these two regions as MIS capacitors while the completely etched region as a MS diode. The I-V curves measured in dark does not show great values of on/off ratio or ideality factor, but an intriguing response is observed when the device is exposed to light. Depending on the position of the light spot across the substrate, a different type of response can be obtained. As in the previous section, in the MIS capacitors the photocurrent became appreciable only when the turn-on voltage of the Fowler-Nordheim tunnelling is reached. But since in this device the two capacitors have a different insulating layer, the turn-on voltage is different for the two regions. In the MS diode instead, the absence of the insulating layer allows the device to exhibit enhanced photovoltaic behaviours. These different performances allow to observe photocurrents which intensities depend on the spot position and the applied bias. The

responsivity of the three regions have been calculated at different bias to understand if the responses possessed linear behaviours. After that a series of photocurrent maps were acquire on the device at different bias. These maps highlight the possibility to select the active area of the device by simply varying the applied voltage.
The work that I have done in my thesis offers low cost and scalable ways to realize devices with more features than a simple photodetector, due to the simultaneous dependence of the response to the incoming light and the applied bias.

List of publications

1. Photoresponse Study of MWCNTS/Insulator/n-Type Si/Insulator/Metal Heterostructure as a Function of the Density of MWCNTs Layer.
   Capista, D.; Passacantando, M.
   Mater. Proc. **2020**, *4*, 60, doi:10.3390/IOCN2020-07936.

2. Easy Fabrication of Performant SWCNT-Si Photodetector.
   Capista, D.; Passacantando, M.; Lozzi, L.; Faella, E.; Giubileo, F.; Di Bartolomeo, A.
   Electronics **2022**, *11*, doi:10.3390/electronics11020271.

3. Bias tunable photocurrent in metal-insulator-semiconductor heterostructures with photoresponse enhanced by carbon nanotubes.
   Di Bartolomeo, A.; Giubileo, F.; Grillo, A.; Luongo, G.; Iemmo, L.; Urban, F.; Lozzi, L.; Capista, D.; Nardone, M.; Passacantando, M.
   Nanomaterials **2019**, *9*, doi:10.3390/nano9111598.

4. Synthesis of hydrophilic carbon nanotube sponge via post-growth thermal treatment.
   Camilli, L.; Capista, D.; Eramo, P.; D'Archivio, A.A.; Maggi, M.A.; Lazzarini, A.; Crucianelli, M.; Passacantando, M.
   Nanotechnology **2022**, *33*, 245707, doi:10.1088/1361-6528/ac5bb7.

5. Field emission from two-dimensional GeAs.
   Di Bartolomeo, A.; Grillo, A.; Giubileo, F.; Camilli, L.; Sun, J.; Capista, D.; Passacantando, M.
   J. Phys. D. Appl. Phys. **2021**, *54*, 105302, doi:10.1088/1361-6463/abcc91.

6. Germanium arsenide nanosheets applied as two-dimensional field emitters.
   Giubileo, F.; Grillo, A.; Pelella, A.; Faella, E.; Camilli, L.; Sun, J.B.; Capista, D.; Passacantando, M.; Di Bartolomeo, A.
   In Proceedings of the Journal of Physics: Conference Series; IOP Publishing, **2021**; Vol. 2047, p. 12021.

7. Formation of a two-dimensional oxide via oxidation of a layered material.
   Camilli, L.; Capista, D.; Tomellini, M.; Sun, J.; Zeller, P.; Amati, M.; Gregoratti, L.; Lozzi, L.; Passacantando, M.
   Phys. Chem. Chem. Phys. **2022**.

8. Hybrid Polyphenolic Network/SPIONs Aggregates with Potential Synergistic Effects in MRI Applications.

Lazzarini, A.; Colaiezzi, R.; Galante, A.; Passacantando, M.; Capista, D.; Ferella, F.; Alecci, M.; Crucianelli, M.
Results Chem. **2022**, 100387.

9. SnO2 Nanofibers Network for Cold Cathode Applications in Vacuum Nanoelectronics.
Giubileo, F.; Faella, E.; Pelella, A.; Kumar, A.; Capista, D.; Passacantando, M.; Kim, S.S.; Di Bartolomeo, A.
Adv. Electron. Mater. **2022**, 2200237.

10. A Self-Powered CNT–Si Photodetector with Tuneable Photocurrent.
Pelella, A.; Capista, D.; Passacantando, M.; Faella, E.; Grillo, A.; Giubileo, F.; Martucciello, N.; Di Bartolomeo, A.
Adv. Electron. Mater. **2022** 2200919.

Activities

Attended courses:

A.Y. 2020/2021	Fabrication and characterization of nanostructures, Prof. C. Mariani (Università La Sapienza)
A.Y. 2020/2021	Radiation-Matter Interaction, Photoemission and Photoabsorption Spectroscopy, Prof. C. Mariani, Prof. S. Mobilio, Prof. F. Offi, Prof. A. Ruocco. (Università La Sapienza)
A.Y. 2020/2021	Introduction to quantum computing, Prof. L. Guidoni (Univeristà degli studi dell'Aquila)
A.Y. 2020/2022	English for Academic Purposes Prof. M. Fiorenza (Univeristà degli studi dell'Aquila)

Attended school:

19 Sep. 2022 - 30 Sep. 2022	XVI School on Synchrotron Radiation: Fundamentals, Methods and Applications, Muggia (Italy)

Assignments:

Sep 21 – Feb 22	Università degli Studi dell'Aquila, L'Aquila. "Svolgimento dell'attività di esercitazioni didattiche e attività di supporto agli studenti, iscritti ai Corsi di Laurea del Dipartimento di Ingegneria Civile, Edile-Architettura, Ambientale per l'a.a. 2021/2022 - Conduct of practice exercises and support activities for the students enrolled in the Bachelor Degree of the department of Department of Civil, Construction-Architectural and Environmental Engineering for the a.y. 2021/2022".
Sep 22 – ongoing	Università degli Studi dell'Aquila, L'Aquila. "Svolgimento dell'attività di esercitazioni didattiche e attività di supporto agli studenti, iscritti ai Corsi di Laurea del Dipartimento di Ingegneria Civile, Edile-Architettura, Ambientale per l'a.a. 2022/2023 - Conduct of

practice exercises and support activities for the students enrolled in the Bachelor Degree of the department of Department of Civil, Construction-Architectural and Environmental Engineering for the a.y. 2022/2023".

Sep 22 – ongoing — Università degli Studi dell'Aquila, L'Aquila.
"Svolgimento dell'attività di ESERCITAZIONI DI FISICA (F3D), per n. 40 ore con svolgimento nel I/II semestre dell'a.a. 2022/2023 - Conduct of practice exercises on Physic enrolled in the Bachelor Degree in Chemistry and Material Science of the Department of Physical and Chemical Sciences a.y. 2022/2023".

Conferences and seminars:

9 Dec 2021 – 10 Dec 2021 — Italy-Taiwan bilateral workshop on emergent crystalline materials
Online workshop – Member of the organization committee. https://ittwsymposium.wordpress.com/

15 Nov 2020 – 15 Nov 2020 — The 2nd international Online-Conference on nanomaterials: Photoresponse Study of MWCNTS/Insulator/n-Type Si/Insulator/Metal Heterostructure as a Function of the Density of MWCNTs Layer
Online

Visiting period:

1 Apr 2022 – 30 Jun 2022 — Leibniz Institute for high performance microelectronics
IHP GmbH Frankfurt (Oder).
In the Materials research Department of IHP, on the topic: "Electrical Characterization of Graphene and 2D-based Devices"

References

1. Agostinelli, T.; Campoy-Quiles, M.; Blakesley, J.C.; Speller, R.; Bradley, D.D.C.; Nelson, J. A polymer/fullerene based photodetector with extremely low dark current for x-ray medical imaging applications. *Appl. Phys. Lett.* **2008**, *93*, 203305, doi:10.1063/1.3028640.
2. Mueller, T.; Xia, F.; Avouris, P. Graphene photodetectors for high-speed optical communications. *Nat. Photonics* **2010**, *4*, 297–301.
3. Lahiri, B.B.; Bagavathiappan, S.; Jayakumar, T.; Philip, J. Medical applications of infrared thermography: a review. *Infrared Phys. Technol.* **2012**, *55*, 221–235.
4. Ryzhii, V.; Otsuji, T.; Karasik, V.E.; Ryzhii, M.; Leiman, V.G.; Mitin, V.; Shur, M.S. Comparison of intersubband quantum-well and interband graphene-layer infrared photodetectors. *IEEE J. Quantum Electron.* **2018**, *54*, 1–8.
5. Jalali, B.; Fathpour, S. Silicon Photonics. *J. Light. Technol.* **2006**, *24*, 4600–4615, doi:10.1109/JLT.2006.885782.
6. Temkin, H.; Bean, J.C.; Pearsall, T.P.; Olsson, N.A.; Lang, D. V High photoconductive gain in Ge x Si1− x/Si strained-layer superlattice detectors operating at λ= 1.3 μm. *Appl. Phys. Lett.* **1986**, *49*, 155–157.
7. Hawkins, A.R.; Reynolds, T.E.; England, D.R.; Babic, D.I.; Mondry, M.J.; Streubel, K.; Bowers, J.E. Silicon heterointerface photodetector. *Appl. Phys. Lett.* **1996**, *68*, 3692–3694, doi:10.1063/1.115975.
8. Li, X.; Mariano, M.; McMillon-Brown, L.; Huang, J.; Sfeir, M.Y.; Reed, M.A.; Jung, Y.; Taylor, A.D. Charge transfer from carbon nanotubes to silicon in flexible carbon nanotube/silicon solar cells. *Small* **2017**, *13*, 1702387.
9. Diao, J.; Srivastava, D.; Menon, M. Molecular dynamics simulations of carbon nanotube/silicon interfacial thermal conductance. *J. Chem. Phys.* **2008**, *128*, 164708.
10. Aramo, C.; Ambrosio, A.; Ambrosio, M.; Battiston, R.; Castrucci, P.; Cilmo, M.; De Crescenzi, M.; Fiandrini, E.; Guarino, F.; Grossi, V. Development of new photon detection device for Cherenkov and fluorescence radiation. In Proceedings of the EPJ Web of Conferences; EDP Sciences, 2013; Vol. 53, p. 8014.

11. Li, X.; Lv, Z.; Zhu, H. Carbon/silicon heterojunction solar cells: state of the art and prospects. *Adv. Mater.* **2015**, *27*, 6549–6574.
12. Jia, Y.; Cao, A.; Bai, X.; Li, Z.; Zhang, L.; Guo, N.; Wei, J.; Wang, K.; Zhu, H.; Wu, D.; et al. Achieving High Efficiency Silicon-Carbon Nanotube Heterojunction Solar Cells by Acid Doping. *Nano Lett.* **2011**, *11*, 1901–1905, doi:10.1021/nl2002632.
13. Fujiwara, A.; Matsuoka, Y.; Suematsu, H.; Ogawa, N.; Miyano, K.; Kataura, H.; Maniwa, Y.; Suzuki, S.; Achiba, Y. Photoconductivity in Semiconducting Single-Walled Carbon Nanotubes. *Jpn. J. Appl. Phys.* **2001**, *40*, L1229, doi:10.1143/JJAP.40.L1229.
14. Wei, J.; Sun, J.-L.; Zhu, J.-L.; Wang, K.; Wang, Z.; Luo, J.; Wu, D.; Cao, A. Carbon Nanotube Macrobundles for Light Sensing. *Small* **2006**, *2*, 988–993, doi:https://doi.org/10.1002/smll.200600191.
15. Misewich, J.A.; Martel, R.; Avouris, P.; Tsang, J.C.; Heinze, S.; Tersoff, J. Electrically induced optical emission from a carbon nanotube FET. *Science (80-.).* **2003**, *300*, 783–786.
16. Lee, J.U. Photovoltaic effect in ideal carbon nanotube diodes. *Appl. Phys. Lett.* **2005**, *87*, 73101, doi:10.1063/1.2010598.
17. Kamat, P. V Harvesting photons with carbon nanotubes. *Nano Today* **2006**, *1*, 20–27.
18. Scagliotti, M.; Salvato, M.; Frezza, F.; Catone, D.; Di Mario, L.; Boscardin, M.; De Crescenzi, M.; Castrucci, P. Carbon nanotube film/silicon heterojunction photodetector for new cutting-edge technological devices. *Appl. Sci.* **2021**, *11*, 606.
19. Di Bartolomeo, A. Graphene Schottky diodes: An experimental review of the rectifying graphene/semiconductor heterojunction. *Phys. Rep.* **2016**, *606*, 1–58, doi:https://doi.org/10.1016/j.physrep.2015.10.003.
20. Tinti, A.; Righetti, F.; Ligonzo, T.; Valentini, A.; Nappi, E.; Ambrosio, A.; Ambrosio, M.; Aramo, C.; Maddalena, P.; Castrucci, P.; et al. Electrical analysis of carbon nanostructures/silicon heterojunctions designed for radiation detection. *Nucl. Instruments Methods Phys. Res. Sect. A Accel. Spectrometers, Detect. Assoc. Equip.* **2011**, *629*, 377–381, doi:https://doi.org/10.1016/j.nima.2010.11.097.
21. Passacantando, M.; Bussolotti, F.; Grossi, V.; Santucci, S.; Ambrosio, A.; Ambrosio, M.; Ambrosone, G.; Carillo, V.; Coscia, U.; Maddalena, P.; et al. Photoconductivity

in defective carbon nanotube sheets under ultraviolet–visible–near infrared radiation. *Appl. Phys. Lett.* **2008**, *93*, 51911, doi:10.1063/1.2968203.

22. Passacantando, M.; Grossi, V.; Santucci, S. High photocurrent from planar strips of vertical and horizontal aligned multi wall carbon nanotubes. *Appl. Phys. Lett.* **2012**, *100*, 163119, doi:10.1063/1.4704569.
23. Melisi, D.; Nitti, M.A.; Valentini, M.; Valentini, A.; Ligonzo, T.; De Pascali, G.; Ambrico, M. Photodetectors based on carbon nanotubes deposited by using a spray technique on semi-insulating gallium arsenide. *Beilstein J. Nanotechnol.* **2014**, *5*, 1999–2006, doi:10.3762/bjnano.5.208.
24. Valentini, L.; Cantalini, C.; Armentano, I.; Kenny, J.M.; Lozzi, L.; Santucci, S. Highly sensitive and selective sensors based on carbon nanotubes thin films for molecular detection. *Diam. Relat. Mater.* **2004**, *13*, 1301–1305.
25. Kong, J.; Franklin, N.R.; Zhou, C.; Chapline, M.G.; Peng, S.; Cho, K.; Dai, H. Nanotube molecular wires as chemical sensors. *Science (80-.).* **2000**, *287*, 622–625.
26. Kroto, H.W.; Heath, J.R.; O'Brien, S.C.; Curl, R.F.; Smalley, R.E. C60: Buckminsterfullerene. *Nature* **1985**, *318*, 162–163, doi:10.1038/318162a0.
27. Iijima, S. Helical microtubules of graphitic carbon. *Nature* **1991**, *354*, 56–58, doi:10.1038/354056a0.
28. Iijima, S.; Ichihashi, T. Single-shell carbon nanotubes of 1-nm diameter. *Nature* **1993**, *363*, 603–605, doi:10.1038/363603a0.
29. Bethune, D.S.; Kiang, C.H.; de Vries, M.S.; Gorman, G.; Savoy, R.; Vazquez, J.; Beyers, R. Cobalt-catalysed growth of carbon nanotubes with single-atomic-layer walls. *Nature* **1993**, *363*, 605–607, doi:10.1038/363605a0.
30. Bugatti, V.; Viscusi, G.; Di Bartolomeo, A.; Iemmo, L.; Zampino, D.C.; Vittoria, V.; Gorrasi, G. Ionic Liquid as Dispersing Agent of LDH-Carbon Nanotubes into a Biodegradable Vinyl Alcohol Polymer. *Polymers (Basel).* **2020**, *12*, doi:10.3390/polym12020495.
31. Guadagno, L.; De Vivo, B.; Di Bartolomeo, A.; Lamberti, P.; Sorrentino, A.; Tucci, V.; Vertuccio, L.; Vittoria, V. Effect of functionalization on the thermo-mechanical and electrical behavior of multi-wall carbon nanotube/epoxy composites. *Carbon N. Y.* **2011**, *49*, 1919–1930, doi:10.1016/J.CARBON.2011.01.017.

32. Gorrasi, G.; Bugatti, V.; Milone, C.; Mastronardo, E.; Piperopoulos, E.; Iemmo, L.; Di Bartolomeo, A. Effect of temperature and morphology on the electrical properties of PET/conductive nanofillers composites. *Compos. Part B Eng.* **2018**, *135*, 149–154, doi:10.1016/J.COMPOSITESB.2017.10.020.
33. Gorrasi, G.; Sarno, M.; Di Bartolomeo, A.; Sannino, D.; Ciambelli, P.; Vittoria, V. Incorporation of carbon nanotubes into polyethylene by high energy ball milling: Morphology and physical properties. *J. Polym. Sci. Part B Polym. Phys.* **2007**, *45*, 597–606, doi:https://doi.org/10.1002/polb.21070.
34. Camilli, L.; Passacantando, M. Advances on Sensors Based on Carbon Nanotubes. *Chemosensors* **2018**, *6*, 62, doi:10.3390/chemosensors6040062.
35. Kruss, S.; Hilmer, A.J.; Zhang, J.; Reuel, N.F.; Mu, B.; Strano, M.S. Carbon nanotubes as optical biomedical sensors. *Adv. Drug Deliv. Rev.* **2013**, *65*, 1933–1950, doi:10.1016/j.addr.2013.07.015.
36. Zaporotskova, I. V; Boroznina, N.; Parkhomenko, Y.N.; Kozhitov, L. V Carbon nanotubes: Sensor properties. A review. *Mod. Electron. Mater.* **2016**, *2*, 95–105.
37. Baughman, R.H.; Zakhidov, A.A.; de Heer, W.A. Carbon Nanotubes--the Route Toward Applications. *Science (80-.).* **2002**, *297*, 787–792, doi:10.1126/science.1060928.
38. Hata, K.; Futaba, D.N.; Mizuno, K.; Namai, T.; Yumura, M.; Iijima, S. Water-Assisted Highly Efficient Synthesis of Impurity-Free Single-Walled Carbon Nanotubes. *Science (80-.).* **2004**, *306*, 1362–1364, doi:10.1126/science.1104962.
39. Gui, X.; Wei, J.; Wang, K.; Cao, A.; Zhu, H.; Jia, Y.; Shu, Q.; Wu, D. Carbon Nanotube Sponges. *Adv. Mater.* **2010**, *22*, 617–621, doi:10.1002/adma.200902986.
40. Chung, D.D.L. Review Graphite. *J. Mater. Sci.* **2002**, *37*, 1475–1489, doi:10.1023/A:1014915307738.
41. Dresselhaus, G.; Dresselhaus, M.S.; Saito, R. *Physical properties of carbon nanotubes*; World scientific, 1998; ISBN 1783262419.
42. Eatemadi, A.; Daraee, H.; Karimkhanloo, H.; Kouhi, M.; Zarghami, N.; Akbarzadeh, A.; Abasi, M.; Hanifehpour, Y.; Joo, S.W. Carbon nanotubes: properties, synthesis, purification, and medical applications. *Nanoscale Res. Lett.* **2014**, *9*, 393, doi:10.1186/1556-276X-9-393.

43. Saito, R.; Dresselhaus, G.; Dresselhaus, M.S. Electronic structure of double-layer graphene tubules. *J. Appl. Phys.* **1993**, *73*, 494–500, doi:10.1063/1.353358.
44. Charlier, J.-C.; Michenaud, J.-P. Energetics of multilayered carbon tubules. *Phys. Rev. Lett.* **1993**, *70*, 1858–1861, doi:10.1103/PhysRevLett.70.1858.
45. Scott, C.D.; Arepalli, S.; Nikolaev, P.; Smalley, R.E. Growth mechanisms for single-wall carbon nanotubes in a laser-ablation process. *Appl. Phys. A* **2001**, *72*, 573–580.
46. Maser, W.K.; Muñoz, E.; Benito, A.M.; Martınez, M.T.; De La Fuente, G.F.; Maniette, Y.; Anglaret, E.; Sauvajol, J.-L. Production of high-density single-walled nanotube material by a simple laser-ablation method. *Chem. Phys. Lett.* **1998**, *292*, 587–593.
47. Guo, T.; Nikolaev, P.; Thess, A.; Colbert, D.T.; Smalley, R.E. Catalytic growth of single-walled manotubes by laser vaporization. *Chem. Phys. Lett.* **1995**, *243*, 49–54.
48. Yudasaka, M.; Yamada, R.; Sensui, N.; Wilkins, T.; Ichihashi, T.; Iijima, S. Mechanism of the effect of NiCo, Ni and Co catalysts on the yield of single-wall carbon nanotubes formed by pulsed Nd: YAG laser ablation. *J. Phys. Chem. B* **1999**, *103*, 6224–6229.
49. Journet, C.; Bernier, P. Production of carbon nanotubes. *Appl. Phys. A Mater. Sci. Process.* **1998**, *67*.
50. Ebbesen, T.W.; Ajayan, P.M. Large-scale synthesis of carbon nanotubes. *Nature* **1992**, *358*, 220–222.
51. Ren, Z.F.; Huang, Z.P.; Xu, J.W.; Wang, J.H.; Bush, P.; Siegal, M.P.; Provencio, P.N. Synthesis of large arrays of well-aligned carbon nanotubes on glass. *Science (80-.).* **1998**, *282*, 1105–1107.
52. Sinnott, S.B.; Andrews, R.; Qian, D.; Rao, A.M.; Mao, Z.; Dickey, E.C.; Derbyshire, F. Model of carbon nanotube growth through chemical vapor deposition. *Chem. Phys. Lett.* **1999**, *315*, 25–30.
53. Ren, Z.F.; Huang, Z.P.; Wang, D.Z.; Wen, J.G.; Xu, J.W.; Wang, J.H.; Calvet, L.E.; Chen, J.; Klemic, J.F.; Reed, M.A. Growth of a single freestanding multiwall carbon nanotube on each nanonickel dot. *Appl. Phys. Lett.* **1999**, *75*, 1086–1088.
54. Camilli, L.; Capista, D.; Eramo, P.; D'Archivio, A.A.; Maggi, M.A.; Lazzarini, A.; Crucianelli, M.; Passacantando, M. Synthesis of hydrophilic carbon nanotube sponge

via post-growth thermal treatment. *Nanotechnology* **2022**, *33*, 245707, doi:10.1088/1361-6528/ac5bb7.
55. Dai, H.; Rinzler, A.G.; Nikolaev, P.; Thess, A.; Colbert, D.T.; Smalley, R.E. Single-wall nanotubes produced by metal-catalyzed disproportionation of carbon monoxide. *Chem. Phys. Lett.* **1996**, *260*, 471–475, doi:https://doi.org/10.1016/0009-2614(96)00862-7.
56. Grosso, G.; Parravicini, G.P. *Solid state physics*; Academic press, 2013; ISBN 0123850312.
57. Sze, S.M.; Li, Y.; Ng, K.K. *Physics of semiconductor devices*; John wiley & sons, 2021; ISBN 1119618002.
58. Bethe, H.A. Theory of the boundary layer of crystal rectifiers. In *Semiconductor Devices: Pioneering Papers*; World Scientific, 1991; pp. 387–399.
59. Cheung, C.L.; Kurtz, A.; Park, H.; Lieber, C.M. Diameter-Controlled Synthesis of Carbon Nanotubes. *J. Phys. Chem. B* **2002**, *106*, 2429–2433, doi:10.1021/jp0142278.
60. Filho, A.G.S.; Jorio, A.; Samsonidze, G.G.; Dresselhaus, G.; Saito, R.; Dresselhaus, M.S. Raman spectroscopy for probing chemically/physically induced phenomena in carbon nanotubes. *Nanotechnology* **2003**, *14*, 1130–1139, doi:10.1088/0957-4484/14/10/311.
61. Di Bartolomeo, A.; Rücker, H.; Schley, P.; Fox, A.; Lischke, S.; Na, K.-Y. A single-poly EEPROM cell for embedded memory applications. *Solid. State. Electron.* **2009**, *53*, 644–648, doi:https://doi.org/10.1016/j.sse.2009.04.007.
62. Giubileo, F.; Bartolomeo, A. Di; Scarfato, A.; Iemmo, L.; Bobba, F.; Passacantando, M.; Santucci, S.; Cucolo, A.M. Local probing of the field emission stability of vertically aligned multi-walled carbon nanotubes. *Carbon N. Y.* **2009**, *47*, 1074–1080, doi:https://doi.org/10.1016/j.carbon.2008.12.035.
63. Di Bartolomeo, A.; Giubileo, F.; Grillo, A.; Luongo, G.; Iemmo, L.; Urban, F.; Lozzi, L.; Capista, D.; Nardone, M.; Passacantando, M. Bias tunable photocurrent in metal-insulator-semiconductor heterostructures with photoresponse enhanced by carbon nanotubes. *Nanomaterials* **2019**, *9*, doi:10.3390/nano9111598.
64. Di Bartolomeo, A.; Scarfato, A.; Giubileo, F.; Bobba, F.; Biasiucci, M.; Cucolo, A.M.; Santucci, S.; Passacantando, M. A local field emission study of partially aligned

carbon-nanotubes by atomic force microscope probe. *Carbon N. Y.* **2007**, *45*, 2957–2971, doi:https://doi.org/10.1016/j.carbon.2007.09.049.

65. Ahn, Y.H.; Tsen, A.W.; Kim, B.; Park, Y.W.; Park, J. Photocurrent Imaging of p−n Junctions in Ambipolar Carbon Nanotube Transistors. *Nano Lett.* **2007**, *7*, 3320–3323, doi:10.1021/nl071536m.
66. Mueller, T.; Xia, F.; Freitag, M.; Tsang, J.; Avouris, P. Role of contacts in graphene transistors: A scanning photocurrent study. *Phys. Rev. B* **2009**, *79*, 245430, doi:10.1103/PhysRevB.79.245430.
67. De Nicola, F.; Castrucci, P.; Scarselli, M.; Nanni, F.; Cacciotti, I.; De Crescenzi, M. Multi-Fractal Hierarchy of Single-Walled Carbon Nanotube Hydrophobic Coatings. **2015**, doi:10.1038/srep08583.
68. Capista, D.; Passacantando, M.; Lozzi, L.; Faella, E.; Giubileo, F.; Di Bartolomeo, A. Easy Fabrication of Performant SWCNT-Si Photodetector. *Electronics* **2022**, *11*, doi:10.3390/electronics11020271.
69. Kim, K.K.; Yoon, S.-M.; Choi, J.-Y.; Lee, J.; Kim, B.-K.; Kim, J.M.; Lee, J.-H.; Paik, U.; Park, M.H.; Yang, C.W.; et al. Design of Dispersants for the Dispersion of Carbon Nanotubes in an Organic Solvent. *Adv. Funct. Mater.* **2007**, *17*, 1775–1783, doi:https://doi.org/10.1002/adfm.200600915.
70. Hilding, J.; Grulke, E.A.; George Zhang, Z.; Lockwood, F. Dispersion of carbon nanotubes in liquids. *J. Dispers. Sci. Technol.* **2003**, *24*, 1–41.
71. Kato, H.; Nakamura, A.; Horie, M. Behavior of surfactants in aqueous dispersions of single-walled carbon nanotubes. *RSC Adv.* **2014**, *4*, 2129–2136, doi:10.1039/C3RA45181J.
72. Fischer, S.; Thümmler, K.; Volkert, B.; Hettrich, K.; Schmidt, I.; Fischer, K. Properties and Applications of Cellulose Acetate. *Macromol. Symp.* **2008**, *262*, 89–96, doi:https://doi.org/10.1002/masy.200850210.
73. Majumder, S.; Matin, M.A.; Sharif, A.; Arafat, M.T. Understanding solubility, spinnability and electrospinning behaviour of cellulose acetate using different solvent systems. *Bull. Mater. Sci.* **2019**, *42*, 1–9.
74. Camilli, L.; Pisani, C.; Gautron, E.; Scarselli, M.; Castrucci, P.; D'Orazio, F.; Passacantando, M.; Moscone, D.; De Crescenzi, M. A three-dimensional carbon

nanotube network for water treatment. *Nanotechnology* **2014**, *25*, 065701, doi:10.1088/0957-4484/25/6/065701.

75. Dresselhaus, M.S.; Dresselhaus, G.; Saito, R.; Jorio, A. Raman spectroscopy of carbon nanotubes. *Phys. Rep.* 2005, *409*, 47–99.
76. Di Bartolomeo, A.; Giubileo, F.; Grillo, A.; Luongo, G.; Iemmo, L.; Urban, F.; Lozzi, L.; Capista, D.; Nardone, M.; Passacantando, M. Bias Tunable Photocurrent in Metal-Insulator-Semiconductor Heterostructures with Photoresponse Enhanced by Carbon Nanotubes. *Nanomaterials* **2019**, *9*, 1598, doi:10.3390/nano9111598.
77. Liu, P.; Sun, Q.; Zhu, F.; Liu, K.; Jiang, K.; Liu, L.; Li, Q.; Fan, S. Measuring the Work Function of Carbon Nanotubes with Thermionic Method. *Nano Lett.* **2008**, *8*, 647–651, doi:10.1021/nl0730817.
78. Tao, S.X.; Theulings, A.; Smedley, J.; van der Graaf, H. DFT study of electron affinity of hydrogen terminated β-Si3N4. *Diam. Relat. Mater.* **2015**, *53*, 52–57, doi:https://doi.org/10.1016/j.diamond.2015.02.001.
79. Ismail, R.A.; Mohammed, M.I.; Mahmood, L.H. Preparation of multi-walled carbon nanotubes/n-Si heterojunction photodetector by arc discharge technique. *Optik (Stuttg).* **2018**, *164*, 395–401, doi:10.1016/J.IJLEO.2018.03.043.
80. Salvato, M.; Scagliotti, M.; De Crescenzi, M.; Boscardin, M.; Attanasio, C.; Avallone, G.; Cirillo, C.; Prosposito, P.; De Matteis, F.; Messi, R.; et al. Time response in carbon nanotube/Si based photodetectors. *Sensors Actuators A Phys.* **2019**, *292*, 71–76, doi:https://doi.org/10.1016/j.sna.2019.04.004.
81. Fidan, M.; Ünverdi, Ö.; Çelebi, C. Junction area dependent performance of graphene/silicon based self-powered Schottky photodiodes. *Sensors Actuators A Phys.* **2021**, *331*, 112829.
82. Lv, P.; Zhang, X.; Zhang, X.; Deng, W.; Jie, J. High-Sensitivity and Fast-Response Graphene/Crystalline Silicon Schottky Junction-Based Near-IR Photodetectors. *IEEE Electron Device Lett.* **2013**, *34*, 1337–1339, doi:10.1109/LED.2013.2275169.
83. Periyanagounder, D.; Gnanasekar, P.; Varadhan, P.; He, J.-H.; Kulandaivel, J. High performance, self-powered photodetectors based on a graphene/silicon Schottky junction diode. *J. Mater. Chem. C* **2018**, *6*, 9545–9551.
84. Bel'skii, M.D.; Bocharov, G.S.; Eletskii, A. V; Sommerer, T.J. Electric field

enhancement in field-emission cathodes based on carbon nanotubes. *Tech. Phys.* **2010**, *55*, 289–295, doi:10.1134/S1063784210020210.

85. Cheung, S.K.; Cheung, N.W. Extraction of Schottky diode parameters from forward current-voltage characteristics. *Appl. Phys. Lett.* **1986**, *49*, 85–87, doi:10.1063/1.97359.

86. Tataroğlu, A.; Pür, F.Z. The Richardson constant and barrier inhomogeneity at Au/Si3N4/n-Si (MIS) Schottky diodes. *Phys. Scr.* **2013**, *88*, 15801, doi:10.1088/0031-8949/88/01/015801.

87. Ertürk, K.; Bektöre, Y.; Cüneyt Haciismailoglu, M. Electrical and Schottky contact properties of Pt/n-Si1–xGex/n-Si(100) heterostructure. *Phys. status solidi* **2005**, *2*, 1428–1432, doi:https://doi.org/10.1002/pssc.200460480.

88. Knotter, D.M.; Denteneer, T.J.J.D. Etching mechanism of silicon nitride in HF-based solutions. *J. Electrochem. Soc.* **2001**, *148*, F43.

89. Sénémaud, C.; Driss-Khodja, M.; Gheorghiu, A.; Harel, S.; Dufour, G.; Roulet, H. Electronic structure of silicon nitride studied by both soft x-ray spectroscopy and photoelectron spectroscopy. *J. Appl. Phys.* **1993**, *74*, 5042–5046, doi:10.1063/1.354286.

90. Sokolov, A.A.; Filatova, E.O.; Afanas'ev, V. V; Taracheva, E.Y.; Brzhezinskaya, M.M.; Ovchinnikov, A.A. Interface analysis of HfO2 films on (1 0 0)Si using x-ray photoelectron spectroscopy. *J. Phys. D. Appl. Phys.* **2008**, *42*, 35308, doi:10.1088/0022-3727/42/3/035308.

91. Al-Ahmadi, N.A. Metal oxide semiconductor-based Schottky diodes: a review of recent advances. *Mater. Res. Express* **2020**, *7*, 32001, doi:10.1088/2053-1591/ab7a60.

92. Shetty, A.; Roul, B.; Mukundan, S.; Mohan, L.; Chandan, G.; Vinoy, K.J.; Krupanidhi, S.B. Temperature dependent electrical characterisation of Pt/HfO2/n-GaN metal-insulator-semiconductor (MIS) Schottky diodes. *AIP Adv.* **2015**, *5*, 97103, doi:10.1063/1.4930199.

93. Ouyang, W.; Teng, F.; He, J.; Fang, X. Enhancing the photoelectric performance of photodetectors based on metal oxide semiconductors by charge-carrier engineering. *Adv. Funct. Mater.* **2019**, *29*, 1807672.

94. Luongo, G.; Di Bartolomeo, A.; Giubileo, F.; Chavarin, C.A.; Wenger, C. Electronic

properties of graphene/p-silicon Schottky junction. *J. Phys. D. Appl. Phys.* **2018**, *51*, 255305.
95. Riazimehr, S.; Kataria, S.; Gonzalez-Medina, J.M.; Wagner, S.; Shaygan, M.; Suckow, S.; Ruiz, F.G.; Engström, O.; Godoy, A.; Lemme, M.C. High responsivity and quantum efficiency of graphene/silicon photodiodes achieved by interdigitating Schottky and gated regions. *Acs Photonics* **2018**, *6*, 107–115.
96. Riazimehr, S.; Belete, M.; Kataria, S.; Engström, O.; Lemme, M.C. Capacitance–Voltage (C–V) Characterization of Graphene–Silicon Heterojunction Photodiodes. *Adv. Opt. Mater.* **2020**, *8*, 2000169.
97. Riazimehr, S.; Kataria, S.; Bornemann, R.; Haring Bolívar, P.; Ruiz, F.J.G.; Engström, O.; Godoy, A.; Lemme, M.C. High photocurrent in gated graphene–silicon hybrid photodiodes. *ACS photonics* **2017**, *4*, 1506–1514.
98. Di Bartolomeo, A.; Luongo, G.; Giubileo, F.; Funicello, N.; Niu, G.; Schroeder, T.; Lisker, M.; Lupina, G. Hybrid graphene/silicon Schottky photodiode with intrinsic gating effect. *2D Mater.* **2017**, *4*, 25075.
99. Jia, Y.; Cao, A.; Kang, F.; Li, P.; Gui, X.; Zhang, L.; Shi, E.; Wei, J.; Wang, K.; Zhu, H. Strong and reversible modulation of carbon nanotube–silicon heterojunction solar cells by an interfacial oxide layer. *Phys. Chem. Chem. Phys.* **2012**, *14*, 8391–8396.